
Evaluation of ADC Physicochemical Characteristics and Their Impact on Pharmacokinetics in Transgenic huFcRn Mice



TECHNISCHE
UNIVERSITÄT
DARMSTADT

**vom Fachbereich Chemie
der Technischen Universität Darmstadt**

zur Erlangung des Grades
Doctor rerum naturalium
(Dr. rer. nat.)

**genehmigte Dissertation
von Anna Kaempffe, M.Sc.**

Erstgutachter: Prof. Dr. Harald Kolmar
Zweitgutachter: Prof. Dr. Dr. Siegfried Neumann

Darmstadt 2022

Kaempffe, Anna

***Evaluation of ADC Physicochemical Characteristics and
Their Impact on Pharmacokinetics in Transgenic huFcRn Mice***

Darmstadt, Technische Universität Darmstadt

Tag der Einreichung: 02. Juni. 2022

Tag der mündlichen Prüfung: 21. Juli. 2022

Jahr der Veröffentlichung der Dissertation auf TUpriints: 2022

Lizenz: Veröffentlicht unter CC BY 4.0 International

URN: urn:nbn:de:tuda-tuprints-218487

URI: <https://tuprints.ulb.tu-darmstadt.de/id/eprint/21848>



Die vorliegende Arbeit wurde unter der Leitung von Herrn Prof. Dr. Harald Kolmar am Clemens-Schöpf-Institut für Organische Chemie und Biochemie der Technischen Universität Darmstadt sowie bei der Merck KGaA in Darmstadt von Februar 2017 bis Juni 2022 angefertigt.



Publications or patents derived from the presented work

Parts of this work have been published:

Kaempffe A., Dickgiesser S., Rasche N., Paoletti A., Bertotti E., De Slave I., Sirtori F.R., Kellner R., Könning D., Hecht S., Anderl J., Kolmar H., Schröter C. (2021) Effect of Conjugation Site and Technique on the Stability and Pharmacokinetics of Antibody-Drug Conjugates. *J Pharm Sci.* 110 (12), 3776-3785

Publications to other projects

Kaempffe A.*, Jäger S.*, Könning D., Kolmar H., Schröter C. (2020) Isolation of Tailor-Made Antibody Fragments from Yeast-Displayed B-Cell Receptor Repertoires by Multiparameter Fluorescence-Activated Cell Sorting. *Methods in Molecular Biology. Vol 2070: Genotype Phenotype Coupling: Methods and Protocols* (Zielonka S., Krah S., Eds.) pp 249-266, Chapter 14, Springer US, New York.

Könning D., Zielonka S., **Kaempffe A.**, Jäger S., Kolmar H., Schröter C. (2020) Selection and Characterization of Anti-idiotypic Shark Antibody Domains. *Methods in Molecular Biology. Vol 2070: Genotype Phenotype Coupling: Methods and Protocols* (Zielonka S., Krah S., Eds.) pp 191-209, Chapter 11, Springer US, New York.

* contributed equally to this work.

1. Table of Contents

1.....	TABLE OF CONTENTS	1
2.....	ABSTRACT	1
3.....	ZUSAMMENFASSUNG.....	3
4.....	INTRODUCTION.....	5
4.1.	Antibody-Drug Conjugates	5
4.1.1.	Mechanism of Action of ADCs.....	6
4.1.2.	Structure and Function of Antibodies	7
4.1.3.	Clinically Approved ADCs.....	9
4.2.	ADC Design Features to Improve the Therapeutic Window	9
4.2.1.	Antibody	9
4.2.2.	Cytotoxic Drug	11
4.2.3.	Linker	12
4.2.4.	Conjugation Strategy	13
4.3.	Elimination of ADCs from the Blood Stream	17
4.3.1.	Elimination Mechanisms of ADCs.....	18
4.3.2.	Screening Assays to Identify mAbs and ADCs with Risk for Poor Pharmacokinetics	20
4.3.3.	Human FcRn Transgenic Mouse Models	23
4.3.4.	Pharmacokinetic Analyses of ADCs	25
5.....	OBJECTIVE OF THIS WORK.....	27
6.....	MATERIAL AND METHODS.....	28
6.1.	Mammalian Cell Lines and Culture Media	28
6.2.	Bacterial Strain	28
6.3.	Mouse Strain	28
6.4.	Antibody Sequences.....	28
6.5.	Commercial Antibodies	34
6.6.	Enzymes and Proteins	34
6.7.	Chemicals.....	35
6.8.	Prepared Solutions, Buffer, and Media.....	37

6.9. Kits and Consumables.....	38
6.10. Equipment	39
6.11. Software.....	41
6.12. Transformation of <i>E. coli</i>	42
6.13. Plasmid Amplification and Preparation	42
6.14. Quantification of DNA in Aqueous Solutions.....	43
6.15. Expression of Antibodies	43
6.16. Quantification of Protein in Aqueous Solutions	43
6.17. Generation of ADCs with Different Conjugation Methods.....	44
6.17.1. Conjugation to Interchain Cysteines.....	44
6.17.2. Conjugation to Engineered Cysteines.....	44
6.17.3. Conjugation via Microbial Transglutaminase	45
6.17.4. Site-Specific Conjugation to Native mAbs	45
6.17.5. Conjugation via Sortase A.....	45
6.18. Protein A Chromatography.....	45
6.19. Preparative Size Exclusion Chromatography (SEC).....	46
6.20. Analytical Size Exclusion Chromatography (SE-HPLC)	46
6.21. Analytical Hydrophobic Interaction Chromatography.....	46
6.22. DAR Determination by Liquid Chromatography-Mass Spectroscopy.....	48
6.23. <i>In vitro</i> Serum Stability Analyzed by Liquid Chromatography-Mass Spectroscopy and Enzyme-Linked Immunosorbent Assay	49
6.24. Pharmacokinetic Studies in huFcRn Mice.....	50
6.25. Total Antibody Ligand Binding Assay for the Analyses of Pharmacokinetic Samples	50
6.26. Antibody-Conjugated Payload Assay for the Analyses of Pharmacokinetic Samples	51
6.27. Analysis of Pharmacokinetic Parameters	51
6.28. Nano Differential Scanning Fluorimetry.....	52
6.29. huFcRn Affinity Chromatography	52
6.30. Bio-Layer Interferometry.....	53
6.30.1. huFcRn Binding Kinetics.....	54

6.30.2. Clone Self-Interaction Bio-Layer Interferometry.....	54
6.30.3. Polyspecificity Reagent Bio-Layer Interferometry.....	55
6.31. Bis-ANS Assay	56
6.32. Affinity-Capture Self-Interaction Nanoparticle Spectroscopy.....	56
6.33. Baculovirus Particle Enzyme-Linked Immunosorbent Assay.....	57
6.34. Heparin Enzyme-Linked Immunosorbent Assay.....	58
7..... RESULTS AND DISCUSSION	59
7.1. Relationship Between HIC, huFcRn Affinity, and Thermal Stability Analysis of ADCs Conjugated at Different Conjugation Sites and Their Pharmacokinetics	59
7.1.1. ADC Design and Generation	59
7.1.2. Hydrophobicity of the ADCs	62
7.1.3. Thermal Stability of the ADCs.....	63
7.1.4. Binding Kinetics to Soluble huFcRn	65
7.1.5. <i>In Vitro</i> Mouse Serum Stability of the ADCs.....	67
7.1.6. Pharmacokinetics and Stability of the ADCs in huFcRn Mice.....	70
7.1.7. Correlation of the <i>In Vitro</i> and <i>In Vivo</i> Results	75
7.2. Establishment of Additional <i>In Vitro</i> Assays to Analyze ADC Physicochemical Properties for the Identification of ADCs with Risk for Poor Pharmacokinetics.....	78
7.2.1. Assay Selection and Test Molecules.....	78
7.2.2. Evaluation of the Self-Interaction Properties of ADCs	81
7.2.3. Investigation of Non-Specific Binding of ADCs	85
7.2.4. Hydrophobicity of ADCs Analyzed by Bis-ANS.....	89
7.2.5. huFcRn Affinity Chromatography.....	91
7.2.6. Comparison of Different <i>In Vitro</i> Assays	94
7.2.7. Correlation of <i>In Vitro</i> Assay Results with <i>In Vivo</i> Pharmacokinetics.....	96
8..... OUTLOOK.....	100
9..... REFERENCES.....	102
10.... APPENDIX.....	115
10.1. Abbreviations	120
10.2. List of Figures.....	126



10.3. List of Tables	128
10.4. Acknowledgements	129
11....AFFIRMATIONS.....	132

2. Abstract

Antibody-drug conjugates (ADCs) are a promising and fast-growing class of targeted anti-cancer therapeutics. They consist of highly potent chemotherapeutic drugs that are covalently linked to monoclonal antibodies (mAbs) which guide the drug to cancer cells. The concept of targeted delivery of a chemotherapeutic agent via an ADC aims at enhanced therapeutic efficacy and safety compared to the individual components of an ADC - the mAb and cytotoxic agent. Despite various successful ADC approvals, their development is complex and associated with a high risk of costly late-stage failures. It has been shown that the overall design of an ADC and every component can influence the critical physicochemical properties which in turn can lead to fast non-specific clearance of the ADCs. Elevated non-specific clearance can directly affect the efficacy and safety and limit the therapeutic window of ADCs. To address this problem, the aim of this study was to evaluate physicochemical property assays that indicate a risk for poor pharmacokinetics (PK) of ADCs.

Physicochemical property assays were applied to an ADC series to evaluate whether ADC hydrophobicity (hydrophobic interaction chromatography (HIC)), thermal stability (nano differential scanning fluorimetry (nanoDSF)), and the binding behavior to the human neonatal Fc-receptor (huFcRn; huFcRn binding kinetics by Bio-Layer Interferometry (BLI)) could serve as an indicator of the PK of the ADCs that was analyzed in huFcRn transgenic Tg276 mice. For this, eight trastuzumab-based ADCs with a homogenous DAR of 2 (drug-to-antibody ratio of 2) were generated by conjugation to cysteines, genetically introduced at positions N325, L328, S239, D265, or S442, and by enzymatic conjugation via microbial transglutaminase (mTG) either to C-terminal light (LC) or heavy chain (HC) recognition motifs or to the endogenous position Q295 of the native antibody. Interestingly, pronounced differences in the ADC PK profiles were observed which allowed to confirm the recently described position L328 as favorable site for cysteine conjugation, comparable to the well-established position S239, and emphasizes the favorable position Q295 of native antibodies and the tagged LC antibody variant for enzymatic conjugations via mTG. Furthermore, to explore if conjugation site and method effects would apply to antibody scaffolds other than trastuzumab, two of the positions, L328 and the mTG LC variant, were evaluated in context of the clinically evaluated mAbs briakinumab and secukinumab. This showed that the influence of conjugation sites and methods on PK resulted in same ADC PK rankings also for briakinumab- and secukinumab-based variants. Physicochemical property assay data were obtained for all study ADCs and correlated with ADC clearance (CL) that serves as important PK parameter. Interestingly, similar huFcRn binding and differently pronounced hydrophobicity and thermal stabilities were observed which did not correlate with the ADC CL values.

Consequently, additional physicochemical property assays were explored in this study that could serve as indicators for poor PK of ADCs and that were adapted from various reports where they allowed prediction of

poor PK of mAbs. To enable a more robust correlation between PK and the *in vitro* assay outcome, 13 ADCs were used that varied not only in the conjugation site and method but also in the DAR and antibody scaffold and for which a broad range of CL values (1.18-8.38 mL/h/kg) were observed in hemizygous huFcRn Tg276 mice. These ADCs were assessed by seven physicochemical property assays that were implemented to analyze either the degree of self-association (clone self-interaction Bio-Layer Interferometry (CSI-BLI) and affinity-capture self-interaction nanoparticle spectroscopy (AC-SINS)), non-specific binding (polyspecificity reagent Bio-Layer Interferometry (PSR-BLI), baculovirus particle (BVP) and heparin enzyme-linked immunosorbent assay (ELISA)), hydrophobicity (bis-ANS), or huFcRn binding (huFcRn affinity chromatography). Assay data was used for the correlation to CL values. Overall, ADCs with lower CL showed lower assay results compared to ADCs with fast CL (about >4 mL/h/kg) which showed elevated assay results. These results indicate for the first time that the selected *in vitro* assays could be a powerful tool for the early development not only for mAbs but also for ADCs allowing the selection of ADCs with favorable PK characteristics. Consequently, application of the *in vitro* assay panel could serve as screening paradigm for PK risk mitigation during early ADC development. However, further work is needed to expand the data set and to conduct robust statistical analyses which could serve as basis to define thresholds for each assay.

3. Zusammenfassung

Antikörper-Wirkstoff-Konjugate (ADCs) sind eine vielversprechende und schnell wachsende Klasse innerhalb der zielgerichteten Krebstherapeutika. Sie bestehen aus hochwirksamen Chemotherapeutika, die kovalent an monoklonale Antikörper (mAbs) gebunden sind, welche das Chemotherapeutikum zu den Krebszellen transportieren. Das Konzept der gezielten Zustellung eines Chemotherapeutikums über ein ADC ermöglicht eine verbesserte therapeutische Wirksamkeit und Sicherheit im Vergleich zu den einzelnen Komponenten eines ADC - dem mAb und dem zytotoxischen Wirkstoff. Obwohl bereits verschiedene ADCs erfolgreichen zugelassen wurden, ist deren Entwicklung komplex und mit einem hohen Risiko kostspieliger Fehlschläge in späten Entwicklungsstadien verbunden. Es hat sich gezeigt, dass das Gesamtdesign eines ADCs und ebenso jede einzelne Komponente die kritischen physikochemischen Eigenschaften des ADCs beeinflussen können, was wiederum zu einer schnellen unspezifischen Clearance der ADCs führen kann. Eine erhöhte unspezifische Clearance kann sich direkt auf die Wirksamkeit und Sicherheit auswirken und das therapeutische Fenster des ADCs verkleinern. Um dieses Problem zu adressieren, war das Ziel dieser Studie Methoden zu bewerten mit denen sich physikochemische Eigenschaften von ADCs analysieren lassen und die genutzt werden könnten, um auf ein Risiko für eine schlechte Pharmakokinetik (PK) der ADCs hinzuweisen.

Diese Methoden wurde auf eine Serie von ADCs angewandt, um zu bewerten, ob die Hydrophobizität (Hydrophobe Interaktionschromatographie (HIC)) und thermische Stabilität (*nano differential scanning fluorimetry* (nanoDSF)) der ADCs sowie das Bindungsverhalten an den human neonatalen Fc-Rezeptor (huFcRn; huFcRn Bindungskinetik mittels *Bio-Layer-Interferometrie* (BLI)) Hinweise auf die PK der ADCs geben können, die in huFcRn-transgenen Tg276-Mäusen analysiert wurden. Zu diesem Zweck wurden acht Trastuzumab-basierte ADCs mit einer homogenen DAR von 2 (Wirkstoff-Antikörper-Verhältnis von 2) hergestellt. Die Konjugation erfolgte entweder an Cysteine, die genetisch an den Positionen N325, L328, S239, D265 oder S442 eingefügt wurden, oder enzymatisch mittels mikrobieller Transglutaminase (mTG) entweder an C-terminale Erkennungsmotive der leichten (LC) oder schweren Kette (HC) oder an die endogene Position Q295 des nativen Antikörpers. Interessanterweise wurden deutliche Unterschiede in den PK-Profilen der ADCs beobachtet, die es ermöglichten die kürzlich beschriebene Position L328 als geeignete Stelle für die Cystein-Konjugation zu bestätigen, vergleichbar mit der gut etablierten Position S239. Darüber hinaus ermöglichte dies die Eignung der Position Q295 des nativen Antikörpers und der mit Erkennungsmotiv generierter LC-Antikörpervariante für enzymatische Konjugationen via mTG hervorzuheben. Um zu untersuchen, ob die Auswirkungen der Konjugationsstelle und -methode auch für andere Antikörpergerüste als Trastuzumab gelten, wurden zwei der Positionen, L328 und die mTG-LC-Variante, zusätzlich im Zusammenhang mit den klinisch evaluierten mAbs Briakinumab und Secukinumab bewertet. Dabei zeigte

sich, dass auch bei den Briakinumab- und Secukinumab-basierten Varianten der Einfluss der Konjugationsstellen und -Methoden auf die PK zu einer gleichen Rangfolge in der PK führte. Für alle ADCs wurden Daten zu ihren physikochemischen Eigenschaften mit den oben genannten Methoden erhoben und mit der ADC Clearance korreliert, da die Clearance (CL) ein wichtiger PK-Parameter ist. Interessanterweise wurde jedoch eine ähnliche huFcRn-Bindung und unterschiedlich ausgeprägte Hydrophobizität und thermische Stabilitäten beobachtet, die nicht mit den CL-Werten der ADCs korrelierten.

Folglich wurden in dieser Studie zusätzliche Methoden auf ihre Eignung als Indikator für ein schlechtes PK-Verhalten von ADCs untersucht, die aus verschiedenen Berichten adaptiert wurden, in denen sie eine Vorhersage der schlechten PK von mAbs ermöglichten. Um eine robustere Korrelation zwischen der PK und den Ergebnissen der *In-vitro* Methoden zu ermöglichen, wurden 13 ADCs verwendet, die sich nicht nur in der Konjugationsposition und Konjugationsmethode, sondern auch in ihrer DAR und dem Antikörpergerüst unterschieden und für die in hemizygoten huFcRn-Tg276-Mäusen ein breites Spektrum an CL-Werten (1,18-8,38 ml/h/kg) beobachtet wurde. Die unterschiedlichen physikochemischen Eigenschaften dieser ADCs wurden mittels sieben verschiedener Methoden bewertet. Diese wurden implementiert, um entweder den Grad der Selbstassoziation (Klon-Selbstinteraktions *Bio-Layer-Interferometrie* (CSI-BLI) und *Affinity Capture* Selbstinteraktions-Nanopartikel-Spektroskopie (AC-SINCS)), der unspezifischen Bindung (Polyspezifitätsreagenz *Bio-Layer-Interferometrie* (PSR-BLI), Baculoviren-Partikel (BVP) und Heparin-*Enzyme-linked immunosorbent Assay* (ELISA)), der Hydrophobizität (bis-ANS) oder der huFcRn-Bindung (huFcRn-Affinitäts-Chromatographie) der ADCs zu analysieren. Die Daten aus den Analysen wurden für die Korrelation mit den CL-Werten verwendet. Insgesamt zeigten ADCs mit niedriger CL auch niedrigere Ergebnisse in den Tests, während im Vergleich dazu ADCs mit schneller CL (in etwa >4 ml/h/kg) höhere Test-Ergebnisse aufwiesen.

Diese Ergebnisse deuten zum ersten Mal darauf hin, dass die ausgewählten *In-vitro*-Methoden ein leistungsfähiges Instrument für die frühe Entwicklung nicht nur von mAbs, sondern auch von ADCs sein könnten, da sie ermöglichen ADCs mit günstigen PK-Eigenschaften auszuwählen. Folglich könnte die Anwendung dieser *In-vitro*-Methoden als *Screening-Paradigma* für die PK-Risikominimierung während der frühen ADC-Entwicklung dienen. Allerdings sind noch weitere Arbeiten erforderlich, um den Datensatz zu erweitern und robuste statistische Analysen durchzuführen, die als Grundlage für die Festlegung von Grenzwerten für jeden Assay dienen könnten.

4. Introduction

Parts of this work have been published.¹

4.1. Antibody-Drug Conjugates

Cancer is one of leading causes of premature death worldwide and is expected to become the leading cause in most countries during this century.² In the field of anti-cancer therapeutics, ADCs are a promising and fast-growing class. By March 2022, a total of eleven different ADCs had been approved by the US Food and Drug Administration (FDA) including seven new approvals since 2019.³ Furthermore, more than 80 ADCs are under clinical development, emphasizing the great potential of this therapeutic modality.⁴

An ADC is formed by covalently attaching a potent chemotherapeutic toxin to a mAb. While therapeutic mAbs alone often exhibit insufficient cytotoxic activity, the relatively non-specific acting but very cytotoxic chemotherapeutic agents (also named drugs or payloads) not only damage cancer but also healthy tissue. ADCs overcome this drawbacks since the mAb specifically targets tumor cells and therefore acts as carrier for the cytotoxic drug allowing for sufficient killing of tumor cells while damage of healthy cells can be prevented.⁵ Compared to rather unselective chemotherapeutic agents, this specific targeting results in a lower minimum effective dose (MED) and higher maximum tolerated dose (MTD, **Figure 1**). Thus, the range of doses with greatest therapeutic effect and without unacceptable side-effects, termed therapeutic window, is expanded enabling the administration of efficient doses with less side effects. However, this concept is not universally applicable. Because an ADC carries a highly cytotoxic small molecule the selection of an appropriate target antigen is extremely important. The target antigen should be only minimal present on healthy tissue cells, to prevent side-effects, but sufficiently present on tumor cells, to enable an effective ADC activity. Moreover, target antigens should be chosen that lead to an efficient internalization of the formed antigen-ADC-complex into the cell as a requisite of the ADC mechanism of action (MoA), which is described in detail in the next section.

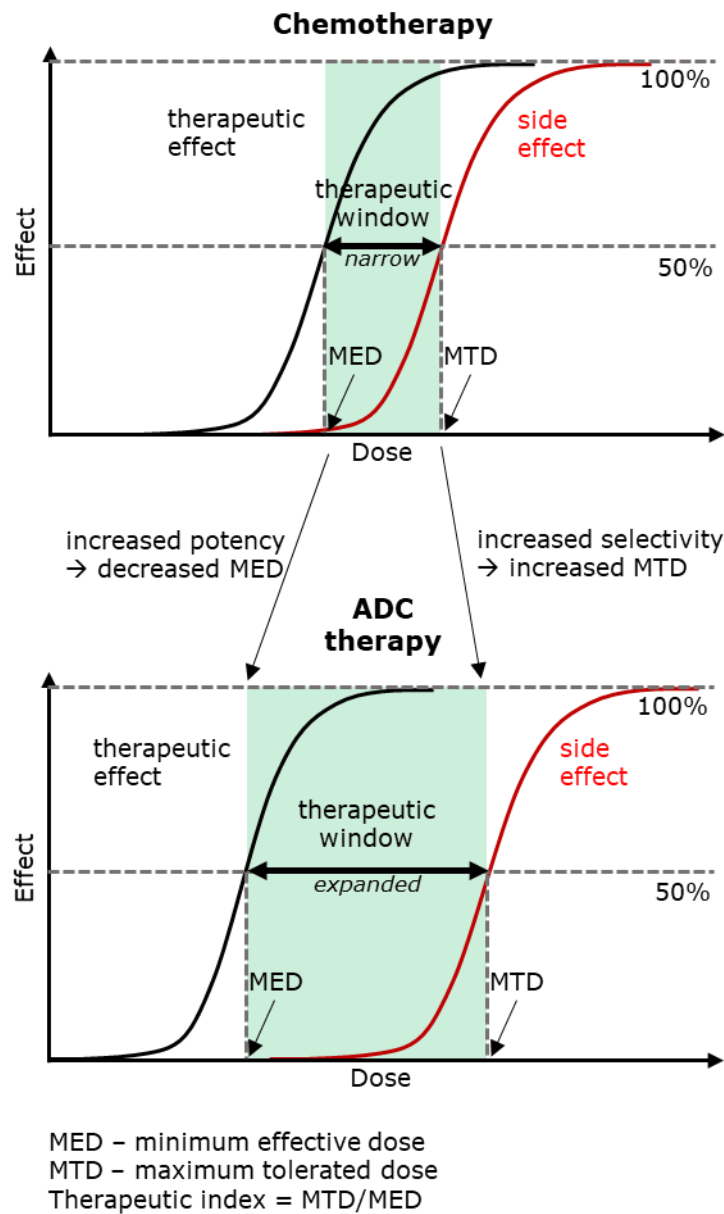


Figure 1. Comparison of the therapeutic windows of a conventional chemotherapy and ADC therapy. Because of the specific delivery of the toxin to the tumor by ADCs the minimum effective dose (MED) is decreased as it leads to an increased potency. In addition, the maximum tolerated dose (MTD) is increased because less non-target cells are reached. Therefore, by using ADCs the therapeutic window, the range of doses with greatest therapeutic effect and without unacceptable side-effects, can be expanded compared to chemotherapeutic drugs. The schematic representation was adapted from Panowski *et al.* and Tarcza *et al.*^{6,7}

4.1.1.1. Mechanism of Action of ADCs.

To specifically damage cancer tissue, an ADC has to reach its cellular expressed target-antigen after intravenous administration. After binding to its target, the formed complex gets internalized via receptor-mediated endocytosis, followed by endosomal trafficking and final localization in the lysosome (**Figure 2**).

Upon lysosomal degradation of the ADC by proteolytic digestion, the payload gets released, followed by diffusion to its cellular target. Various ADC payloads were described targeting tubulin or the DNA in the nucleus which results ultimately in apoptosis of the cell. Furthermore, the payload may also diffuse into cells that are in close proximity to the targeted cell and mediate the so called bystander killing effect.⁸ Since the mAb moiety is of specific interest in the present work, the structure and function of antibodies will be explained in more detail in the following.

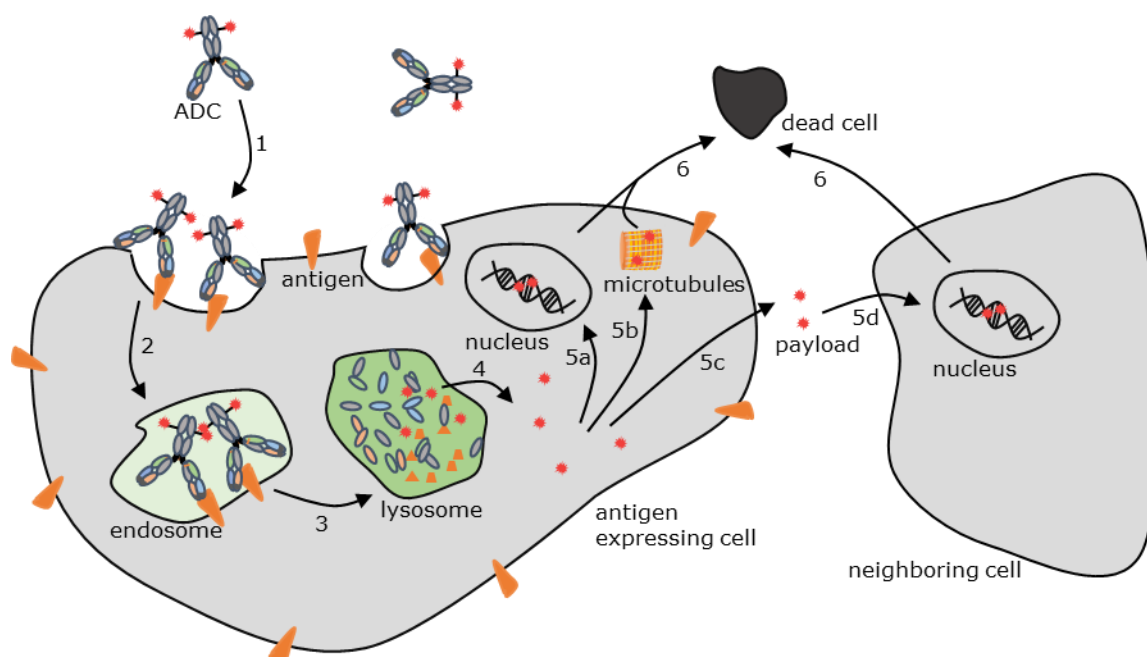


Figure 2. ADC mode of action. The ADC binds to the cell-surface antigen via the mAb component (1). The antigen-ADC complex gets internalized by receptor-mediated endocytosis (2) and reaches the endosome. (3) The payload gets released in the lysosome by ADC degradation and/or by cleavage of the linker by proteases. The free cytotoxin can then diffuse from the lysosome into the cytosol where it can bind to its drug target, for example to DNA in the nucleus (5a) or to microtubule (5b) in the cytosol resulting in cell death (6). Hydrophobic and charge-neutral payloads may diffuse out of the target-expressing (tumor) cell (5c), followed by passive transport into neighboring cells (5d), causing cell death of cells in proximity of the target cell (6; the so called “bystander effect”). Figure adapted according to Kitson *et al.*⁹

4.1.2. Structure and Function of Antibodies

Most ADCs utilize the immunoglobulin G (IgG) isotype as antibody scaffold, which consists of four polypeptide chains with a total molecular weight of approximately 150 kDa. The four chains comprise two identical light chains (LC, ~25 kDa) and two identical heavy chains (HC, ~50 kDa) that are connected via non-covalent interactions and disulfide bonds (interchain disulfide bonds). Furthermore, the LCs and HCs can be separated into different domains. Each chain contains a variable domain (HC: V_H and LC: V_L) that carries three hypervariable complementary-determining regions (CDRs) which enable antigen binding and constant domains (HC: three domains C_{H1} , C_{H2} , and C_{H3} and LC: one $C_L \kappa$ or $C_L \lambda$ domain). The C_{H2} and C_{H3} domains of

both HCs can mediate effector functions like antibody-dependent cell-mediated cytotoxicity (ADCC) and complement-dependent cytotoxicity (CDC) by binding to surface receptors of cells of the immune system (FcγR) or to components of the complement system (C1q).^{10,11} Additionally, this region interacts with the neonatal Fc receptor (FcRn) which is critical for the elimination half-life of the mAb (see section 4.3.1). The characteristic bivalent Y-shaped form of an antibody is caused by the highly flexible hinge region located between the C_{H1} and C_{H2} domain in which the two heavy chains are connected via disulfide bonds. Cleavage of the hinge region by papain separates IgG molecules into two identical Fab domains (fragment of antibody binding, each ~ 50 kDa) consisting of the LC paired with the V_H and C_{H1} and into one Fc domain (fragment crystalline, ~ 50 kDa) comprising the C_{H1} and C_{H2} of both HCs.¹⁰ Furthermore, IgGs are glycoproteins that contain at least one conserved glycosylation site located in the C_{H2} domain at position N297 (**Figure 3**). In total four subclasses of IgG are known, namely IgG1, IgG2, IgG3, and IgG4, that differ in length of the hinge region, in their effector functions, and in the number of inter-chain disulfides. Except for the IgG3 subtype, all subclasses were used for applications as therapeutic mAbs, depending, for instance, on the mode of action or the target.¹² Interestingly, different subclasses were also used for the clinical development of ADCs. At this, nine of eleven ADCs that were clinically approved compose a IgG1 antibody scaffold whereas two ADCs include the IgG4 subclass.^{13,14}

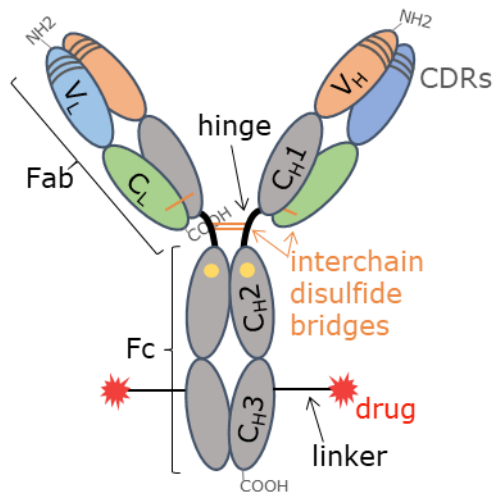


Figure 3. Schematic representation of an ADC. The ADC consists of an antibody equipped with cytotoxic payload that is attached via a linker. The IgG molecule consists of two identical light chains colored in blue (V_L) and green (C_L) and of two identical heavy chains colored in orange (V_H) and gray (C_{H1}, C_{H2}, and C_{H3}) that are connected via disulfide bonds. C_{H1} and C_{H2} of the HCs are separated by the highly flexible hinge region. Hypervariable complementary determining regions (CDR) for antigen recognition within the V_H and V_L are marked in grey and the conserved glycosylation position (N297) in the C_{H2} is marked as yellow point. By papain digestion the antibody is separated into one Fc fragment (fragment crystalline) and two Fab fragments (fragment of antibody binding).

4.1.3. Clinically Approved ADCs

The concept of a tumor-selective delivery of toxin was already envisioned in 1913 by Paul Ehrlich. However, it took until the year 2000 when the first ADC was clinically approved (Mylotarg[®], gemtuzumab ozogamicin). Ten years later, Mylotarg[®] was withdrawn from the market because of risk concerns and lack of sufficient clinical benefit. This example illustrates that the clinical development of ADCs is very challenging.^{15,16} The growing success of ADCs in the last years indicated by the eleven ADCs approved by the FDA today (**Table 1**) and many more already in clinical development is caused by the growing understanding of the major role of the different ADC design parameters and their interplay. While for most of the initially approved ADCs, like Mylotarg[®] and Kadcyra[®], the linker-payload is conjugated randomly to lysine-residues resulting in a heterogeneous ADC product, approved ADCs in recent days, like Padcev[®] and Enhertu[®], were generated with a technique where the linker-payload is attached to reduced interchain-cysteines yielding more homogenous ADCs with a DAR of 4 or 8.^{7,15} More information about the clinically approved ADCs by the FDA are shown in **Table 1**, whereas the improvements made during the past decades leading to the growing success of ADCs are highlighted in the next chapter.

4.2. ADC Design Features to Improve the Therapeutic Window

4.2.1. Antibody

Without the advancements in the antibody field, the development of successful ADCs would not have been possible. A first important step for the development of successful therapeutic antibodies was done in 1975 by Köhler and Milstein who developed the hybridoma technology.¹⁷ This technology enabled the generation of monoclonal antibodies that are specific for a single epitope of an antigen.¹⁸ However, the early mAbs produced by this technique were of non-human origin leading to immunogenicity issues in humans.¹⁹ To overcome these problems and to enhance the generation process, several powerful tools were developed and improved in the last decades. Such tools include different humanization techniques, the use of transgenic mice and rats bearing the genetic human antibody repertoire, the use of sequencing technologies, antibody expression systems, display systems that allow the selection of antibodies with specific properties out of synthetic, immunized, or naïve repertoires, and Fc engineering techniques.²⁰⁻²⁵ All these techniques and many more led to the optimization of antibody features, its production, and characterization and contributed to the great success of therapeutic mAbs today. Beyond this, further research is ongoing to improve the efficacy and safety of therapeutic antibodies, which is also important to improve ADCs. One example is the development of bispecific antibodies (BsAbs) that are generated with two different binding sites and thus can target two different epitopes of one antigen or two different antigens.^{26,27}

Table 1. FDA approved ADCs.^{3,7,13} Mylotarg[®] was first approved in 2000 but withdrawn from the market in 2010 and re-approved in 2017.¹³

ADC Name	Approval Year	Indication	Target	mAb	Conjugation	Linker	Drug	DAR
Gemtuzumab ozogamicin (Mylotarg [®])	2000/2017	AML	CD33	IgG4	Lys	hydrazone disulfide (C)	calicheamicin	2.5
Brentuximab vedotin (Adcetris [®])	2011	HL, ALCL	CD30	IgG1	Cys	VC (C)	MMAE	4
Trastuzumab emtansine (Kadcyla [®])	2013	HER2+ breast cancer	HER2	IgG1	Lys	MCC (NC)	DM1	3.5
Inotuzumab ozogamicin (Besponsa [®])	2017	ALL	CD22	IgG4	Lys	hydrazone disulfide (C)	calicheamicin	6
Polatuzumab vedotin (Polivy [®])	2019	DLBCL	CD79b	IgG1	Cys	VC (C)	MMAE	3.5
Enfortumab vedotin (Padcev [®])	2019	urothelial cancer	Nectin-4	IgG1	Cys	VC (C)	MMAE	4
Trastuzumab deruxtecan (Enhertu [®])	2019	HER2+ breast cancer	HER2	IgG1	Cys	GGPG (C)	DXd	8
Sacituzumab govitecan (Trodelvy [®])	2020	TNBC	Trop-2	IgG1	Cys	CL2A (C)	SN-38	7.6
Belantamab mafodotin (Blenrep [®])	2020	multiple myeloma	BCMA	IgG1	Cys	MC (NC)	MMAF	3-4
Loncastuximab tesirine (Zylonta [®])	2021	DLBCL	CD19	IgG1	Cys	VA (C)	PBD	2.3
Tisotumab vedotin (Tivdak [®])	2021	cervical cancer	TF	IgG1	Cys	VC (C)	MMAE	4

Abbreviations: ALCL - anaplastic large-cell lymphoma; ALL - acute lymphoblastic leukemia; AML - acute myeloid leukemia; BCMA - B-cell maturation antigen; C - cleavable linker; CD - cluster of differentiation; CL2A - cleavable PEG8- and triazole-containing PABC-peptide-MC linker; Cys - interchain cysteine conjugation; DLBCL - diffuse large B cell lymphoma; DM1 - derivate of maytansine; DXd - exatecan derivate; GGPG - glycine-glycine-phenylalanine-glycine; HER2 - human epidermal growth factor receptor 2; HL - Hodgkin lymphoma; Lys - random lysine conjugation; MC - maleimidocaproyl; MCC - 4-maleimidomethyl cyclohexane-1-carboxylate; MMAE - monomethyl auristatin E; MMAF - monomethyl auristatin F; NC - non-cleavable linker; PBD - pyrrolobenzodiazepine; SN38 - active metabolite of the topoisomerase I inhibitor irinotecan; TF - tissue factor; TNBC - triple negative breast cancer; TROP-2 - tumor-associated calcium signal transducer 2; VA - valine-alanine; VC - valine-citrulline.

The advantage of BsAbs over monospecific antibodies can be an increase in target-specificity, efficacy, and a reduction in the occurrence of antibody resistance mechanisms. In the last decade the development of BsAbs has been extensively improved and BsAbs are now in the focus for the generation of ADCs.^{27,28} In May 2022 already four bispecific ADCs had a clinically active status.²⁹

The importance and impact of the antibody scaffold on ADC characteristics was already extensively reviewed elsewhere and for more information the reader is referred to several excellent reviews, for example, by Hoffmann *et al.* and by Tiller and Tessier.^{30,31} In addition to the antibody scaffold, ADC characteristics are also governed by the choice of payload, which will be the focus of the next section.

4.2.2. Cytotoxic Drug

The first ADCs were based on approved chemotherapeutic drugs like the tubulin inhibitor vinblastine.¹⁵ However, these ADCs failed due to their insufficient potency and it became evident that the payload needs to be highly cytotoxic with potencies in the sub-nanomolar to picomolar range as only a limited number of payloads reaches the target cell.³² Further criteria that were found to be important are: (1) a payload needs a chemical attachment site for the covalent connection with a linker that should not alter the cytotoxic activity, (2) a payload should be chemically stable and soluble under physiological conditions, (3) it should not negatively influence the internalization properties of the mAb, (4) it should be no substrate for the efflux mediating multidrug resistance protein 1 (MDR1), which can confer resistance, and (5) the payload should be relatively hydrophilic to prevent ADC aggregation and precipitation.^{4,33,34} However, many potent drugs, as for example, the often used auristatin monomethyl auristatin E (MMAE), are hydrophobic.^{33,35} Excessive hydrophobicity can decrease the solubility and increase the tendency to aggregate which in turn can limit the drug load of ADCs due to elevated toxicity and faster elimination from the circulation.^{33,35,36}

The payloads of the marketed ADCs (**Table 1**) can be divided into three classes: (1) tubulin inhibitors including the auristatins MMAE and MMAF as well as the maytansinoid DM1, (2) DNA damaging drugs (calicheamicin and the pyrrolobenzodiazepine (PBD)-Dimer SG3199), and (3) DNA topoisomerase I inhibitors (SN-38 and DXd).⁷ Beyond these payloads, research is ongoing to improve the toxic component of an ADC, for example, to increase the therapeutic window, to be more effective against slow growing or non-proliferating tumors, and to overcome drug-resistances caused by efflux pumps.³⁷ At this, several payloads are investigated preclinically and clinically comprising different structural variants and classes of tubulin and DNA damaging drugs as well as drugs targeting different essential biological mechanisms, for example, α -amanitin that inhibits the RNA polymerase II.^{37,38}

4.2.3. Linker

In line with progress made for the mAb and payload component of an ADC, the linker was continuously improved as well. The properties of a linker connecting the mAb and payload can significantly influence the toxicity, potency, and pharmacokinetic (PK) properties of an ADC.^{13,15} A linker needs to be stable in the bloodstream to prevent the pre-mature release of the cytotoxin, which could damage healthy cells, and is required to efficiently release the active drug within the tumor cell upon internalization of the ADC. Linkers can be either cleavable or non-cleavable. It was shown in several studies that non-cleavable linkers, like the succinimidyl 4-(*N*-maleimidomethyl)cyclohexane-1-carboxylate (SMCC) linker of Kadcyra[®], are usually more stable in the circulation, which can reduce off-target toxicity and broaden the therapeutic window of the ADC.³⁹ After internalization into the target cell, the antibody portion of an ADC with a non-cleavable linker needs to be degraded in the lysosome to release the payload. Typically, amino acid residues remain associated with the payload-linker construct after lysosomal antibody digestion. Therefore, non-cleavable linkers are not suitable for all payloads as the potency must be maintained with possible substitutions.³⁹ In contrast to their non-cleavable counterparts, cleavable linkers release their payloads traceless. Different linker types have been developed to prevent premature cleavage in the circulation and allow an efficient payload release in target cells. Here, several characteristics of the lysosomal environment can be utilized to achieve selective linker cleavage such as acidic pH, high glutathione concentrations, or hydrolytic enzymes.⁴⁰ For example, one of the most prominent cleavable linker was designed for cleavage by Cathepsin B (CatB) that is an ubiquitous cysteine protease expressed in mammalian cells and overexpressed in several cancer indications. CatB is mainly located in the lysosome and was only found extracellularly in metastatic tumors and in tissue altered by rheumatoid arthritis conditions.^{41,42} One frequently used CatB motif is the valine-citrulline (VC) dipeptide in combination with para-aminobenzyl alcohol (PAB), a self-immolative spacer located between the dipeptide and the payload that enables release of the unmodified payload after cleavage (**Figure 4**).⁴³ Although designed for CatB cleavage, it has been shown that the VC motif can be cleaved by additional lysosomal cathepsins and even by an extracellular enzyme, namely the rodent-specific Carboxylesterase 1C (Ces1C).^{44,45} The extracellular cleavage by Ces1C is not expected to be relevant for humans or other non-rodent species like cynomolgus monkeys, but it can hamper the preclinical development of ADCs in rodents since it can lead to an instability of the linker in the rodent plasma resulting in a reduced potency.⁴⁵ To prevent misleading selections of ADCs with Ces1C cleavable linkers in mouse models, transgenic Ces1C-knockout mice became available.⁴⁶ Moreover, modification of the linker by increasing the hydrophilicity of the linker at the position in front of the valine residue has been shown to prevent Ces1C cleavage while maintaining efficient CatB cleavage.^{43,45}

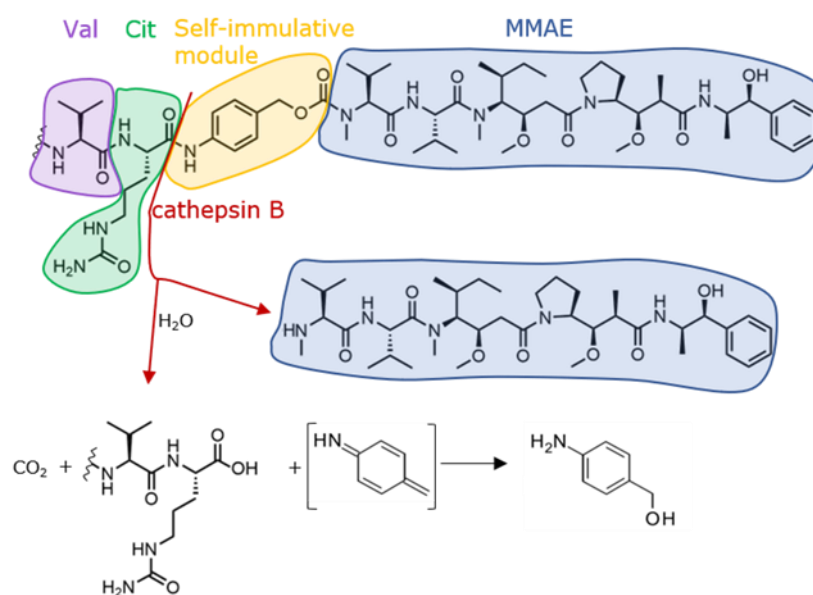


Figure 4. Chemical structure of the cleavable dipeptide linker VC-PAB-MMAE. Attachment of the linker to the mAb is via the moiety bound at the N-terminus of the valine (violet; not shown here). After the dipeptide, valine (violet)-citrulline (green), a self-immolative module (yellow) is attached, followed by the cytotoxic payload MMAE (blue). The linker can be cleaved by lysosomal cathepsin B (CatB) which leads to the decay of the self-immolative module and traceless release of MMAE. In addition to CatB, the lysosomal proteases Cathepsin K and L and the rodent Carboxylesterase 1C (Ces1C) can cleave the linker at the same site.^{44,45}

As already mentioned, an increased hydrophobicity of ADCs is associated with increased clearance, reduced conjugation efficacy, and increased off-target toxicity but hydrophobicity is an intrinsic property of most used potent payloads. Here, the linker design can play a crucial role in reducing the overall hydrophobicity of the ADC, for example, by incorporation of polyethylenglycol (PEG) into the linker.^{35,40,47}

4.2.4. Conjugation Strategy

In various studies it was demonstrated that the attachment of the linker-payload to the mAb is of utmost importance for the generation of active and safe ADCs.^{7,48} Initially, ADCs were generated by chemically coupling of the linker-payload to random lysine residues or interchain cysteines of the mAb. Stochastic conjugation to lysine residues or interchain cysteines results in a heterogenous mixture of different ADCs with different drug loads where different conjugation sites were employed (**Figure 5**). For lysine coupling in each mAb, approximately 40 different lysine residues are available for conjugation, whereas for the interchain cysteine coupling this number is already significantly reduced to eight possible conjugation sites per mAb.⁶ It was found that addressing different conjugation sites can result in ADC species with varying efficacy, PK behavior, and safety.^{36,49,50} To overcome the challenges associated with heterogenous ADC

products, several new site-specific conjugation strategies have been developed to allow generation of homogenous ADCs (**Figure 5**).⁵¹ Two of these methods are described in more detail in here:

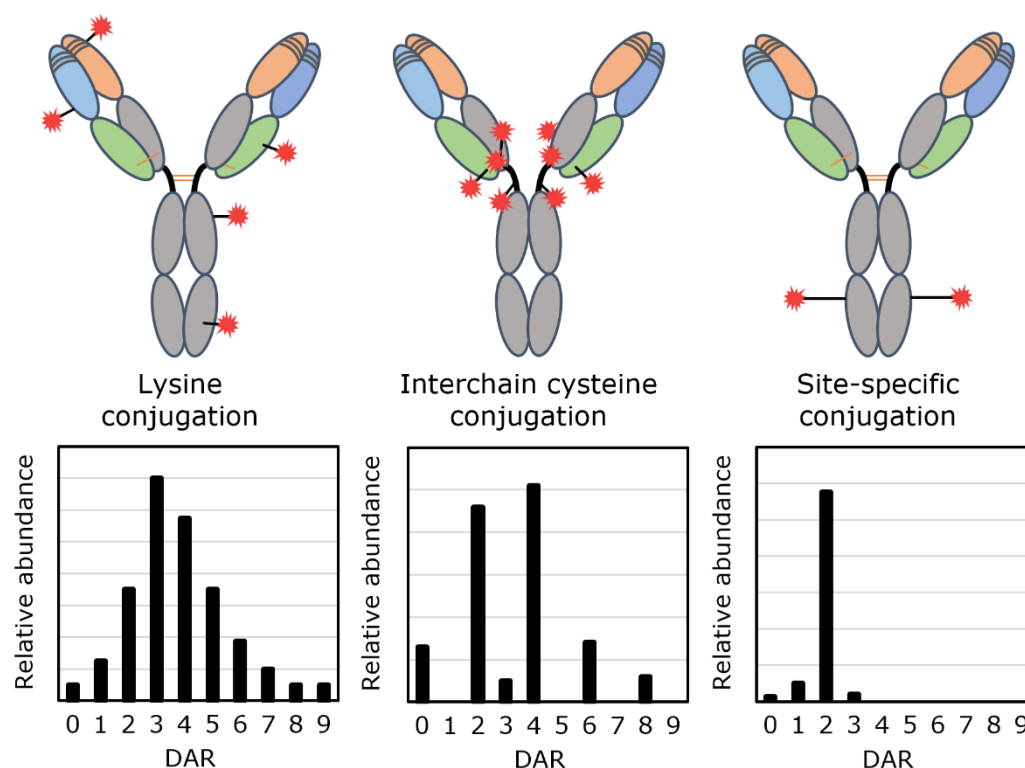


Figure 5. Heterogeneity in the ADC conjugation sites and drug-to-antibody ratio (DAR) of ADCs generated with different conjugation techniques. Lysine conjugation targets randomly ~40 lysine residues in a mAb, interchain cysteine conjugation the eight cysteine residues of the interchain disulfide bridges that are getting reduced for the conjugation, and site-specific conjugation techniques, like engineered cysteine or microbial transglutaminase conjugation, specific positions within the antibody sequence. Figure adapted according to Kaur *et al.*⁵²

Site-Specific Conjugation to Engineered Cysteines

A widely employed method to generate ADCs with defined DAR and conjugation site is the engineered cysteine technology. Instead of using the native cysteines, additional cysteine residues are genetically incorporated into the mAb sequence that can be specifically used for the conjugation to maleimide- or disulfide-functionalized linker-payloads (**Figure 6**).^{50,53} Therefore, mild conditions for the required reduction-oxidation step have been developed to enable that only engineered cysteines are available for conjugation.^{15,50,54} In 2008, Junutula *et al.* showed that ADCs (THIOMAB™) generated by this technique can exhibit improved safety and PK compared to conventional interchain disulfide conjugated ADCs.⁵⁰ However, the site of conjugation has to be chosen with care to allow efficient conjugation, to not alter antigen binding, and to preserve the mAb folding and assembly.^{50,53,55} It was also shown that the cysteine position heavily impacts ADC stability which directly correlated with *in vivo* activity.^{49,56–58} While ADC instability is typically

caused by disturbed protein integrity, maleimide-conjugates can additionally suffer from premature linker-payload deconjugation by retro-Michael elimination.^{49,50,56–58} This process especially occurs in the presence of free sulfhydryl groups as found in serum, for example, in human serum albumin, but strongly depends on the conjugation site.^{49,59} While some positions favor deconjugation, others actually stabilize the conjugate by promoting hydrolysis of the thiosuccinimide ring preventing retro-Michael elimination (**Figure 6**).^{49,60}

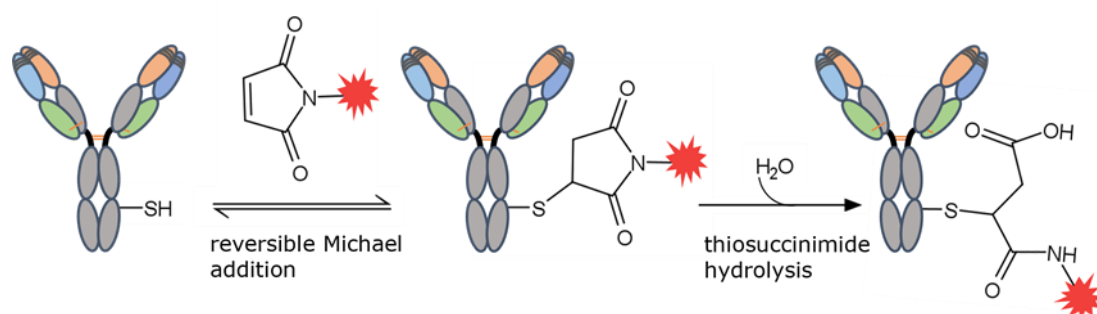


Figure 6. Cysteine conjugated ADCs with maleimide-based linkers. The linker-payload gets conjugated to the antibody via reversible Michael addition. Hydrolysis of the formed unstable thiosuccinimide ring prevents retro-Michael elimination. Figure adapted according to Akkapeddi *et al.*⁶¹

Several positions for efficient engineered cysteine conjugation have been described so far.^{56,62–64} For instance, multiple ADCs against different targets have been conjugated with highly cytotoxic PBD dimers at position S239C (EU numbering is used for all positions described in this work) and showed strong antitumor activity against several cancer- and patient-derived cell lines *in vitro* and in *in vivo* xenograft models.^{65–69} Furthermore, a PK behavior similar to the parental unconjugated mAb was described for one of these ADCs suggesting that the linker-PBD had no impact on the PK at this position.⁶⁵ Consequently, all five S239C-conjugated ADCs have been assessed at least in phase 1 clinical trials already.^{33,66,70–72} To increase the DAR from 2 to 4, position S239C was even combined with a second position S442C in a HER2-bispecific ADC conjugated to a tubulysin-based microtubule inhibitor payload (MEDI4276) that was evaluated in a phase 1/2 clinical trial.^{73,74} In comparison to the clinical approved HER2-targeting ado-trastuzumab emtansine (T-DM1), MEDI4276 showed improved potency in different HER2 expressing cell lines and patient-derived xenograft models, including T-DM1 resistant models.⁷⁴ Another example is position D265C which has been used for conjugation of amanitin-based linker-payloads. These ADCs were well-tolerated in pre-clinical studies in mice and non-human primates.^{75,76} Two recently discovered positions are N325C and L328C, which have been described by Wozniak-Knopp *et al.*⁷⁷ ADCs conjugated at these positions showed promising *in vitro* behavior but have not been assessed *in vivo* so far.⁷⁷

Site-Specific Conjugation via Microbial Transglutaminase

A prominent enzyme-driven approach for site-specific ADC conjugation relies on microbial transglutaminase (mTG). This enzyme, derived from *Streptomyces mobaraensis*, catalyzes the formation of stable isopeptide bonds between glutamine residues and acyl-acceptor substrates (Figure 7).⁷⁸ mTG conjugation of antibodies is either facilitated by mAb deglycosylation, which enables linker-payload attachment to endogenous Q295, or by genetic insertion of mTG recognition motifs (for example, LLQG) into the mAb sequence.^{79,80} Recently, Dickgiesser *et al.* reported engineered mTG mutants that allow conjugation to position Q295 of native, fully glycosylated mAbs.⁸¹

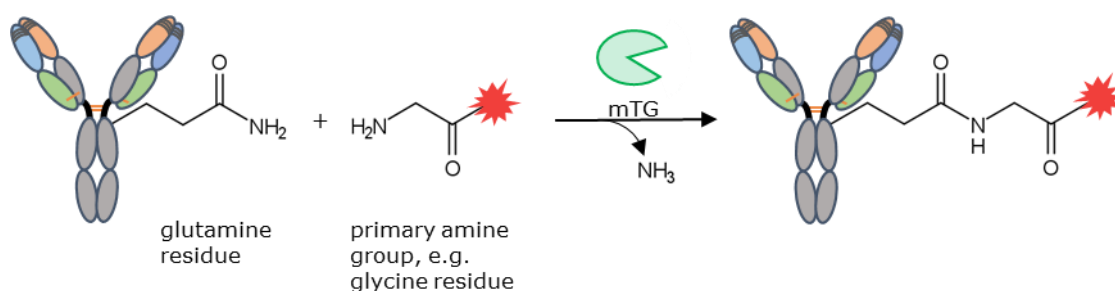


Figure 7. ADCs generation via microbial transglutaminase (mTG). The mTG forms a stable isopeptide bond between a glutamine residue (acyl donor) in the mAb and the primary amine group (acyl acceptor) of a linker-payload. Figure adapted according to Strop *et al.*⁸²

It was reported that conjugation by mTG even enabled the generation of ADCs with high drug load (DAR 6 and DAR 8) with favorable properties.⁸³ Compared to a corresponding conventional interchain cysteine coupled DAR 8 ADC, these ADCs showed a similar safety profile in mice but were more efficacious and cleared slower in mice and rats.⁸³ Moreover, the authors showed that not only the single site of conjugation but also the combination of sites can impact the PK.^{80,83} In addition, like ADCs conjugated at engineered cysteines, also mTG conjugated ADCs showed a conjugation site dependent instability.⁸⁰ In contrast to cysteine conjugated ADCs a stable isopeptide bond is formed between the linker and the mAb hence no chemical instability can be observed. Instead, the observed instabilities were attributed to a differential accessibility of the linker to the murine protease Ces1C, which can cleave certain dipeptide linkers as already mentioned above.^{45,80,84,85} Especially ADCs conjugated to peptide motifs fused to the HC (RN927C) or the LC (RN765C) C-termini, and to position Q295 of aglycosylated mAbs (PF-06888667) were stable, safe, and highly efficacious in xenograft models and RN927C even entered clinical trial.^{86–89}

4.3. Elimination of ADCs from the Blood Stream

One very important factor sensitively impacting efficacy and safety is the duration of the ADC in the circulation which can be described by an important pharmacokinetic parameter, namely the clearance. The clearance is defined as the volume of plasma from which the ADC is completely removed per unit time. A fast decrease of the ADC concentration in plasma implies a decrease in the concentration gradient between plasma and the tumor which is causing diffusion of the ADC into the tumor. Therefore, a fast clearance leads to a reduced tumor exposure which can result in a reduced efficacy.⁹⁰⁻⁹² In addition the clearance can be linked to the toxicity of ADCs:

A correlation between the PK (elimination half-life) and safety (highest non-severely toxic dose, HNSTD) in cynomolgus monkeys was reported for two ADC payload classes, for PBD- and tubulysin-based ADCs.⁹³ **Figure 8 a** and **b** illustrate these correlations indicating that ADCs with prolonged half-life show better safety. As shown by **Figure 8 c**, this indication is not only true just for monkey species but also for humans as the HNSTD in cynomolgus monkeys was shown to correlate with the maximum tolerated dose (MTD) in humans.⁹⁴ Although the correlation between ADC PK and safety has been shown with the use of elimination half-life, the following facts suggest that this should also apply to clearance:

Upon drug administration, the drug distributes in the circulation until equilibrium has been reached, followed by the elimination phase where the drug concentration declines. The elimination half-life ($t_{1/2}$) is defined by the time required to reduce the drug concentration in plasma by 50% during the terminal elimination phase. Therefore, the half-life of a molecule depends on the CL and the volume of distribution (V), which is described in the following formula: $t_{1/2} = \ln 2 * V/CL$. Because of the size and polarity of large biomolecules, different mAbs and ADCs have a similar volume of distribution. Their distribution after intravenous administration is confined to the vascular and interstitial space resulting in a low volume of distribution at steady state (V_{ss}) of approximately 3-8 L which is only slightly greater or close to plasma volume.⁹⁵ Because of this similar volume of distribution it can be assumed that the half-life of ADCs is mainly influenced by the clearance and that the reported dependency between ADC safety and half-life is also true for the clearance parameter. Therefore, improving the clearance of ADCs could enhance not only efficacy but also affect the ADC safety and thereby the therapeutic window. One example that supports this assumption was shown by Burke *et al.*, who focused on the optimization of the drug-linker to reduce the ADC hydrophobicity and thus the CL.⁹⁶ In fact, they demonstrated that the incorporation of PEG-chains into the linker reduced ADC hydrophobicity and CL depending on the PEG-chain length. Interestingly, they showed also improved tolerability and efficacy by reduction in CL.⁹⁶ In a subsequent study analyzing the biodistribution and toxicity of the ADCs in rats, the same group showed that the reduced clearance of the less hydrophobic study ADCs was attributed to a reduced non-specific uptake by various cells of the reticuloendothelial system leading to a reduced ADC

catabolism and consequently to a reduced maximal concentration of released payload in tissue, ultimately reducing toxicity.⁹⁷

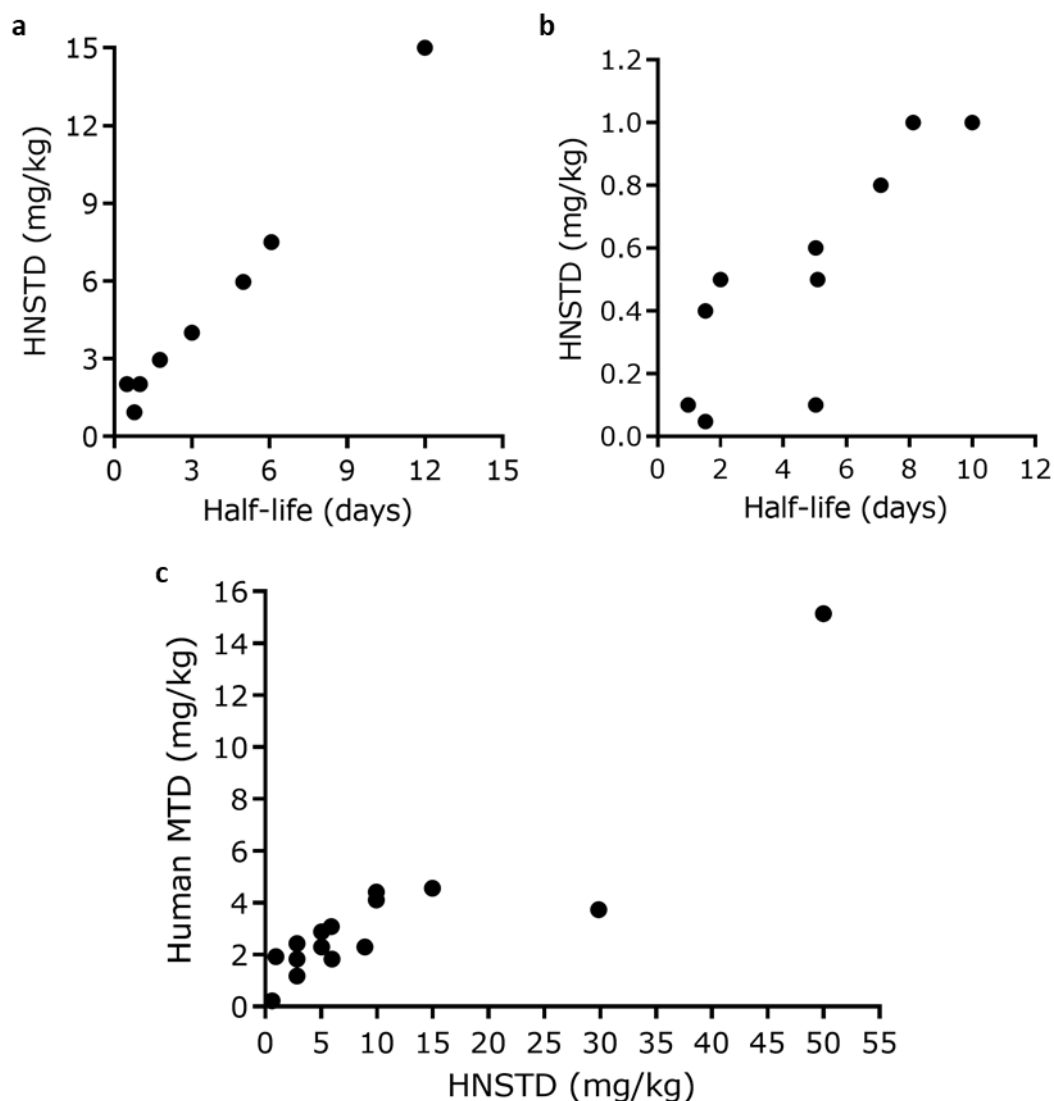


Figure 8. Illustration of the dependency between the PK and safety of ADCs. Shown are correlations between the half-life and highest non-severely toxic dose (HNSTD) of tubulysin- (a) and PBD-based (b) ADCs in cynomolgus monkeys (according to figures shown by R. Dixit at the eighth World ADC conference).⁹³ c) Correlation between the HNSTD in cynomolgus monkeys and the maximum tolerated dose (MTD) in humans of different ADCs, according to H. Saber.⁹⁴

4.3.1. Elimination Mechanisms of ADCs

The main elimination path of ADCs is similar to mAbs driven by catabolic processes that includes cellular uptake and lysosomal degradation as the molecular size of ADCs is too large for elimination by biliary excretion. In addition, ADCs can be eliminated by deconjugation processes causing loss of drug.⁹⁸ As the

deconjugation process was already described in sections 4.2.3 and 4.2.4, this chapter will focus on non-specific catabolic clearance upon cellular uptake.

The uptake of ADCs into cells is mainly mediated by receptor-mediated endocytosis or by pinocytosis. Receptor-mediated endocytosis processes include specific binding to the target receptor or binding to Fc-gamma-receptors (FcγR) which are expressed on cells of the mononuclear phagocytose system and on further immune cells.⁹⁹ Binding to Fcγ receptors is mediated by the C_H2 and C_H3 domains of the mAb (see section 4.1.2) and can differ depending on the IgG isotype and on the mAb glycosylation pattern at the Fc portion.^{100,101} In contrast to receptor-mediated endocytosis, pinocytosis is an unspecific fluid-phase endocytosis mechanism occurring throughout the body.¹⁰² Nevertheless, endogenous IgG have a long serum half-life of approximately 19-23 days in humans.^{103,104}

This prolonged half-life seems to be mainly mediated by the interaction with the neonatal Fc- receptor (FcRn) that rescues IgG from catabolism after uptake by pinocytosis. FcRn is a major histocompatibility complex (MHC) class I-related receptor consisting of an MHC-class-I-like heavy chain (also α chain) and a non-covalently associated β2-macroglobulin (B2M) light chain (β chain) that is expressed in different organs and tissues throughout the body of several different species, mainly in endothelial cells.^{105,106} After uptake via pinocytosis the IgG gets transferred to the endosome where FcRn captures IgG with high affinity at an acidic pH (pH ~6-6.5). This protects the IgG from lysosomal degradation as the FcRn-IgG complex is recycled back to the cell surface where the IgG is released from FcRn due to low affinity at physiological pH (pH 7.4) outside the cell (**Figure 9**).¹⁰² Beside this recycling mechanisms, FcRn can transport IgG across polarized cells via transcytosis.¹⁰⁵ Comparisons between wild type and FcRn-deficient mice have shown that the half-life of IgG in FcRn-deficient mice (~22 h) was significantly reduced compared to the half-life in wild type mice (~ 95 h).^{105,107,108} Furthermore, FcRn is also responsible for the long half-life of serum albumin.¹⁰⁸ As albumin was shown to have a distinct binding site at FcRn this allows for a simultaneous, non-cooperative interaction of FcRn with both, IgG and albumin.^{105,109}

Even though it has been shown that interaction with FcRn plays a major role in non-specific elimination of IgG-based molecules, further physicochemical factors can significantly affect the non-specific clearance including overall non-specific binding, positive charge patches in the variable region, net charge, hydrophobicity, the glycosylation pattern, and specific off-target binding.¹¹⁰⁻¹²¹

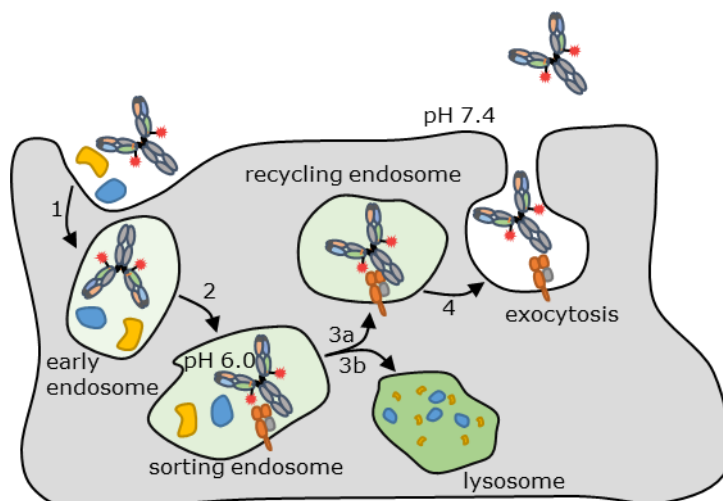


Figure 9. Schematic illustration of the FcRn mediated recycling of Fc-fragment containing molecules. (1) The ADC and serum proteins are taken up by fluid-phase pinocytosis in an early endosome. (2) In the acidified sorting endosome, pH 6.0, the ADC is captured by FcRn at the Fc-portion. The FcRn-ADC complex is sorted (3a) to be recycled back to the cell-surface where the ADC gets released at pH 7.4 (4). (3b) Serum proteins not binding to FcRn finally end up in lysosomes to be degraded. Figure adapted according to Sand *et al.*¹²²

4.3.2. Screening Assays to Identify mAbs and ADCs with Risk for Poor Pharmacokinetics

Because all different components of an ADC can alter the overall physicochemical ADC properties which could lead to fast non-specific clearance and ultimately to a narrow therapeutic window, the risk for cost intensive late-stage failure of ADCs is high. Even though with mAbs the risk of failures is high as poor physicochemical properties can finally lead to an inadequate exposure, lack of efficacy, or toxicity.¹¹¹ Based on these findings, great interest arose to develop screening tools for the identification of mAbs with an inherent risk for a poor PK early in the development. Consequently, several reports about medium- to high-throughput *in vitro* assays that were developed to analyze different physicochemical properties that could influence the PK were published in the recent years. The developed assays included assays to analyze the mAb hydrophobicity, aggregation, self-association, charge, non-specific binding, and interaction with FcRn.^{110,111,115,123} In many of these reports, additionally, successful correlations between the *in vitro* assay results and *in vivo* PK data, named *in vitro in vivo* correlations (IVIVC), of the respective study mAbs were shown.¹¹⁰ The results suggested that the reported *in vitro* assays could be powerful screening tools for the selection of antibodies with presumably good PK.^{110,111,121} Since the aim of this study was to identify *in vitro* physicochemical property assays that would allow the selection of ADCs with presumably good PK, some of these assays are outlined in more detail in this section.

Methods to Analyze the FcRn-Antibody-Interaction

Because of the important role of FcRn recycling for the mAb PK, several efforts were made to analyze the mAb-FcRn interaction. In this context, it was demonstrated in several studies that residues in the antibody Fc region are accountable for the FcRn interaction but that also the variable domain sequence of an antibody can impact the FcRn binding.^{105,124-126} In addition to an efficient binding to FcRn at pH 5-6 in the endosome, a fast dissociation at neutral pH is also of high importance as FcRn is rapidly recycled back to the sorting endosome (within approximately 0.3 s) after reaching the plasma membrane. In case of a slow dissociation, the antibody-FcRn complex would be recycled back into the cell where it could lead to a higher fraction of mAbs degraded in the lysosome.¹²⁶⁻¹²⁸ One method that is frequently used to measure the interaction kinetics (association and dissociation) between mAbs and FcRn at acidic or at neutral pH is surface plasmon resonance (SPR).¹²⁹ Two different setups of this method can be used where FcRn is either in the soluble or in the immobilized form. While in the FcRn soluble setup monovalent binding affinities can be measured, the immobilized setup allows to measure bivalent binding.¹²⁹ In 2011, Wang *et al.* reported for mAbs with identical Fc but different Fab domains a correlation between the dissociation from immobilized FcRn at neutral pH, measured by SPR, and the PK measured in human FcRn transgenic mice, nonhuman primates (NHP), and humans.¹²⁶ As they could not observe a correlation with PK data when performing the SPR measurement with dissociation at pH 6, they suggested that for mAbs with varying Fab domains the dissociation from FcRn at neutral pH seems to be better suitable to assess PK than the pH 6 binding affinity. However, in the case of mAbs having a different Fc but identical Fab domains, they suggested the pH 6 setup for a more robust prediction of their PK behavior.¹²⁶ Beside this report, the relationship between *in vivo* PK results of mAbs and their FcRn binding kinetics measured by SPR has been investigated in many other studies revealing that overall inconsistent results were found regarding the correlations between FcRn binding kinetics measured by SPR and *in vivo* PK data.^{110,121,126,130,131}

Schlothauer *et al.* developed a different method to characterize the mAb-FcRn interaction using a huFcRn affinity chromatography.¹³² By using this method, successful correlations between the FcRn affinity chromatography results (retention time and peak width) of mAbs and their PK in huFcRn transgenic homozygous Tg32 and hemizygous Tg276 mice were described. Here, a longer retention time and a greater peak width indicated a shorter half-life/faster clearance.^{111,124,132} In contrast, for antibodies with specific mutations that change the mAb-FcRn interaction a different relationship was shown, where a longer retention time indicated a longer half-life/slower clearance.¹³² Schlothauer *et al.* supposed that this method may better mimic the physiological pH conditions important for the FcRn interaction, since antibodies were first bound to immobilized huFcRn on the column at pH 5.5 before they got eluted from FcRn by using a pH gradient (pH 5.5 to 8.8).¹³² As a result, molecules with subtle differences in the huFcRn interaction at both,

neutral and acidic pH, can be separated and described by the chromatography retention time and peak width during the elution.¹³²

Methods to Analyze Non-Specific Binding and Self-Association of mAbs

Several *in vitro* high-throughput assays to identify mAbs with risk for poor PK have been reported that focus on the non-specific binding behavior of mAbs.¹¹⁰ For example, Hötzel *et al.* could show that an increased risk for fast CL was associated with an increased non-specific binding to baculovirus particles (BVP) measured by enzyme-linked immunosorbent assay (ELISA) using a series of 45 antibodies with a broad range of CL values in cynomolgus monkeys. That this correlation was also relevant for PK behavior in humans was shown in the same report by successful correlation of BVP ELISA data and CL values measured in humans for 16 molecules.¹²¹ Other assays that were used for successful correlations between non-specific binding and *in vivo* CL were based on heparin interaction,^{115,116} or interaction with cultured adherent human embryonic kidney (HEK) cells,¹¹⁵ DNA,¹¹¹ insulin,¹¹¹ or chaperones to name a few.¹³³ Another important assay from Xu and coworkers was published that can be directly integrated into the antibody screening processes to avoid selection of antibodies with risk for poor PK.¹³⁴ In this yeast-surface based assay, the binding of screened antibodies to polyspecificity reagent (PSR) during the selection process was measured by flow cytometry, where a high binding signal was thought to indicate non-specific binding capacity that was used to exclude those clones with potential poor PK.^{134,135}

Beside methods to measure non-specific binding behavior, further assays were explored that consider self-association properties of mAbs. It was suggested that the self-association properties indicate aggregation tendency and hence are considered as indicator for poor PK.^{119,136} In this context, Liu *et al.* described an improved version of the affinity-capture self-interaction nanoparticle spectroscopy (AC-SINS) assay that can be used to measure self-association of mAbs by capturing them on gold nanoparticles.¹³⁷ Later, Avery *et al.* showed a correlation between the self-association scores determined with this AC-SINS assay and *in vivo* PK determined in homozygous Tg32 mice using several mAbs.¹¹¹

This study by Avery *et al.* was more comprehensive, comprising in total 40 mAbs with available PK data in homozygous Tg32 mice and 38 antibodies with available human PK data including not only the analysis of self-interaction but also other properties described early in this section. In detail, they used the AC-SINS assay to analyze mAb self-association, insulin- and DNA-ELISA to analyze mAb non-specific binding, and FcRn affinity chromatography and SPR to characterize the mAb-FcRn interaction and could show an IVIC with all these assays.¹¹¹ Furthermore, this study demonstrated that it can be advantageous to use a variety of different assays, not only to analyze different physicochemical properties, but also to minimize the risk of

false selections. For instance, it is very unlikely to obtain false positive results in all assays that would indicate a poor PK for a mAb that actually has a good PK.¹¹¹

Although a successful IVIVC has been shown for several different assays that are used to analyze physicochemical properties of mAbs, the correlation is typically not perfectly linear. Therefore, these assays should not be used to predict PK but could be used as screening tools to reject mAbs with potential risk for a poor PK, thereby reducing the number of required preclinical *in vivo* studies.^{111,121}

Methods for ADCs

There is a great demand for the establishment of methods to characterize physicochemical properties of ADCs in order to identify candidates with a risk for poor PK already in the early discovery phase.

Interestingly, for a set of peptide-antibody conjugates a correlation between the results of a cellular uptake assay into hepatocytes and the CL in CD-1 mice was reported recently. In this assay, the depletion of the peptide-antibody conjugates from medium caused by non-specific uptake into hepatocytes was measured.¹³⁸

Another report was published by Lyon *et al.* that highlighted the application of hydrophobic interaction chromatography (HIC) as a tool for PK assessment. Herein, Lyon *et al.* showed a correlation between the PK in BALB/c mice and rats and the apparent hydrophobicity of a set of tool ADCs with different hydrophobic linker-payloads measured by HIC.³⁵ Although this first study highlighted HIC as important method with regard to PK, limitations of the method as a predictive tool were described in a subsequent study where no such correlation was observed for ADCs with linker-payloads equipped with PEG chains of different length.¹³⁹ For these ADCs, an increase of PEG chain length resulted in a decrease of their clearance. However, inconsistent results were found for the HIC analysis: For antibodies conjugated only with the PEG chain, a longer PEG chain resulted in a longer retention time, whereas for the ADCs with payload and PEG chain, the retention time again became shorter with PEG chains of more than four PEG units, presumably caused by the masking of the hydrophobic payload moiety.¹³⁹ In contrast to the HIC retention times, the authors reported a strong correlation between CL in rats and *in vitro* uptake into Kupffer cells using the different PEGylated ADCs.¹³⁹ Although their Kupffer cell assay seems to be a suitable tool for selecting ADCs with good PK at least for the set of PEGylated ADCs, a limitation of this assay is the additional labeling step of the ADC with a fluorescent dye that may impact the physicochemical properties of the ADC.

4.3.3. Human FcRn Transgenic Mouse Models

Although physicochemical *in vitro* assays seem to be helpful to evaluate the potential mAb/ADC PK properties, preclinical animal models are still irreplaceable. In this regard, mice are well-established as

preclinical model for the first *in vivo* validation including PK analysis of the hit candidates.¹⁴⁰ Although wild type mice are heavily used in this context, their applicability for the prediction of PK in humans is rather limited. It was shown that human IgG antibodies bind to mouse FcRn with an even higher affinity than to human FcRn.¹⁴¹ This is highly relevant for analyzing the PK parameters of human IgG-based therapeutic modalities and may contribute to the poor human PK predictability of data generated in wild type rodents.^{140,142} Due to the application of huFcRn transgenic mice, researchers were able to overcome this disadvantage rendering them a suitable model for predictive PK studies.^{140,142} Two prominent strains of huFcRn transgenic mouse models were developed so far that are available as homozygous or hemizygous: Tg276 (B6.Cg-Fcgrt<tm1Dcr> Tg(CAG-FCGRT)276Dcr/DcrJ) or Tg32 (B6.Cg-Fcgrt<tm1Dcr> Tg(FCGRT)32Dcr/DcrJ) mice.¹⁴⁰ The parental mouse strain of both transgenic strains is the C57BL/6J mouse in which most of the murine FcRn gene sequence and its promoter was deleted resulting in a homozygous FcRn null C57BL/6J mouse strain. Therefore, the huFcRn transgenic mice are lacking mouse FcRn. Instead, both strains express the human/mouse heterodimer FcRn receptor with mouse B2M (β chain) and human FcRn (α chain), but the promoters were designed differently: The Tg276 mice express huFcRn under control of a human cytomegalovirus immediate early promoter/enhancer together with a chicken beta-actin/rabbit beta-globin hybrid promoter (CAG), whereas the Tg32 mice express huFcRn under the endogenous huFcRn promoter.¹⁴³ It was shown that the different promoters led to a different FcRn expression pattern in both mice strains. The strong CAG promoter in the Tg276 mice caused a ubiquitous expression of FcRn, also in a variety of additional cell types that lack FcRn expression in human tissue, whereas Tg32 mice demonstrated an FcRn expression pattern similar to that in human and monkey tissues.^{106,144} As mouse IgG binds to huFcRn only with very low affinity, the endogenous IgG levels in both strains are reduced compared to wild type mice. Consequently, the competition for binding to FcRn between endogenous IgG and the administered Fc-molecule of interest is reduced.^{140,141,145,146} However, Tam *et al.* demonstrated for the homozygous Tg32 and Tg276 strains that a pretreatment with intravenous administered human IgG had only little effect on the half-life of the human IgG sample mAb.¹⁴⁶ In contrast, for hemizygous Tg32 mice with less expressed huFcRn, administration of the FcRn binding competitors reduced the half-life of the human IgG1 sample mAb.¹⁴⁶ In line with this, Petkova *et al.* suggested a pretreatment with human IgG for the hemizygous Tg32 mice but considered it as unnecessary for hemi- and homozygous Tg276 mice.¹⁴⁷ Recently, a new transgenic mouse strain, based on the Tg32 mice, was constructed that produces human Fc-mouse Fab2 chimeric IgG1 antibodies (Tg32-hFc) which can act as endogenous competitor for the FcRn binding. Analysis of two different antibodies revealed a reduced half-life and increased CL in the Tg32-hFc strain compared to the Tg32 strain with reduced competition.¹⁴⁸

As mentioned in section 4.3.1, the ability to interact with FcRn is not only responsible for the long serum half-life of IgGs but also for the long serum half-life of serum albumin.¹⁰⁸ For the FcRn binding no competition between IgG and serum albumin is expected as the binding site of serum albumin on FcRn is distinct from the binding site of IgGs.^{105,109} Nevertheless, it cannot be excluded that human serum albumin (HSA) may influence the PK of IgGs but the blood of huFcRn transgenic mice contains mouse serum albumin (MSA) and lacks HSA.^{140,146} However, it was reported that a parallel administration of HSA to the transgenic huFcRn mice (Tg32 homo- and hemizygous, and Tg276 homozygous, which had all similar MSA levels) had no effect on the level of administered human IgG.¹⁴⁶

Another difference between the FcRn expression in human tissues and transgenic mice is that FcRn is expressed as heterodimer in the mice where the human FcRn HC is paired with mouse B2M, resulting in a chimeric receptor with human and mouse FcRn receptor components. However, no detectable differences in the half-life of a human mAb were found in an study that compared Tg32 mice and a constructed Tg32 mice-based strain that expresses not only mouse but also human B2M.¹⁴⁰ Furthermore, the results of various studies indicated the functionality of the heterodimeric receptor, as the PK data in the transgenic mice correlated well to human and non-human primate data.^{140,142,146,149–151}

Because of the differences in FcRn expression induced by the promoters, antibodies are cleared differently in both strains with a faster clearance in the Tg276 mice.^{140,152} At this, fastest antibody clearance was observed in the hemizygous Tg276 mice while the slowest clearance was reported for the homozygous Tg32 mice.^{140,152} One potential advantage of hemizygous Tg276 mouse strain is to better detect subtle differences in antibody PK including those mediated by Fc-engineering.^{126,140,143,147,149,153} Correlation of PK data from the transgenic mice to human and/or monkey data have been shown for all four mouse strains, Tg32 and Tg276, homozygous and hemizygous, respectively.^{126,142,146,149–151,154} Nevertheless, homozygous Tg32 were most frequently used in various studies to predict human PK based on mouse PK data.^{142,146,150,154,155}

4.3.4. Pharmacokinetic Analyses of ADCs

The evaluation of ADC profiles from serum is challenging as catabolic and metabolic processes can modify the ADCs in the blood stream leading to a wide variety of new species that can include modified or (partly) degraded linker-payload species or the formation of novel adduct species.¹⁶ Different methods have been developed for analyzing the ADC PK profiles, where the analysis of free drug species is based on liquid chromatography with tandem mass spectrometry (LC-MS/MS) methods and analysis of all species in which the antibody is present is based on ligand-binding assays (LBAs) and liquid chromatography-mass spectrometry (LC-MS) methods.¹⁵⁶ Commonly PK profiles of ADCs rely on up to four different analytes

including total antibody (1), conjugated antibody (2), antibody-conjugated payload (3), and free drug (4) concentration profiles (**Figure 10**): (1) For the total antibody profile the concentration of all antibodies is measured, regardless of whether a small molecule is associated with the antibody or not. (2) With conjugated antibody assays, only the antibodies are measured that are conjugated to at least one payload. (3) An antibody-conjugated payload profile is obtained by measuring any drug that is associated with the antibody. Here, signals correspond to the overall drug load of the analyte. (4) The content of free drug in the circulation can be analyzed by measuring the unconjugated, free drug.¹⁶

Drug loss and its impact on the PK can be unrevealed by comparing the total antibody and antibody-conjugated payload profiles.¹⁶ At this, average DAR at each timepoint can be calculated by dividing the molar concentration of antibody-conjugated payload by the molar concentration of total-antibody.¹⁶ For a more precise characterization of the DAR, assays using affinity capture combined with LC-MS were developed. These assays allow to analyze the DAR distribution and to quantify the relative amount of the different DAR-species in the samples.^{157–161} Further details regarding different analysis methods and their limitations are already extensively reviewed elsewhere.^{156,162–164}

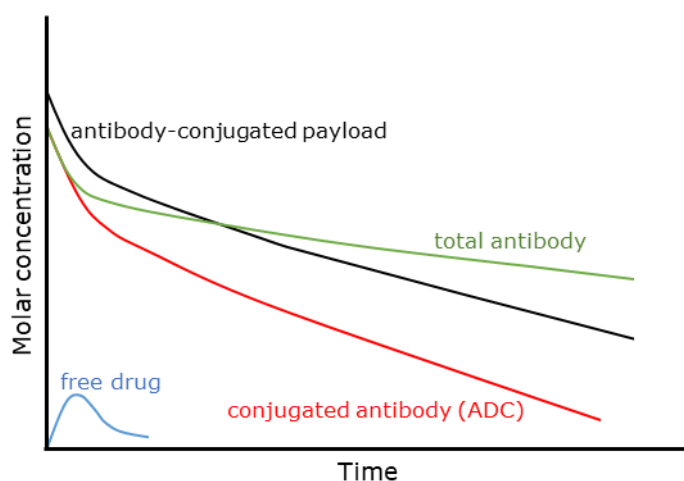


Figure 10. Exemplary pharmacokinetic profiles of ADC analytes. For antibody-conjugated payload profiles (black) all payloads associated with the antibody are quantified. The total antibody profiles (green) are based on the measurement of all DAR species including the unconjugated antibody. In contrast, the conjugated antibody or ADC profiles include all antibody species with at least one associated payload. The blue profile reflects the content of unconjugated payload in plasma/serum. Figure adapted according to Kamath *et al.*¹⁶

5. Objective of this Work

The aim of this study was to evaluate different *in vitro* physicochemical property assays to identify ADCs with risk for poor PK. Up to now, several *in vitro* assays were developed to analyze different physicochemical properties of mAbs that served as screening tools to identify mAbs with fast non-specific clearance/poor PK. However, the assays were never applied to ADCs for this purpose, even though elevated non-specific clearance can directly limit efficacy and safety profiles of ADCs and ultimately leading to a small therapeutic window.

Therefore, the main objective of this work was to adapt the published screening assays and apply them to a series of study ADCs for that different conjugation sites and different conjugated methods, mAb scaffolds and/or DAR were employed. For this purpose, in some cases the assay procedure and data processing had to be optimized for use with ADCs. The assays should be used to analyze the self-association (CSI-BLI and AC-SINS) and the non-specific binding (BVP- and heparin ELISA, PSR-BLI) tendencies of the ADCs and to analyze the hydrophobicity (HIC and bis ANS), thermal stability (nanoDSF), and the huFcRn interaction (huFcRn binding kinetics by BLI and huFcRn affinity chromatography) of the ADCs. Assay data was then used for correlation with ADC PK data (*in vivo* CL) obtained from the hemizygous Tg276 mouse model that is transgenic for huFcRn and was suggested to better predict PK behavior in human than wildtype mice. Analyses of correlations needed to be performed to identify assays that allow for identification of ADC candidates with risk for poor PK.

6. Material and Methods

6.1. Mammalian Cell Lines and Culture Media

Expi293F™ cells (#A14527)	Gibco™ Thermo Fisher Scientific, Waltham, MA, USA
Medium: Expi293F™ Expression Medium	Gibco™ Thermo Fisher Scientific, Waltham, MA, USA
ExpiCHO-S™ cells (# A29127)	Gibco™ Thermo Fisher Scientific, Waltham, MA, USA
Medium: ExpiCHO Expression Medium	Gibco™ Thermo Fisher Scientific, Waltham, MA, USA
HEK293-6E (RRID: CVCL_HF20)	National Research Council (NRC) Canada
Medium: FreeStyle™ F17 supplemented with 4 mM L-Glutamine	Thermo Fisher Scientific, Waltham, MA, USA and Merck, Darmstadt, Germany

6.2. Bacterial Strain

One Shot™ TOP10 chemically competent *E. coli* cells (#C4040-10, Invitrogen™ Thermo Fisher Scientific, Waltham, MA, USA);

Genotype: F- *mcrA* Δ (*mrr-hsdRMS-mcrBC*) ϕ 80*LacZ* Δ M15 Δ *LacX74* *recA1* *araD139* Δ (*araI*) 7697 *galU* *galK* *rpsL* (StrR) *endA1* *nupG*

6.3. Mouse Strain

Tg276 (hemizygous) mice,¹⁴⁰ (#004919, The Jackson Laboratory, Bar Harbor, ME, USA, breeder: Charles River Laboratories Italia, Calco, Italy).

Genotype: B6.Cg-Fcgrt^{tm1Dcr} Tg(CAG-FCGRT)276Dcr/DcrJ, (Homozygous for Fcgrttm1Dcr, Hemizygous for Tg(CAG-FCGRT)276Dcr)

6.4. Antibody Sequences

Amino acid sequences of trastuzumab as published by drug bank accession entry DB00072 in the year 2009.¹⁶⁵ Genetic modifications are marked in bold.

Light chain, unmodified:

DIQMTQSPSSLSASVGDRVTITCRASQDVNTAVAWYQQKPGKAPKLLIYSASFLYSGVPSRFGSRSRGTDFLTISLQPEDF
ATYYCQQHYTTPPTFGQGTKVEIKRTVAAPSVFIFPPSDEQLKSGTASVVCLLNNFYPREAKVQWKVDNALQSGNSQESVT
EQDSKDSTYLSSTLTLSKADYEKHKVYACEVTHQGLSSPVTKSFNRGEC

Light chain with C-terminal mTG recognition motif:

DIQMTQSPSSLSASVGDRVTITCRASQDVNTAVAWYQQKPGKAPKLLIYSASFLYSGVPSRFGSRSRGTDFLTISLQPEDF
ATYYCQQHYTTPPTFGQGTKVEIKRTVAAPSVFIFPPSDEQLKSGTASVVCLLNNFYPREAKVQWKVDNALQSGNSQESVT
EQDSKDSTYLSSTLTLSKADYEKHKVYACEVTHQGLSSPVTKSFNRGEC**GGLLQGPP**

Light chain with C-terminal Sortase A recognition motif and GS-linker:

DIQMTQSPSSLSASVGDRVTITCRASQDVNTAVAWYQQKPGKAPKLLIYSASFLYSGVPSRFGSRSRGTDFLTISLQPEDF
ATYYCQQHYTTPPTFGQGTKVEIKRTVAAPSVFIFPPSDEQLKSGTASVVCLLNNFYPREAKVQWKVDNALQSGNSQESVT
EQDSKDSTYLSSTLTLSKADYEKHKVYACEVTHQGLSSPVTKSFNRGEC**GGGGSGGGGSGGGGSLPETGS**

Heavy chain with Q295A substitution:

EVQLVESGGGLVQPGGSLRLSCAASGFNIKDTYIHWVRQAPGKGLEWVARIYPTNGYTRYADSVKGRFTISADTSKNTAYL
QMNSLRAEDTAVYYCSRWGGDGFYAMDYWGQGLTVTVSSASTKGPSVFPLAPSSKSTSGGTAALGCLVKDYFPEPVTVS
WNSGALTSGVHTFPAVLQSSGLYSLSSVTVPSSSLGTQTYICNVNHKPSNTKVDKKEPPKSCDKHTCPPCPAPELLGGP
SVFLFPPKPKDTLMISRTPEVTCVVVDVSHEDPEVKFNWYVDGVEVHNAKTKPREE**A**YNSTYRVVSVLTVLHQDWLNGKE
YKCKVSNKALPAPIEKTISKAKGQPREPQVYTLPPSRDELTKNQVSLTCLVKGFYPSDIAVEWESNGQPENNYKTTTPVLDSD
GSFFLYSKLTVDKSRWQQGNVFSCSVMHEALHNHYTQKSLSLSPGK

Heavy chain with C-terminal mTG recognition motif:

EVQLVESGGGLVQPGGSLRLSCAASGFNIKDTYIHWVRQAPGKGLEWVARIYPTNGYTRYADSVKGRFTISADTSKNTAYL
QMNSLRAEDTAVYYCSRWGGDGFYAMDYWGQGLTVTVSSASTKGPSVFPLAPSSKSTSGGTAALGCLVKDYFPEPVTVS
WNSGALTSGVHTFPAVLQSSGLYSLSSVTVPSSSLGTQTYICNVNHKPSNTKVDKKEPPKSCDKHTCPPCPAPELLGGP
SVFLFPPKPKDTLMISRTPEVTCVVVDVSHEDPEVKFNWYVDGVEVHNAKTKPREEQYNSTYRVVSVLTVLHQDWLNGKE
YKCKVSNKALPAPIEKTISKAKGQPREPQVYTLPPSRDELTKNQVSLTCLVKGFYPSDIAVEWESNGQPENNYKTTTPVLDSD
GSFFLYSKLTVDKSRWQQGNVFSCSVMHEALHNHYTQKSLSLSPG**LLQGA**

Heavy chain with S239C substitution:

EVQLVESGGGLVQPGGSLRLSCAASGFNIKDTYIHWVRQAPGKGLEWVARIYPTNGYTRYADSVKGRFTISADTSKNTAYL
QMNSLRAEDTAVYYCSRWGGDGFYAMDYWGQGLTVTVSSASTKGPSVFPLAPSSKSTSGGTAALGCLVKDYFPEPVTVS
WNSGALTSGVHTFPAVLQSSGLYSLSSVTVPSSSLGTQTYICNVNHKPSNTKVDKKVEPPKSCDKTHTCPPCPAPELLGGP
CVFLFPPKPKDTLMISRTPEVTCVVDVSHEDPEVKFNWYVDGVEVHNAKTKPREEQYNSTYRVVSVLTVLHQDWLNGKE
YKCKVSNKALPAPIEKTISKAKGQPREPQVYTLPPSRDELTKNQVSLTCLVKGFYPSDIAVEWESNGQPENNYKTTTPVLDSD
GSFFLYSKLTVDKSRWQQGNVFSCSVMHEALHNHYTQKSLSLSPGK

Heavy chain with D265C substitution:

EVQLVESGGGLVQPGGSLRLSCAASGFNIKDTYIHWVRQAPGKGLEWVARIYPTNGYTRYADSVKGRFTISADTSKNTAYL
QMNSLRAEDTAVYYCSRWGGDGFYAMDYWGQGLTVTVSSASTKGPSVFPLAPSSKSTSGGTAALGCLVKDYFPEPVTVS
WNSGALTSGVHTFPAVLQSSGLYSLSSVTVPSSSLGTQTYICNVNHKPSNTKVDKKVEPPKSCDKTHTCPPCPAPELLGGP
SVFLFPPKPKDTLMISRTPEVTCVVV**C**VSHEDPEVKFNWYVDGVEVHNAKTKPREEQYNSTYRVVSVLTVLHQDWLNGKE
YKCKVSNKALPAPIEKTISKAKGQPREPQVYTLPPSRDELTKNQVSLTCLVKGFYPSDIAVEWESNGQPENNYKTTTPVLDSD
GSFFLYSKLTVDKSRWQQGNVFSCSVMHEALHNHYTQKSLSLSPGK

Heavy chain with N325C substitution:

EVQLVESGGGLVQPGGSLRLSCAASGFNIKDTYIHWVRQAPGKGLEWVARIYPTNGYTRYADSVKGRFTISADTSKNTAYL
QMNSLRAEDTAVYYCSRWGGDGFYAMDYWGQGLTVTVSSASTKGPSVFPLAPSSKSTSGGTAALGCLVKDYFPEPVTVS
WNSGALTSGVHTFPAVLQSSGLYSLSSVTVPSSSLGTQTYICNVNHKPSNTKVDKKVEPPKSCDKTHTCPPCPAPELLGGP
SVFLFPPKPKDTLMISRTPEVTCVVDVSHEDPEVKFNWYVDGVEVHNAKTKPREEQYNSTYRVVSVLTVLHQDWLNGKE
YKCKV**S**CALPAPIEKTISKAKGQPREPQVYTLPPSRDELTKNQVSLTCLVKGFYPSDIAVEWESNGQPENNYKTTTPVLDSD
GSFFLYSKLTVDKSRWQQGNVFSCSVMHEALHNHYTQKSLSLSPGK

Heavy chain with L328C substitution:

EVQLVESGGGLVQPGGSLRLSCAASGFNIKDTYIHWVRQAPGKGLEWVARIYPTNGYTRYADSVKGRFTISADTSKNTAYL
QMNSLRAEDTAVYYCSRWGGDGFYAMDYWGQGLTVTVSSASTKGPSVFPLAPSSKSTSGGTAALGCLVKDYFPEPVTVS
WNSGALTSGVHTFPAVLQSSGLYSLSSVTVPSSSLGTQTYICNVNHKPSNTKVDKKVEPPKSCDKTHTCPPCPAPELLGGP
SVFLFPPKPKDTLMISRTPEVTCVVDVSHEDPEVKFNWYVDGVEVHNAKTKPREEQYNSTYRVVSVLTVLHQDWLNGKE
YKCKVSNK**A****C**PAPIEKTISKAKGQPREPQVYTLPPSRDELTKNQVSLTCLVKGFYPSDIAVEWESNGQPENNYKTTTPVLDSD
GSFFLYSKLTVDKSRWQQGNVFSCSVMHEALHNHYTQKSLSLSPGK

Heavy chain with S442C substitution:

EVQLVESGGGLVQPGGSLRLSCAASGFNIKDTYIHWVRQAPGKGLEWVARIYPTNGYTRYADSVKGRFTISADTSKNTAYL
QMNSLRAEDTAVYYCSRWGGDGFYAMDYWGQGLTVTVSSASTKGPSVFPLAPSSKSTSGGTAALGCLVKDYFPEPVTVS
WNSGALTSVHTFPAVLQSSGLYSLSSVTVPSSSLGTQTYICNVNHKPSNTKVDKKVEPPKSCDKTHTCPPCPAPELLGGP
SVFLFPPKPKDTLMISRTPEVTCVVDVSHEDPEVKFNWYVDGVEVHNAKTKPREEQYNSTYRVVSVLTVLHQDWLNGKE
YKCKVSNKALPAPIEKTISKAKGQPREPQVYTLPPSRDELTKNQVSLTCLVKGFYPSDIAVEWESNGQPENNYKTTTPVLDSD
GSFFLYSKLTVDKSRWQQGNVFSCSVMHEALHNHYTQKSLSLCPGK

Amino acid sequences of briakinumab (briakinumab VH¹⁶⁶ on human IgG Fc and VL¹⁶⁶ on human lambda light chain constant region). Genetic modifications are marked in bold.

Light chain, unmodified:

QSVLTQPPSVSGAPGQRVTISCSGSRNIGSNTVKWYQQLPGTAPKLLIYNDQRPSGVPDRFSGSKSGTSASLAITGLQAE
DEADYYCQSYDRYTHPALLFGTGKVTVLGQPKAAPSVTLFPPSSEELQANKATLVCLISDFYPGAVTVAWKADSSPVKAGV
ETTPSKQSNNKYAASSYLSLTPEQWKSHKSYSCQVTHEGSTVEKTVAPTECS

Light chain with C-terminal mTG recognition motif:

QSVLTQPPSVSGAPGQRVTISCSGSRNIGSNTVKWYQQLPGTAPKLLIYNDQRPSGVPDRFSGSKSGTSASLAITGLQAE
DEADYYCQSYDRYTHPALLFGTGKVTVLGQPKAAPSVTLFPPSSEELQANKATLVCLISDFYPGAVTVAWKADSSPVKAGV
ETTPSKQSNNKYAASSYLSLTPEQWKSHKSYSCQVTHEGSTVEKTVAPTECS**GGLLQGGP**

Heavy chain, unmodified:

QVQLVESGGGVVQPGRSLRLSCAASGFTSSYGMHWVRQAPGKLEWVAFIRYDGSNKYYADSVKGRFTISRDNKNTLY
LQMNSLRAEDTAVYYCKTHGSHDNWGQGMVTVSSASTKGPSVFPLAPSSKSTSGGTAALGCLVKDYFPEPVTVSWNSG
ALTSVHTFPAVLQSSGLYSLSSVTVPSSSLGTQTYICNVNHKPSNTKVDKRVKPKSCDKTHTCPPCPAPELLGGPSVFLFPP
KPKDTLMISRTPEVTCVVDVSHEDPEVKFNWYVDGVEVHNAKTKPREEQYNSTYRVVSVLTVLHQDWLNGKEYKCKVSN
KALPAPIEKTISKAKGQPREPQVYTLPPSREEMTKNQVSLTCLVKGFYPSDIAVEWESNGQPENNYKTTTPVLDSDGSFFLY
SKLTVDKSRWQQGNVFSCSVMHEALHNHYTQKSLSLSPG

Heavy chain with Q295A substitution:

QVQLVESGGGVVQPGRSLRLSCAASGFTFSSYGMHWVRQAPGKGLEWVAFIRYDGSNKYYADSVKGRFTISRDN SKNTLY
LQMNSLRAEDTAVYYCKTHGSHDNWGQGTMTVSSASTKGPSVFPLAPSSKSTSGGTAALGCLVKDYFPEPVTVSWNSG
ALTSGVHTFPAVLQSSGLYSLSSVVTVPSSSLGTQTYICNVNHKPSNTKVDKRVEPKSCDKTHTCPPCPAPELLGGPVFLFPPK
PKDTLMISRTPEVTCVVDVSHEDPEVKFNWYVDGVEVHNAKTKPREE**A**YNSTYRVVSVLTVLHQDWLNGKEYKCKVSN
KALPAPIEKTISKAKGQPREPQVYTLPPSREEMTKNQVSLTCLVKGFYPSDIAVEWESNGQPENNYKTTTPVLDSDGSFFLYS
KLTVDKSRWQQGNVFCFSVMHEALHNHYTQKSLSLSPG

Heavy chain with L328C substitution:

QVQLVESGGGVVQPGRSLRLSCAASGFTFSSYGMHWVRQAPGKGLEWVAFIRYDGSNKYYADSVKGRFTISRDN SKNTLY
LQMNSLRAEDTAVYYCKTHGSHDNWGQGTMTVSSASTKGPSVFPLAPSSKSTSGGTAALGCLVKDYFPEPVTVSWNSG
ALTSGVHTFPAVLQSSGLYSLSSVVTVPSSSLGTQTYICNVNHKPSNTKVDKRVEPKSCDKTHTCPPCPAPELLGGPSVFLFPP
KPKDTLMISRTPEVTCVVDVSHEDPEVKFNWYVDGVEVHNAKTKPREEQYNSTYRVVSVLTVLHQDWLNGKEYKCKVSN
KAC**P**APIEKTISKAKGQPREPQVYTLPPSREEMTKNQVSLTCLVKGFYPSDIAVEWESNGQPENNYKTTTPVLDSDGSFFL
YSKLTVDKSRWQQGNVFCFSVMHEALHNHYTQKSLSLSPG

Amino acid sequences of secukinumab (secukinumab VH¹⁶⁷ on human IgG Fc and VL¹⁶⁷ on human kappa light chain constant region). Genetic modifications are marked in bold.

Light chain, unmodified:

EIVLTQSPGTLSSLSPGERATLSCRASQSVSSSYLAWYQQKPGQAPRLLIYGASSRATGIPDRFSGSGSGTDFTLTISRLE
PEDFAVYYCQQYGSSPCTFGQGRLEIKRTVAAPSVFIFPPSDEQLKSGTASVVCLLNNFYPRKAVQWKVDNALQSGNSQ
ESVTEQDSKDYSLSTLTLSKADYEKHKVYACEVTHQGLSSPVTKSFNRGEC

Light chain with C-terminal mTG recognition motif:

EIVLTQSPGTLSSLSPGERATLSCRASQSVSSSYLAWYQQKPGQAPRLLIYGASSRATGIPDRFSGSGSGTDFTLTISRLEPEDFA
VYYCQQYGSSPCTFGQGRLEIKRTVAAPSVFIFPPSDEQLKSGTASVVCLLNNFYPRKAVQWKVDNALQSGNSQESVTE
QDSKDYSLSTLTLSKADYEKHKVYACEVTHQGLSSPVTKSFNRGEC**GGLLQGP**P

Heavy chain, unmodified:

EVQLVESGGGLVQPGGSLRLSCAASGFTFSNYWMNWRQAPGKGLEWVAAINQDGSEKYYVGSVKGRFTISRDNKNSL
YMQMNSLRVEDTAVYYCVRDYYDILTDYYIHYYWYFDLWGRGTLTVSSASTKGPSVFPLAPSSKSTSGGTAALGCLVKDYFP
EPVTVSWNSGALTSGVHTFPAVLQSSGLYSLSSVTVPSSSLGTQTYICNVNHKPSNTKVDKRVEPKSCDKTHTCPPCPAPE
LLGGPSVFLFPPKPKDTLMISRTPEVTCVVVDVSHEDPEVKFNWYVDGVEVHNAKTKPREEQYNSTYRVVSVLTVLHQDW
LNGKEYKCKVSNKALPAPIEKTISKAKGQPREPQVYTLPPSREEMTKNQVSLTCLVKGFYPSDIAVEWESNGQPENNYKTPP
PVLDSGDGSFFLYSKLTVDKSRWQQGNVDFCSVMHEALHNHYTQKSLSLSPG

Heavy chain with Q295A substitution:

EVQLVESGGGLVQPGGSLRLSCAASGFTFSNYWMNWRQAPGKGLEWVAAINQDGSEKYYVGSVKGRFTISRDNKNSL
YMQMNSLRVEDTAVYYCVRDYYDILTDYYIHYYWYFDLWGRGTLTVSSASTKGPSVFPLAPSSKSTSGGTAALGCLVKDYFP
EPVTVSWNSGALTSGVHTFPAVLQSSGLYSLSSVTVPSSSLGTQTYICNVNHKPSNTKVDKRVEPKSCDKTHTCPPCPAPE
LLGGPSVFLFPPKPKDTLMISRTPEVTCVVVDVSHEDPEVKFNWYVDGVEVHNAKTKPREEAYNSTYRVVSVLTVLHQDW
LNGKEYKCKVSNKALPAPIEKTISKAKGQPREPQVYTLPPSREEMTKNQVSLTCLVKGFYPSDIAVEWESNGQPENNYKTPP
PVLDSGDGSFFLYSKLTVDKSRWQQGNVDFCSVMHEALHNHYTQKSLSLSPG

Heavy chain with L328C substitution:

EVQLVESGGGLVQPGGSLRLSCAASGFTFSNYWMNWRQAPGKGLEWVAAINQDGSEKYYVGSVKGRFTISRDNKNSL
YMQMNSLRVEDTAVYYCVRDYYDILTDYYIHYYWYFDLWGRGTLTVSSASTKGPSVFPLAPSSKSTSGGTAALGCLVKDYFP
EPVTVSWNSGALTSGVHTFPAVLQSSGLYSLSSVTVPSSSLGTQTYICNVNHKPSNTKVDKRVEPKSCDKTHTCPPCPAPE
LLGGPSVFLFPPKPKDTLMISRTPEVTCVVVDVSHEDPEVKFNWYVDGVEVHNAKTKPREEQYNSTYRVVSVLTVLHQDW
LNGKEYKCKVSNKACPAPIEKTISKAKGQPREPQVYTLPPSREEMTKNQVSLTCLVKGFYPSDIAVEWESNGQPENNYKTPP
PVLDSGDGSFFLYSKLTVDKSRWQQGNVDFCSVMHEALHNHYTQKSLSLSPG

Typically, the coding DNA sequences of the amino acid sequences of the HCs and LCs were codon-optimized for mammalian expression. The expression plasmids, based on a pTT5 plasmid with a cytomegalovirus immediate early (CMV) promoter and an ampicillin resistance gene, were produced by GeneArt (Thermo Fisher Scientific). In addition to the antibodies shown above, further antibodies targeting EGFR, HER2, MUC1, ROR1, and TAA were used and kindly provided from Merck KGaA research programs.

6.5. Commercial Antibodies

AffiniPure goat anti-human IgG, Fcγ fragment specific (#109-005-098)	Jackson ImmunoResearch Europe, Cambridgeshire, GB
AffiniPure mouse anti-human IgG, F(ab') ₂ fragment specific (#209-005-097)	Jackson ImmunoResearch Europe, Cambridgeshire, GB
Anti-MMAE monoclonal antibody, clone 2E2, (#MAB30699)	Epitope Diagnostics, San Diego, CA, USA
Biotin-SP (long spacer) AffiniPure goat anti-human IgG, Fcγ fragment specific (#209-065-098)	Jackson ImmunoResearch Europe, Cambridgeshire, GB
ChromPure Goat IgG, whole molecule (#005-000-003)	Jackson ImmunoResearch Europe, Cambridgeshire, GB
peroxidase-AffiniPure F(ab') ₂ fragment goat anti-mouse IgG, Fcγ fragment specific (#109-036-098)	Jackson ImmunoResearch Europe, Cambridgeshire, GB
peroxidase-AffiniPure goat anti-mouse IgG (H+L), (#115-035-062)	Jackson ImmunoResearch Europe, Cambridgeshire, GB
peroxidase-AffiniPure goat anti-mouse IgG, F(ab') ₂ fragment specific, (#115-035-072)	Jackson ImmunoResearch Europe, Cambridgeshire, GB
Trastuzumab (Herceptin®)	Roche, Basel, Switzerland

6.6. Enzymes and Proteins

Bovine serum albumin (BSA, #3912)	Sigma Aldrich, St. Louis, MO, USA
Bovine serum albumin (BSA, #A7906)	Sigma Aldrich, St. Louis, MO, USA
Cathepsin B from human liver (#C8571)	Sigma Aldrich, St. Louis, MO, USA
cOmplete™, EDTA-free Protease Inhibitor Cocktail	Roche, Basel, Switzerland
Mouse serum (#S2160)	BioWest, Nuaille, France
Papain, <i>Carica Papaya</i> (#5125)	Sigma Aldrich, St. Louis, MO, USA
Recombinant huFcRn-His ₆	produced in-house; Merck, Darmstadt, Germany
Recombinant Human ErbB2/Her2 Fc Chimera	R&D Systems, Bio-Techne, Minneapolis, MN, USA
Sortase A, recombinant, <i>S. aureus</i>	produced in-house; Merck, Darmstadt, Germany
Transglutaminase, genetically engineered, ⁸¹	produced in-house; Merck, Darmstadt, Germany
Transglutaminase, recombinant, <i>S. mobaraensis</i>	Zedira®, Darmstadt, Germany

6.7. Chemicals

0.1% formic acid in acetonitrile (ACN) ULC/MS - CC/SFC	Biosolve B.V., Valkenswaard, Netherlands
0.1% formic acid in water ULC/MS - CC/SFC	Biosolve B.V., Valkenswaard, Netherlands
1-Step™ Ultra TMB-ELISA Substrate Solution	Thermo Fisher Scientific, Waltham, MA, USA
2-Morpholinoethanesulfonic acid monohydrate (MES)	Merck, Darmstadt, Germany
4,4'-Dianilino-1,1'-binaphthyl-5,5'-disulfonic acid dipotassium salt (bis-ANS)	Sigma Aldrich, St. Louis, MO, USA
Acetic acid (96% solution)	Sigma Aldrich, St. Louis, MO, USA
Acetonitrile (ACN, HPLC grade)	Merck Millipore, Billerica, MA, USA
Agar, extra pure	Merck, Darmstadt, Germany
Ammonium sulfate ((NH ₄) ₂ SO ₄)	Merck, Darmstadt, Germany
Ampicillin, sodium salt	Life Technologies™ Thermo Fisher Scientific, Waltham, MA, USA
Baculovirus particles (BVP)	iBet, Oeiras, Portugal
Calcium chloride (CaCl ₂ ·2H ₂ O)	Merck, Darmstadt, Germany
D8-MMAE	MedChemExpress, Monmouth Junction, NJ, USA
Dimethyl sulfoxide (DMSO, HPLC grade)	Merck Millipore, Billerica, MA, USA
Disodium hydrogen phosphate (Na ₂ HPO ₄)	Merck, Darmstadt, Germany
Dulbecco's Phosphate Buffered Saline (DPBS), w/o Ca ²⁺ and Mg ²⁺	Gibco™ Thermo Fisher Scientific, Waltham, MA, USA
Ethylenediaminetetraacetic acid (EDTA)	Sigma Aldrich, St. Louis, MO, USA
Formic acid (purity 98-100%)	Sigma Aldrich, St. Louis, MO, USA
G ₃ -MMAF	Produced in-house, Merck, Darmstadt, Germany
G ₃ -VC-PAB-MMAE	Moradec LLC, San Diego, CA, USA
G ₃ -VC-PAB-MMAF	Produced in-house, Merck, Darmstadt, Germany
Gel filtration standard (#151-1901)	Bio-Rad, Hercules, CA, USA
Glycerol	Sigma Aldrich, St. Louis, MO, USA
Gold Colloids (Sols) (#15705)	Ted Pella, Redding, CA, USA
Heparin (#H3149)	Sigma Aldrich, St. Louis, MO, USA

HEPES	Sigma-Aldrich, St. Louis, MO, USA
HIC standard	Produced in-house, Merck, Darmstadt, Germany
Hydrochloric acid (HCl); 1 N	Merck, Darmstadt, Germany
Isopropanol (HPLC grade)	Merck Millipore, Billerica, MA, USA
Kalium chloride (KCl)	Merck, Darmstadt, Germany
L-Dehydroascorbic acid (L-DHA)	Sigma Aldrich, St. Louis, MO, USA
Magnesium chloride (MgCl)	Merck, Darmstadt, Germany
MC-VC-PAB-MMAE	Levena Biopharma, San Diego, CA, USA
Methanol (HPLC grade)	Merck Millipore, Billerica, MA, USA
Milli-Q® H ₂ O	Produced in-house, Merck, Darmstadt, Germany
MSD Read Buffer T (4x) with surfactant	Meso Scale Discovery, Rockville, MD, USA
N-acetylcysteine	Sigma Aldrich, St. Louis, MO, USA
n-Dodecyl-β-maltoside (DDM)	Thermo Fisher Scientific, Waltham, MA, USA
Opti-MEM™, reduced serum media	Gibco™ Thermo Fisher Scientific, Waltham, MA, USA
Peptone, from casein	Merck, Darmstadt, Germany
PBS tablets	Gibco™ Thermo Fisher Scientific, Waltham, MA, USA
Poly(ethyleneglycol)methyletherthiol (PEG thiol)	Sigma-Aldrich, St. Louis, MO, USA
Potassium di-hydrogen phosphate (KH ₂ PO ₄)	Merck, Darmstadt, Germany
S.O.C. Medium	Thermo Fisher Scientific, Waltham, MA, USA
Sodium acetate (NaOAc)	Sigma Aldrich, St. Louis, MO, USA
Sodium carbonate (Na ₂ CO ₃)	Merck, Darmstadt, Germany
Sodium chloride (NaCl)	Merck, Darmstadt, Germany
Sodium dihydrogen phosphate (NaH ₂ PO ₄ ·H ₂ O)	Merck, Darmstadt, Germany
Sodium hydrogen carbonate (NaHCO ₃)	Merck, Darmstadt, Germany
Sodium hydroxide (NaOH), 2 N	Merck, Darmstadt, Germany
Sulfuric acid (H ₂ SO ₄), 1N	Bernd Kraft, Oberhausen, Germany
The Blocking Solution	Candor Bioscience, Wangen, Germany
Tris(2-carboxyethyl)phosphine (TCEP); 0.5 M	Sigma Aldrich, St. Louis, MO, USA
Tris(hydroxymethyl)aminomethane (Tris base)	Merck, Darmstadt, Germany
Tris-hydrochloride (Tris HCl)	Sigma Aldrich, St. Louis, MO, USA
Tween® 20 (polysorbate 20)	Merck, Darmstadt, Germany

Yeast extract, granulated

Merck, Darmstadt, Germany

6.8. Prepared Solutions, Buffer, and Media

Unless otherwise stated, Milli-Q® water was used as solvent. Buffers were sterilized by filtration and medium by autoclavation before antibiotic was added.

1 M acetate buffer pH 5.0	37 mM acetic acid, 63 mM NaOAc, pH 5.0
100 mM Sodium-Carbonate-Buffer	20% (v/v) 0.1 M Na ₂ CO ₃ , 80% (v/v) 0.1 M NaHCO ₃ , pH 9.6
2.5% formic acid	2.5% (v/v) formic acid in Milli®-Q water
20 mM acetate buffer pH 4.3	12.8 mM acetic acid, 7.2 mM NaOAc, pH 4.3
2x MSD Read buffer T with surfactant	50% (v/v) MSD Read Buffer T (4x) with surfactant, 50% (v/v) Milli-Q®-water
2xTY-ampicillin selective medium	1.6% (w/v) peptone, 1% (w/v) yeast extract, 0.5% (w/v) NaCl, 100 µg/mL (w/v) ampicillin
BLI blocking buffer	1% (w/v) BSA (A3912) in DPBS
BVP/Heparin ELISA buffer	3% (w/v) BSA (A3912) in DPBS
Cleavage buffer	0.06 units cathepsin B and 9.8 units papain in 1.9 mM EDTA, 9.3 mM TCEP pH 7, 0.7 M acetate buffer pH 5.0
Cysteine conjugation buffer	PBS pH 7.4 + 1 mM EDTA
DPBS pH 7.4	DPBS adjusted with NaOH to pH 7.4
FcRn binding assay buffer (BLI)	50 mM NaH ₂ PO ₄ , 150 mM NaCl, 0.05% (v/v) Tween®20, pH 6.0
FcRn chromatography, mobile phase A	20 mM MES, 150 mM NaCl, pH 5.5
FcRn chromatography, mobile phase B	20 mM Tris base, 150 mM NaCl, pH 8.8
HIC mobile phase A	1.5 M (NH ₄) ₂ SO ₄ , 25 mM Tris HCl, pH 7.5
HIC mobile phase B	20% (v/v) isopropanol, 25 mM Tris HCl, pH 7.5
LB-ampicillin selective agar plates	1.5% (w/v) agar, 1% (w/v) peptone, 0.5% (w/v) yeast extract, 1% (w/v) NaCl, 100 µg/mL (w/v) ampicillin

MS mobile phase	85% 0.1% formic acid in water, 15% 0.1% formic acid in ACN
mTG conjugation buffer	150 mM NaCl, 50 mM Tris HCl, pH 8
PBS pH 7.4 or pH 7.0	137 mM NaCl, 10 mM Na ₂ HPO ₄ ·2H ₂ O, 0.27 mM KCl 1.0 mM KH ₂ PO ₄ , pH 7.4 or pH 7.0
PBS-T1	PBS pH 7.4, 0.5% (v/v) Tween® 20
PBS-T2	PBS pH 7.4, 0.01% (v/v) Tween® 20
Precipitation reagent	10% (v/v) methanol, 90% (v/v) ACN
PSR buffer A	50 mM HEPES, 0.15 mM NaCl, 2 mM CaCl ₂ , 5 mM KCl, 5 mM MgCl ₂ , 10% (v/v) Glycerol, 2.5x protease inhibitor cOmplete, pH 7.2
PSR buffer B	50 mM HEPES, 0.15 mM NaCl, 2 mM CaCl ₂ , 5 mM KCl, 5 mM MgCl ₂ , 1% (w/v) DDM, 1x protease inhibitor cOmplete, pH 7.2
SE-HPLC mobile phase buffer	50 mM sodium phosphate, 0.4 M NaClO ₄ , pH 6.3
SrtA conjugation buffer	150 mM NaCl, 50 mM Tris HCl, pH 7.5
Total antibody LBA, dilution buffer	PBS pH 7.4, 0.05% (v/v) Tween® 20, 3.0% (w/v) BSA (A7906)

6.9. Kits and Consumables

96-well plates, BRANDplates®, pureGrade (#781602)	Brand, Wertheim, Germany
96-well plates, 0.5 mL, round wells, U shape, polypropylene (#5043-9311)	Agilent Technologies, Santa Clara, CA, USA
Amicon® Ultra Centrifugal Filter, molecular weight cut-off (MWCO) 100 kDa and 50 kDa	Merck Millipore, Billerica, MA, USA
BLI biosensor, anti-human IgG Fc capture (AHC)	FortéBio, Fremont, CA, USA
BLI biosensor, Fab-CH1 2 nd Generation (FAB2G)	FortéBio, Fremont, CA, USA
Erlenmeyer shake flask, PC, 0.5 L, 1 L	Corning® Corning, NY, USA
Fisherbrand™ 384-well polystyrene plates (#12-565-506)	Fisher Scientific, Schwerte, Germany
GenElute™ High Performance Plasmid Maxiprep Kit	Sigma Aldrich, St. Louis, MO, USA

HPLC vial caps	VWR International, Radnor, PA, USA
HPLC vials	VWR International, Radnor, PA, USA
HPLC vials micro inserts, 0.1 mL and 0.2 mL	VWR International, Radnor, PA, USA
Microplates 96-well, black, F-bottom, PP (#655209)	Greiner Bio-One, Kremsmünster, Austria
Millex®-GV, 0.22 µm, syringe filter	Merck Millipore, Billerica, MA, USA
MSD GOLD™ 96-well Streptavidin Quickplex® Plates	Meso Scale Discovery, Rockville, MD, USA
MSD GOLD™ SULFO-TAG NHS-Ester	Meso Scale Discovery, Rockville, MD, USA
nanoDSF, standard capillary chips	NanoTemper Technologies, Munich, Germany
Nunc MaxiSorp™ flat-bottom 96-well plates	Invitrogen™ Thermo Fisher Scientific, Waltham, MA, USA
PCR tubes	Thermo Fisher Scientific, Waltham, MA, USA
Pierce™ BCA Protein Assay Kit	Thermo Fisher Scientific, Waltham, MA, USA
Plate sealing, adhesive PCR sealing foil sheet	Thermo Fisher Scientific, Waltham, MA, USA
Protein A Immunocapture Spin Plates	Thermo Fisher Scientific, Waltham, MA, USA
Protein LoBind 96-well plates	Eppendorf, Hamburg, Germany
Protein LoBind tubes 15, 50 mL	Eppendorf, Hamburg, Germany
Protein LoBind tubes, 1.5, 2.0 mL, safe lock	Eppendorf, Hamburg, Germany
PureLink® HiPure Plasmid Midiprep Kit	Invitrogen™ Thermo Fisher Scientific, Waltham, MA, USA
Steriflip™ 0.22 µm, vacuum filter	Merck Millipore, Billerica, MA, USA
Steritop™, 0.22 µm, bottle top filter	Merck Millipore, Billerica, MA, USA
Transfection kit, ExpiFectamine™ 293	Gibco™ Thermo Fisher Scientific, Waltham, MA, USA
Tubes, 1.5, 2.0 mL, safe lock	Eppendorf, Hamburg, Germany
Ultrafree®-CL, 0.22 µm, centrifugal filter	Merck Millipore, Billerica, MA, USA
Zeba™ Spin Desalting Columns, 7K and 40K MWCO	Thermo Fisher Scientific, Waltham, MA, USA

6.10. Equipment

Acquity BEH C18 1.7 µm (2.1 × 100 mm) and (2.1 × 50 mm)	Waters, Milford, CT, USA
Acquity UPLC H-Class system	Waters, Milford, CT, USA
Agilent 1260 Infinity HPLC system	Agilent Technologies, Santa Clara, CA, USA

Agilent 1260 Infinity II HPLC system	Agilent Technologies, Santa Clara, CA, USA
Analytical balance AE200 and AE240	Mettler-Toledo, Columbus, OH, USA
Analytical balance Sartorius Quintix®	Sartorius, Göttingen, Germany
bioZen™ 3.6 µm Intact C4 column (2.1 × 100 mm)	Phenomenex®, Torrance, CA, USA
BLI system, Octet® RED	FortéBio, Fremont, CA, USA
BLI system, Octet® RED96	FortéBio, Fremont, CA, USA
Branson Digital Sonicator with micro-Horn tip 3 mm 1/8''	Branson Ultrasonic, Emerson, St. Louis, MO, USA
Cell viability analyzer Vi-CELL™ XR	Beckmann Coulter, Brea, CA, USA
Centrifuge 5424	Eppendorf, Hamburg, Germany
Centrifuge 5427R	Eppendorf, Hamburg, Germany
Centrifuge 5430R	Eppendorf, Hamburg, Germany
Centrifuge Biofuge Fresco	Heraeus, Hanau, Germany
Centrifuge Heraeus Fresco21	Thermo Fisher Scientific, Waltham, MA, USA
Centrifuge Megafuge 1.0R	Thermo Fisher Scientific, Waltham, MA, USA
Centrifuge Multifuge 3 SR+	Heraeus, Hanau, Germany
Chromatography system ÄKTA avant	GE Healthcare, Buckinghamshire, GB
Chromatography system ÄKTA pure	GE Healthcare, Buckinghamshire, GB
Chromatography system ÄKTAexpress	GE Healthcare, Buckinghamshire, GB
Dounce homogenizers	Carl Roth, Karlsruhe, Germany
Erlenmeyer flasks with baffles	Schott, Mainz, Germany
ExionLC™ system	Shimadzu, Kyoto, Japan
FcRn column (4.6 × 50 mm)	Produced in-house, Merck, Darmstadt, Germany
Fixed angle rotor Sorvall SS-34	Thermo Fisher Scientific, Waltham, MA, USA
Fixed angle rotor T-647.5	Thermo Fisher Scientific, Waltham, MA, USA
HiLoad™ Superdex 200 pg column (16 × 600 mm) and (26 × 600 mm)	GE Healthcare, Buckinghamshire, GB
HiPrep™ 26/10 desalting column	GE Healthcare, Buckinghamshire, GB
HiTrap™ desalting column, 5 mL	GE Healthcare, Buckinghamshire, GB
HiTrap™ MabSelect™ SuRe™ column, 5 mL	GE Healthcare, Buckinghamshire, GB
Incubation shaker Multitron	Infors HT, Bottmingen, Switzerland
Incubator BBD 6220	Thermo Fisher Scientific, Waltham, MA, USA
Incubator Heracell™ 150	Thermo Fisher Scientific, Waltham, MA, USA



Incubator Heracell™ VIOS 160i	Thermo Fisher Scientific, Waltham, MA, USA
Incubator ICP 500	Memmert, Schwabach, Germany
Incubator Kelvitron®	Heraus Holding GmbH, Hanau, Deutschland
MAB PAK HIC Butyl column, 5 µm (4.6 × 100 mm)	Thermo Fisher Scientific, Waltham, MA, USA
MS, Triple Quad™ 5500 system	AB Sciex, Framingham, MA, USA
MS, Triple Quad™ 6500 system	AB Sciex, Framingham, MA, USA
MS, TripleTOF® 6600+	AB Sciex, Framingham, MA, USA
Multichannel pipette BenchSmart96	Mettler-Toledo, Columbus, OH, USA
NanoDSF, Prometheus NT.PLEX	NanoTemper Technologies, Munich, Germany
pH meter Seven Easy	Mettler-Toledo, Columbus, OH, USA
pH meter WTW	Xylem Analytics, Weilheim, Germany
Plate reader, EnVision 2104	Perkin Elmer, Boston, MA, USA
Plate reader, MESO Quickplex SQ120	Meso Scale Discovery, Rockville, MD, USA
Plate reader, Synergy Neo2	BioTek Instruments, Winooski, VT, USA
Plate shaker, Gran Bio™ PHMP-4	Grant Instruments, Cambridge, GB
Plate washer, ELX405	BioTek Instruments, Winooski, VT, USA
Spectrophotometer, NanoDrop™ 1000	Thermo Fisher Scientific, Waltham, MA, USA
Spectrophotometer, NanoDrop™ One ^C	Thermo Fisher Scientific, Waltham, MA, USA
Sterile bench, laminar air flow, HeraSafe®	Thermo Fisher Scientific, Waltham, MA, USA
ThermoMixer® comfort	Eppendorf, Hamburg, Germany
TSKgel® SuperSW3000 column (4.6 × 300 mm)	Tosoh Bioscience, Tokyo, Japan
Tube roller, Roller Mixer SRT1	Stuart, Staffordshire, GB
Tube rotator, IKA® Loopster basic	IKA®-Werke, Staufen, Germany
Ultracentrifuge Sorvall Evolution RC	Thermo Fisher Scientific, Waltham, MA, USA
Ultracentrifuge Sorvall WX Ultra 90	Thermo Fisher Scientific, Waltham, MA, USA

Further comprised common laboratory instrumentation, for example, water bath and pipettes.

6.11. Software

HPLC Software ChemStation	Agilent Technologies, Santa Clara, CA, USA
Genedata BRAIN	Genedata, Basel, Switzerland
PeakView® software + Bio Tool Kit software plug-in	AB Sciex, Framingham, MA, USA
BioPharmaView™ software	AB Sciex, Framingham, MA, USA

Microsoft Office 365	Microsoft, Redmond, WA, USA
Lasergene 17	DNASTAR, Madison, WI, USA
FortéBio Octet Data Analysis ver. 8.2.0.7 and 12.0.1.2	FortéBio, Fremont, CA, USA
FortéBio Octet Data Acquisition ver. 12.0.1.8	FortéBio, Fremont, CA, USA
MSD Discovery Workbench 4.0	Meso Scale Discovery, Rockville, MD, USA
PyMOL ver. 1.8.6.0 and 2.3	Schrodinger, San Diego, CA, USA
Gen5™ microplate reader Software ver. 3.08.01	BioTeK, Winooski, VT, USA
PR.Thermo Control software ver. 2.1.2	NanoTemper Technologies, Munich, Germany
AB Sciex Analyst ver. 1.7 and ver. 1.6.2	AB Sciex, Framingham, MA, USA
Prism ver. 8.0.0	GraphPad Software, La Jolla, CA, USA
Phoenix WinNonlin™ (ver. 6.3)	Certara, Princeton, NJ, USA
Vi-CELL™ XR Cell viability analyzer ver. 2.04	Beckmann Coulter, Brea, CA, USA
OpenLab CDS (ver. 2.4)	Agilent Technologies, Santa Clara, CA, USA
OpenLab CDS Data Analysis (ver. 2.4)	Agilent Technologies, Santa Clara, CA, USA
Watson LIMS™ software (ver. 7.5)	Thermo Fisher Scientific, Waltham, MA, USA
ÄKTA UNICORN software ver. 5.31 (Build 407)	GE Healthcare, Buckinghamshire, GB
EnVision Workstation ver. 1.12	Perkin Elmer, Boston, MA, USA

6.12. Transformation of *E. coli*

Plasmid DNA was amplified in *E. coli* cells after transformation by heat shock. Therefore, plasmid DNA (1 µL or at least 50 ng) was added to 50 µL One Shot TOP10 chemically competent *E. coli* cells that were thawed on ice and incubated on ice for 15-30 min. A water bath at 42°C was used to heat shock the cells for 45 s before they were put again on ice for 2 min. Afterwards, 250 µL prewarmed S.O.C medium was added and transformed cells were incubated for 0.5 h at 37°C, 300 rpm. 50 µL cell suspension was plated onto selective agar plates and incubated overnight at 37°C.

6.13. Plasmid Amplification and Preparation

To amplify plasmids, a single colony of transformed *E. coli* cells (section 6.12) was inoculated in selective 2xTY medium (50-250 mL) overnight at 37°C, 250 rpm. Subsequently, the culture was centrifuged at 4000 × *g* for 15 min and the supernatant was discarded. Plasmid preparation was performed using either the PureLink® HiPure Plasmid Midiprep Kit or the GenElute™ High Performance Plasmid Maxiprep Kit according to the

manufacturer's instructions. Plasmid DNA in Milli-Q® water was stored at 4°C until contemporary transfection or at -20°C for long time storage.

6.14. Quantification of DNA in Aqueous Solutions

The concentration of DNA in aqueous solutions was measured using the NanoDrop™ 1000 UV/VIS spectrophotometer according to the manufacturer's instructions. Therefore, 1.5 µL sample was used to assess the concentration based on the absorbance at 260 nm and the DNA purity by utilizing the ratios of sample absorbance A_{260}/A_{280} and A_{260}/A_{230} . Ratios of ~1.8 should be analyzed for A_{260}/A_{280} and ratios for A_{260}/A_{230} should be in the range of 2.0-2.2. Lower values indicate the presence of contaminants, for example, proteins.

6.15. Expression of Antibodies

For the expression of antibodies, the Expi293F™ Expression System Kit was used according to the manufacturer's instructions. Therefore, Expi293F™ cells were cultured in Expi293F™ Expression Medium in Erlenmeyer flasks at 37°C, 5% CO₂ and 80 rpm. For transfection, the viability and density of the cultured Expi293F™ was determined by using ViCell cell counter (Beckman Coulter). If cells were suitable for transfection (viability should be >95%), 1.25 mL Opti-MEM™ were gently mixed with 80 µL ExpiFectamine™ and incubated at room temperature for maximal 5 min. Next, 25 µg plasmid-DNA, 1:1 mixed HC and LC plasmids of the antibody, was diluted in 1.25 mL Opti-MEM™, added to the previously diluted and incubated ExpiFectamine™, and incubated for 20 min at room temperature. Meanwhile, Expi293F™ cells were diluted in Expi293F™ Expression Medium in a new Erlenmeyer flask to 2.9×10^6 viable cells/mL (21 mL). Then, the DNA-ExpiFectamine™-mixture was added to the cells. After ~18 h of incubation at 37°C, 5% CO₂, and 80 rpm, 150 µL Enhancer 1 and 1.5 mL Enhancer 2 were added and the cell culture was incubated for another 6 days. Afterwards, antibodies were harvested. Therefore, the cell culture was centrifuged (4000 × *g*, 5 min) and the supernatant was sterilized using 0.22 µm Steritop filters. Antibodies were purified by protein A chromatography (section 6.18). The transfection volume (here: 25 mL) can be scaled-up by keeping the ratios of reagents equal.

6.16. Quantification of Protein in Aqueous Solutions

The quantification of protein in aqueous solutions was done by measuring the absorbance of aromatic acids at 280 nm using the spectrophotometer NanoDrop™ 1000 or NanoDrop™ ONE (Thermo Fisher Scientific)

according to the manufacturer's instructions. For this, 2.0 μ L sample was used. Furthermore, the molecular weight (MW in kilo Dalton) and the extinction coefficient ($M^{-1}cm^{-1}$) of the corresponding protein was obtained from BRAIN (Genedata) and used for calculation of the protein concentration in mg/mL. For the concentration determination of commercially available full-length IgG molecules of which no specific MW and extinctions coefficient could be calculated, the IgG sample type was used (mass extinction coefficient of 13.7 at 280 nm for a 1% (10 mg/mL) IgG solution).

6.17. Generation of ADCs with Different Conjugation Methods

Different conjugation methods were used to generate ADCs. These methods are described in detail in the sections 6.17.1-6.17.5. Amount of reagent given in equivalents refers to molar equivalents compared to the antibody. After the conjugation reaction, all products were purified and buffer exchanged to PBS pH 7.4 or PBS pH 7.0 (section 6.8) by preparative size exclusion chromatography (SEC, section 6.19) before they were concentrated using Amicon® Ultra Centrifugal filter with a MWCO of 100 kDa. Finally, the ADC product was sterile filtered using 0.2 μ m Ultrafree-CL centrifugal devices and the purity was analyzed by SE-HPLC (section 6.20) while DAR was determined by LC-MS (section 6.22).

6.17.1. Conjugation to Interchain Cysteines

Interchain cysteine linked ADCs were generated by partial reduction of the four interchain disulfide bonds of an antibody. Therefore, the antibody was diluted to a final concentration of 5 mg/mL in cysteine conjugation buffer (section 6.8) and reduced for 2 h at 37°C with 2.1 equivalents of TCEP. Subsequently, the reduced antibody was incubated with 8 equivalents of linker-payload (MC-VC-PAB-MMAE) for 1 h at 25°C. The reaction was quenched for 30 min at 25°C after addition of 25 equivalents of N-acetylcysteine.

6.17.2. Conjugation to Engineered Cysteines

Conjugation of linker-payloads to specific cysteines that were incorporated into the antibody sequence by genetic engineering required a reduction-reoxidation step. Therefore, antibodies were diluted to 5 mg/mL in cysteine conjugation buffer (section 6.8) and incubated for 2 h at 37°C with 40 equivalents of TCEP. For the following reoxidation step, TCEP was first removed, and the reduced antibody was formulated in PBS (section 6.8) using an ÄKTA Pure equipped with a 5 mL HiTrap™ desalting column. Then, 20 equivalents of L-dehydroascorbic acid were added and incubated for 2 h at 25°C. Conjugation was done by the addition of

8 equivalents linker-payload (MC-VC-PAB-MMAE) and incubation for 20 h at 35°C. Finally, 25 equivalents of N-acetylcysteine were added, and the mixture was incubated for 30 min at 25°C to quench the reaction.

6.17.3. Conjugation via Microbial Transglutaminase

For conjugation to engineered mTG tags, 5 mg/mL antibody formulated in mTG conjugation buffer (section 3.8) was mixed with 6 units/mL mTG from *S. mobaraensis* and 10 equivalents of linker-payload (G₃-VC-PAB-MMAE or G₃-VC-PAB-MMAF) and incubated at 37°C. The reaction mixture should contain 10% DMSO. After 16 h the reaction was chilled on ice and purified as stated above.

6.17.4. Site-Specific Conjugation to Native mAbs

Site-specific conjugation to native trastuzumab was done by using an engineered mTG.¹⁶⁸ Therefore, 5 mg/mL antibody was mixed with 75 units/mL of genetically engineered mTG¹⁶⁸ and 20 equivalents of G₃-VC-PAB-MMAE in mTG conjugation buffer (section 6.8) supplemented with 10% DMSO. After incubation for 16 h at 37°C the reaction was chilled on ice and purified as stated above.

6.17.5. Conjugation via Sortase A

For the conjugation to the engineered Sortase A (SrtA) recognition motif at the C-terminus of trastuzumab LCs, 5 mg/mL of antibody formulated in StrA conjugation buffer (section 6.8) was mixed with 5 mM CaCl₂, 20 equivalents of linker-payload (G₃-MMAF), and 13 μM SrtA and incubated for 100 min at 25°C. Afterwards, the reaction was stopped by the addition of 10 mM EDTA.

6.18. Protein A Chromatography

Expressed antibodies were purified from sterile filtered cell culture supernatant using protein A chromatography. The chromatography was performed on an ÄKTExpress equipped with a HiTrap™ 5 mL MabSelect™ SuRe™ column and a HiPrep™ 26/10 desalting column. First both columns were equilibrated with PBS pH 7.4. Therefore, a 5-fold column volume (CV) at 2.5 mL/min were used for the MabSelect™ column and 3 CV at 7.5 mL/min for the desalting column. After equilibration, the cell supernatant was loaded (2.5 mL/min) onto the MabSelect™ column where antibodies bound to protein A. Subsequently, the column was washed with ~5 CV PBS pH 7.4 until stable baseline, followed by elution of the bound antibodies at pH 3.0 by 3 CV 50 mM acetic acid. The eluate was directly loaded (7.5 mL/min) onto the desalting column with PBS pH 7.4 to remove the acetic acid. Elution from this column was done with 1.5 CV PBS pH 7.4. The eluate was

collected in fractions (1 mL) and fractions containing protein (A_{280} signal) were pooled. Then, the purity of the antibody solution was assessed by SE-HPLC (section 6.20) and the antibody solution was concentrated using an Amicon® Ultra centrifugal filter device (MWCO 50 kDa). Antibody solutions with an aggregate content >5%, as determined by SE-HPLC, were further purified by preparative SEC (section 6.19) and subsequently concentrated again. Finally, the antibody solution was sterile filtered using a Millex®-GV 0.22 μ m syringe filter and the protein concentration was determined by UV/VIS spectroscopy at 280 nm (section 6.16).

6.19. Preparative Size Exclusion Chromatography (SEC)

To remove undesired low and high molecular weight species, antibodies and generated ADCs were purified and buffer exchanged by preparative SEC. Therefore, an ÄKTA Avant or ÄKTA Pure system equipped with a HiLoad™ Superdex 200 pg column (26 \times 600 mm or 16 \times 600 mm, GE Healthcare) was used at room temperature with a flowrate of 1-2.5 mL/min and PBS pH 7.4 as mobile phase. The column was equilibrated with 1.5-5 CV mobile phase before protein solution was loaded onto the column via sample loop. Fractions of 1-2 mL were collected and fractions containing non-aggregated target protein were pooled.

6.20. Analytical Size Exclusion Chromatography (SE-HPLC)

SE-HPLC was used to analyze the protein purity and molecular size of produced antibodies and ADCs. For this, an Agilent 1260 Infinity system equipped with a TSKgel® SuperSW3000 column (4.6 \times 300 mm, Tosoh Bioscience) was used at 0.35 mL/min with SE-HPLC mobile phase buffer (section 6.8) at room temperature. The column was equilibrated until a stable baseline was observed. Typically, 10 μ g of protein were injected and analyzed for 15 min. Signals were recorded at 214 nm and 280 nm. Additionally, a gel filtration standard (GFS) containing a mixture of five molecular weight markers (Bio-Rad) was injected to allow for calculation of the apparent molecular weights. The following injection sequence was usually used: mobile phase, GFS, samples (up to 10), GFS, mobile phase. Peaks were analyzed and integrated using the ChemStation software and peak areas were used to determine the content of the pure target protein and the high and low molecular weight species.

6.21. Analytical Hydrophobic Interaction Chromatography

Hydrophobic interaction chromatography (HIC) was used to determine the apparent hydrophobicity of molecules. For this, samples were diluted to 0.5 mg/mL in PBS pH 7.4 or PBS pH 7.0 supplemented with 0.5 M

(NH₄)₂SO₄. Furthermore, an Agilent 1260 Infinity system equipped with a MAB PAK HIC Butyl column (5 μm, 4.6 × 100 mm, Thermo Fisher Scientific) was used. After equilibration of the column until a stable baseline was observed, 40 μg of sample was injected and a linear gradient from 100% HIC mobile phase A to 100% HIC mobile phase B (section 6.8) over 20 min at 1 mL/min and 30°C was applied. Signals were recorded at 280 nm. Peaks were analyzed and integrated using the ChemStation software and peak areas and retention times were recorded. Finally, two different calculations were performed with the data:

To investigate the influence of the conjugation on the apparent hydrophobicity, the retention time of the ADC DAR2 species was divided by the retention time of the respective parental mAb to calculate the relative retention time (rRT).

In addition, a different calculation was used to compare the apparent hydrophobicity of molecules measured in different runs and to directly compare the hydrophobicity of different ADCs. For this, a HIC standard that was analyzed in every run was used (**Figure 11, a**). The HIC standard (produced in-house) contained a mAb and ADCs with different DAR species. Five of the peaks which correspond to the DAR species 0 to 4 and their retention times (RT) were used to perform a linear regression. Therefore, the peak of the DAR 4 species was assigned a relative retention factor of 1, the peak of DAR 0 a relative retention factor of 0 and the other three peaks were assigned intermediate relative retention factors, accordingly (**Figure 11, b**). The linear regression was used to calculate the relative retention factors, from here on called normalized retention times (nRT), of the measured samples (**Figure 11, c**). In the exemplary formula in **Figure 11, c** the variable y corresponds to nRT of the sample whereas the x-value corresponds to the measured RT of sample. The RT of the peak with the largest area (main product peak) was used as RT of the sample. In this study, this corresponds to the DAR 2 species of trastuzumab-, secukinumab-, and briakinumab-ADCs.

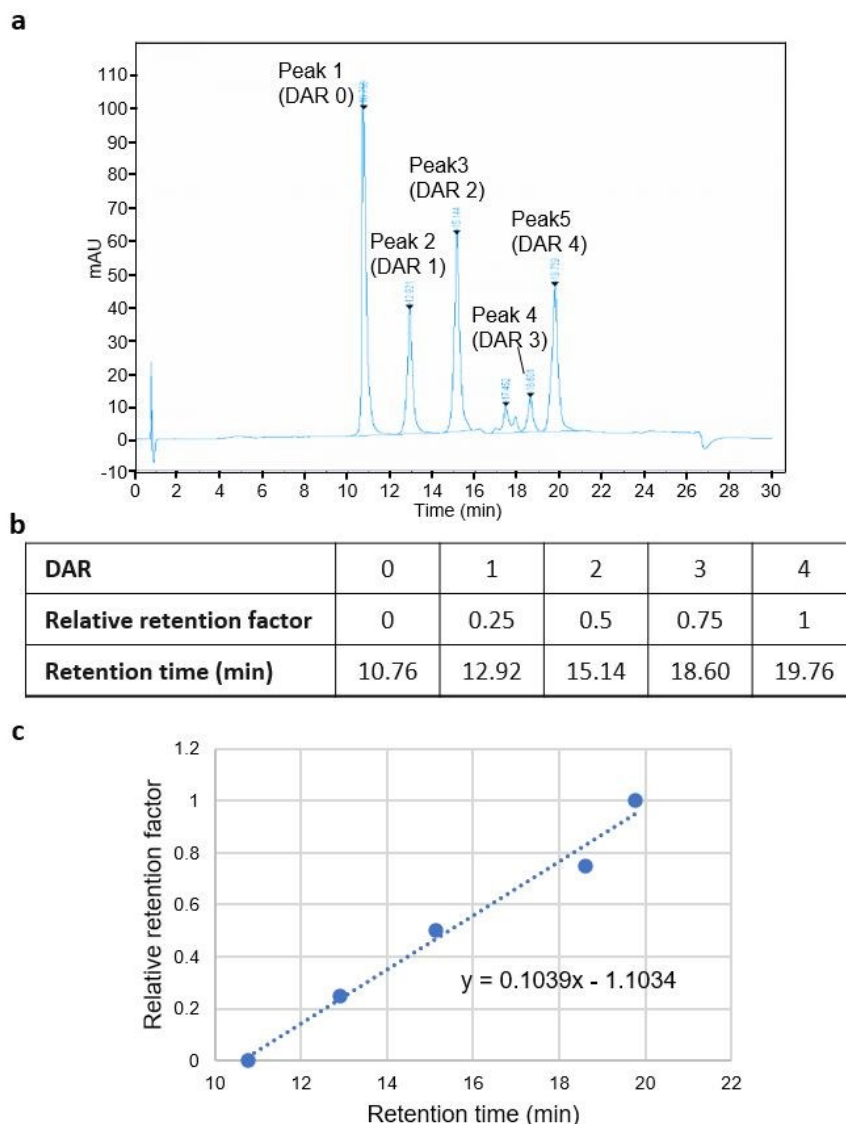


Figure 11. Usage of a standard, containing ADCs with different DARs, to calculate normalized retention times (nRTs) of sample ADCs. a) Example HIC chromatogram of the standard. The peaks 1 to 5 correspond to the DAR species 0 to 4 and each DAR species is assigned a relative retention factor (**b**). **c)** The corresponding retention times of the peaks were plotted against their relative retention factors. The formula of the linear regression can be used to calculate the relative retention factor (named normalized retention time, y) of a sample with known retention time (x), analyzed in the same run.

6.22. DAR Determination by Liquid Chromatography-Mass Spectroscopy

For LC-MS analysis, ADCs or mAbs were diluted in 0.1% formic acid to a final concentration of 0.05 mg/mL. Then, 12 mM (final) TCEP was added and incubated for 3 min at room temperature to reduce the sample. 0.2 μ g of the reduced sample was injected into a Exion liquid chromatography™ system equipped with a RP-column (bioZen™ 3.6 μ m Intact C4 column) for purification, before entering the TripleTOF 6600+ (AB Sciex) with a flowrate of 0.1 mL/min in MS mobile phase (section 6.8). For the electrospray ionization mass

spectroscopy (ESI-MS) a positive ion mode and a data acquisition range of 400-4000 Da were used. The data was further analysed using AB Sciex software (Peak Viewer, BioToolKit or BioPharmaView). Deconvoluted spectrums were used to identify the LC and HC fragments by comparing observed masses with calculated masses considering different numbers of attached drug, fragmentations, and glycosylation patterns. The peak areas of the identified fragments were used to calculate the DAR.

6.23. *In vitro* Serum Stability Analyzed by Liquid Chromatography-Mass Spectroscopy and Enzyme-Linked Immunosorbent Assay

To maintain a stable and defined pH close to physiological pH, mouse serum was adjusted to a pH ranging between 7.30 and 7.40 by the addition of finally 0.3 M HEPES using 2.0 M HEPES buffer pH 7.55. Buffered serum was sterile filtered using 0.22 µm Millex-GV syringe filter or Steriflip™ devices. ADCs were diluted in serum to 50 µg/mL for analysis by LC-MS/MS or to 500 µg/mL for ELISA measurements, gently mixed, transferred into PCR tubes as aliquots of 20 µL, and incubated at 37°C, 5% CO₂. After 0, 2, 4, 6, 24, 48, 72, and 96 h of incubation two samples were taken at each timepoint and stored at -80°C until analyses.

To quantify released free payload LC-MS/MS analysis was used. Therefore, 5 µL of each serum sample was transferred into a new PCR-tube, supplemented with internal standard, extracted with 150 µL methanol, and analyzed by UPLC-MS/MS. An ACQUITY UPLC H-Class System equipped with an Acquity UPLC BEH® C18 column (1.7 µm, 2.1 × 50 mm, Waters) was used with the mobile phases 0.1% formic acid in water and ACN. MS measurements were done using an AB Sciex 6500 Triple Quad™ system and data was analyzed using AB Sciex Analyst 1.7 software (AB Sciex).

Quantification of the antibody-conjugated payload was done by ELISA. Therefore, Nunc MaxiSorp™ 96-well plates were coated overnight at 4°C with 2 µg/mL anti-human Fc mAb (#115-035-062, Jackson ImmunoResearch Laboratories) or unrelated antigen (non-specific binding control). In case of trastuzumab-ADCs plates were coated with 2 µg/mL HER2 instead of anti-human Fc mAb. All incubation steps were done at room temperature for 1 h. In between, plates were washed three times with PBS-T1 (section 6.8). Furthermore, volumes of 300 µL/well were used for the washing steps (plate washer) and blocking step and 100 µL/well for all further incubation steps. All dilutions were done in The Blocking Solution (CANDOR Bioscience).

After coating, the plates were blocked with The Blocking Solution, followed by incubation with diluted standards at defined concentrations and serum samples. Analyses were performed in triplicates. For detection, first an incubation with mouse anti-MMAE mAb (1:500, Clone #2E2, Epitope Diagnostics), followed by incubation with secondary horseradish peroxidase-conjugated goat anti-mouse IgG (1:500, #115-035-072,

Jackson ImmunoResearch Laboratories) and finally with 1-Step™ Ultra TMB-ELISA Substrate Solution was done. The reaction was stopped by the addition of 1 M sulfuric acid as soon as an appropriate staining intensity was observed. The absorption was analyzed at 450 nm with a plate reader (Synergy Neo2). For data analysis, a standard curve was generated with the results of the different standard dilutions and their known concentrations, fitted with a four-parameter fit and used to calculate the concentrations of antibody-conjugated payload in the sample.

Finally, values of percent intact, remaining ADC were calculated with the results obtained by both analytical methods. Therefore, the starting payload concentration of the ADC (free payload determination by LC-MS/MS) or the concentration of antibody-conjugated payload in the 0 h sample (antibody-conjugated payload determination by ELISA) was set to be 100% remaining ADC.

6.24. Pharmacokinetic Studies in huFcRn Mice

PK studies were conducted in hemizygous Tg276 mice. A single dose of 2, 3, or 5 mg/kg of mAb or ADC was administered intravenously into the tail vein of 6-19-week-old mice. A sparse sampling approach was used to collect blood samples from 2-3 mice per time point and up to 540 h post dosing in pre-chilled (0-4°C) lithium heparin tubes. The blood samples were centrifuged at 2500 × *g* for 10 min at 4°C. Then, the plasma was transferred into new vials and immediately stored at -80°C until analyses. All PK studies, animal handling and experimentation, were conducted in accordance with the Italian D.Lvo. 2014/26 and Directive 2010/63/EU. The studies were performed at the Istituto di Ricerche Biomediche *Antoine Marxer*, Colleretto Giacosa, Italy. The institute is fully authorized by the Italian Ministry of Health to conduct safety studies.

6.25. Total Antibody Ligand Binding Assay for the Analyses of Pharmacokinetic Samples

The total antibody concentration in plasma samples was determined by a highly sensitive electrochemiluminescence ligand binding assay (LBA) based on the Meso Scale Discovery technology (Meso Scale Diagnostics). All incubation steps were performed at 22°C with orbital shaking at 450 rpm and a volume of 50 µL/well. Between the incubations, plates were washed three times with 200 µL/well PBS-T2 (section 6.8) using a plate washer. First, MSD GOLD™ 96-well Streptavidin QUICKPLEX® plates were coated for 2 h with 2.5 µg/mL biotin-SP-conjugated AffiniPure goat anti-human IgG, Fcγ fragment specific (#109-065-098, Jackson ImmunoResearch). Meanwhile, plasma samples, standards, and quality controls were serially diluted in dilution buffer (section 6.8). Then, the dilutions were added in duplicates to the plates and incubated for 1 h. For detection, the plates were incubated for 1 h with 0.6 µg/mL mouse anti-human IgG, F(ab')₂ fragment specific (#209-005-097, Jackson ImmunoResearch), previously labeled with MSD GOLD SULFO-TAG (#R91AO,

Meso Scale Diagnostics) according to the manufacturer's instructions and diluted in dilution buffer. Finally, 2x MSD Read Buffer T with surfactant (section 6.8) was added (150 μ L/well) and plates were read on a MESO Quickplex SQ120 plate reader. Data was analyzed using the Watson LIMS™ software (version 7.5, Thermo Fisher Scientific). The standard curve, generated with standards with known concentrations, was fitted with a 5PL (Marquart) equation, weighting factor $1/Y^2$, and used to calculate the total mAb concentration of the plasma samples. The lower limit of quantification (LLOQ) was 50 ng/mL.

6.26. Antibody-Conjugated Payload Assay for the Analyses of Pharmacokinetic Samples

To analyze the *in vivo* stability of ADCs, the antibody-conjugated payload concentrations in plasma samples were measured by a hybrid affinity capture LC-MS/MS method. First, ADCs were captured by binding to protein A. Therefore, Protein A Immunocapture Spin Plates were washed two times with PBS pH 7.4 (200 μ L) by centrifugation at 1000 rpm for 2 min. PK plasma samples as well as ADC standards and quality controls, which were prepared in mouse plasma, were separately diluted in PBS pH 7.4. Subsequently, 95 μ L of the dilutions were transferred to the plates and incubated for 20 min at 22°C and 300 rpm. Then, plates were washed two times like before. Since the payload was conjugated to the ADCs via cleavable VC-PAB linker moiety an enzymatically release of MMAE was performed. Therefore, 200 μ L of 1 M acetate buffer pH 5.0 were mixed with 30 μ L cleavage buffer (section 6.8), added to each well, and incubated for 1.5 h at 40°C and 850 rpm. During this incubation step plates were covered with a sealing foil. Then, 10 μ L 0.5 μ g/mL d8-MMAE (internal standard) was added to each well and incubated for 10 min at room temperature and 850 rpm. The released MMAE was eluted by centrifugation (5 min, 1000 rpm) and mixed for 10 min at 37°C and 350 rpm. Afterwards, 200 μ L of eluent was precipitated with 600 μ L precipitation reagent (section 6.8) and centrifugated (10 min, 3000 rpm). The supernatant was acidified with 2.5% formic acid (1:1) and analyzed by LC-MS/MS using a Waters Acquity UPLC® system equipped with an Acquity UPLC BEH® C18 column (2.1 x 100 mm, 1.7 μ m, Waters) for chromatographic separation and an AB SCIEX™ Triple Quad™ 5500 MS with a turbo ion spray source (positive ion mode). The resulting data was analyzed with the AB SCIEX Analyst software (version 1.6.2) and a standard curve was fitted using a linear equation, weighting $1/x^2$. The LLOQ was 10 ng/mL.

6.27. Analysis of Pharmacokinetic Parameters

Mean plasma concentration-time profiles of total antibody and antibody-conjugated payload were used for parameter estimation. For both the PK parameters area-under-the-curve (AUC_{0-inf}), clearance (CL), and the maximum observed plasma concentration (C_{max}) were estimated by non-compartmental analysis using

Phoenix WinNonlin® (version 6.3, Certara). The concentration of all PK samples that were calculated below the quantification limit (BQL) were considered as 0 ng/mL.

6.28. Nano Differential Scanning Fluorimetry

Nano differential scanning fluorimetry (nanoDSF) can be used to analyze thermal unfolding of proteins by detecting the intrinsic fluorescence of tyrosine (330 nm) and tryptophan (350 nm). Therefore, a nanoDSF standard capillary chip was loaded with 5 mg/mL ADC or mAb and placed into a Prometheus NT.PLEX device. The temperature was gradually increased from 20°C to 95°C at 1°C/min while the fluorescence at 330 and 350 nm was recorded. The first derivative of the F350 nm/F330 nm ratio was used to determine the unfolding transition midpoints (T_m).

6.29. huFcRn Affinity Chromatography

Differences in the interaction with huFcRn of mAbs and ADCs was analyzed by huFcRn affinity chromatography as previously described.¹³² A GE Tricorn column (#28-4064-09, GE) packed with huFcRn-Biotin-Streptavidin-Sepharose resin (huFcRn column; 4.6 × 50 mm, CV 1 mL) was kindly provided by the laboratory of Dirk Müller-Pompalla, Merck KGaA. The column chromatography was performed using an Agilent 1260 Infinity II HPLC system at 0.5 mL/min and at room temperature. ADC or mAb was diluted to 1 mg/mL in FcRn mobile phase A (section 6.8) and stored in the autosampler at 10°C until analysis. After equilibration of the huFcRn column with ~10 CV 80% FcRn mobile phase A and 20% FcRn mobile Phase B (section 6.8), 50 µL sample was injected and further analyzed for 104 min at 280 nm. A linear pH gradient from pH 5.5 to pH 8.8 was applied for elution (see **Table 2**). Every experiment was started with the injection and analysis of FcRn mobile Phase A (blank), followed by the injection and analysis of the reference mAb trastuzumab. After nine additional mAb/ADC sample injections this injection sequence of the beginning (mobile phase A, followed by trastuzumab) was repeated. Furthermore, after every fifth mAb/ADC sample injection an additional column washing step was integrated to remove any remaining sample from the column (see **Table 3**).



Table 2. Linear pH gradient used for the huFcRn affinity chromatography.

Time (min)	% FcRn mobile Phase A	% FcRn mobile Phase B
0	80	20
10	80	20
80	0	100
90	0	100
93	80	20
103	80	20

Table 3. pH gradient used to wash and re-equilibrate the huFcRn column after every fifth mAb/ADC sample analysis.

Time (min)	% FcRn mobile Phase A	% FcRn mobile Phase B
0	0	100
13	0	100
15	80	20
90	80	20

Data was processed using OpenLab CDS Data Analysis (version 2.4, Agilent Technologies). The calculated peak width at half peak height (PW) and retention time (RT) of a mAb/ADC sample was further normalized to maintain the relative PW (rPW) and the relative RT (rRT) of the sample. Therefore, the corresponding results of the reference mAb, trastuzumab, analyzed before the sample, were subtracted from the results of the mAb/ADC sample.

6.30. Bio-Layer Interferometry

Kinetic binding parameters were determined by Bio-Layer Interferometry (BLI) using the Octet RED96 or Octet RED system (FortéBio) with 1000 rpm orbital agitation speed and 200 μ L volume in black 96-well plates. Biosensors were equilibrated in DPBS for 10-30 min before the measurement was started. Data was analyzed using Analysis Software (version 8.2.0.7 and 12.0.1.2 FortéBio).

6.30.1. huFcRn Binding Kinetics

The BLI experiment to analyze the interaction of ADCs and mAbs with FcRn was adapted from a published FortéBio application note.¹⁶⁹ Recombinant huFcRn was buffer exchanged into FcRn binding assay buffer (pH 6.0, section 3.8) by using Zeba Spin desalting columns according to the manufacturer's instruction. The binding kinetics were determined at 30°C using Fab2G biosensors. First the optimized loading concentrations for every ADC or mAb were determined. Therefore, ADC/mAb was diluted in DPBS pH 7.4 to different concentrations (1, 3, 5, and 7 µg/mL) and loaded to the biosensors for 240 s. A baseline was adjusted for 60 s with FcRn binding assay buffer. Then, association was measured by transferring the biosensors for 60 s into 1.6 µM huFcRn, followed by dissociation in FcRn binding assay buffer for 180 s. The lowest concentration of mAb/ADC that yielded a signal response in the range of 0.4 nm to 0.6 nm in the association step was used as optimized loading concentration.¹⁶⁹

The FcRn binding kinetic measurement was performed in a similar way. Biosensors were loaded with the optimized concentration of ADC or mAb in DPBS pH 7.4 for 240 s and further incubated for 60 s in FcRn binding assay buffer. Subsequently, association was measured for 60 s at varying concentrations of huFcRn (0.05-1.6 µM) and dissociation for 180 s in FcRn binding assay buffer. Furthermore, several reference measurements were performed. Possible dissociation of immobilized sample molecule was monitored with a loaded biosensor, where the association step was performed in buffer without huFcRn (reference measurement). One additional biosensor was used to monitor whether huFcRn binds to the sample molecule at pH 7.4. Therefore, all assay steps including the association to 1.6 µM huFcRn were performed in DPBS pH 7.4. To analyze non-specific binding of huFcRn to the biosensors, the assay was repeated with reference biosensors where the loading step was omitted (reference sensor measurement). The data was double referenced by subtraction of the reference and reference sensor measurement. After performing a Savitzky-Golay filtering, the data was fitted using a global fitting with a 1:1 Langmuir binding mode and only the first 5 s of dissociation were used to cover the initial fast dissociation of the biphasic dissociation behavior.¹⁶⁹ Furthermore, the whole experiment was repeated to monitor the dissociation behavior at pH 7.4. Therefore, only the dissociation step was varied and performed at pH 7.4. However, in this case data could be only assessed visually as no adequate fitting was possible due to the rapid dissociation.

6.30.2. Clone Self-Interaction Bio-Layer Interferometry

Clone self-Interaction Bio-Layer Interferometry (CSI-BLI) measurements were conducted to analyze the tendency of mAbs and ADCs to self-interact. The experiment was performed at 25°C with AHC biosensors. DPBS was used as assay and sample molecule dilution buffer. Two biosensors were loaded with 10 µg/mL

ADC or mAb for 300 s. Afterwards sensors were exposed to assay buffer for 150 s. The subsequent association step was done for 600 s. Therefore, one of the biosensors was incubated with the same ADC or mAb used for loading of the biosensor but at a concentration of 150 µg/mL (sample measurement). In parallel, the second biosensor was incubated in assay buffer (reference measurement). Finally, the dissociation of both sensors in assay buffer was monitored for 150 s to recognize possible fast dissociation. Binding curves were aligned to the baseline, filtered by Savitzky-Golay filtering, and the response of the association step was calculated. The resulting response of the reference measurement was subtracted from the response of the sample measurement to obtain a normalized response. To allow for assay-to-assay comparability, final assay scores were calculated by subtraction of the normalized response of a reference IgG (trastuzumab), analyzed on the same plate.

6.30.3. Polyspecificity Reagent Bio-Layer Interferometry

In this study polyspecificity reagent (PSR), consisting of the soluble membrane fractions of CHO and HEK293 cells, was used to detect non-specific binding of ADCs and mAbs.

First, PSR was produced according to Xu *et. al.*¹³⁴ The PSR from the two different cell lines was produced separately. Briefly, 100 million soluble ExpiCHO-S™ and HEK293-6E cells from cell culture were transferred to 50 ml conical tubes and pelleted at 550 × *g* for 6 min. From here on all steps were performed on ice or at 4°C and with pre-chilled buffer. The supernatant was discarded and cells were washed two times with 50 mL DPBS (550 × *g* for 6 min). Afterwards, the pellet was resuspended in PSR buffer A (section 6.8) with three times the volume of the pellet and homogenized with a sonicator (four times for 30 s with 30 s pause in between and amplitude of 35%). Homogenized cells were centrifuged at 23,200 rpm for 1 h. The supernatant was discarded, and the pellet surface was washed with 1 mL PSR buffer A before it was resuspended in ~3 mL PSR buffer A and transferred into a Dounce homogenizer to homogenize it 40-times. The protein concentration of the resulting suspension was determined by Pierce™ BCA protein assay according to the manufacturer's instruction. Afterwards, the protein suspension was diluted with PSR buffer B (section 6.8) to 1 mg/mL and incubated over night at 4°C on a tube roller. On the next day, the suspension was centrifuged at 23,200 rpm for 1 h. The protein concentration of the supernatant containing the soluble membrane proteins was analyzed by Pierce™ BCA protein assay, aliquoted, and stored at -20°C. Final PSR is a 1:1 mixture of the soluble membrane proteins of CHO and of HEK293 cells and was prepared freshly for BLI measurements.

The BLI measurement with PSR was performed at 25°C with AHC biosensors and DPBS as dilution buffer. 10 µg/mL ADC or mAb was loaded for 300 s on two biosensors. Subsequently, sensors were blocked with BLI blocking buffer (section 6.8) for 200 s. A baseline was established by rinsing in DPBS for 60 s and the

association was performed for 100 s with 20 µg/mL PSR for one of the biosensors and with DPBS for the other one (reference measurement). Finally, the dissociation was done in DPBS for 60 s. On every plate a second reference measurement was conducted with two biosensors (reference biosensors) to analyze non-specific binding of PSR to the blocked biosensors. Therefore, the loading step of both biosensors was done in DPBS. Binding curves were aligned to the baseline and the response of the association step was calculated. Then, the binding response from the association step of the sample molecule was normalized to the reference measurement by subtraction. To calculate the final PSR-BLI assay score, the normalized response of the reference biosensors was subtracted from the normalized response of the sample molecule.

6.31. Bis-ANS Assay

Bis-ANS (4,4'-Dianilino-1,1'-binaphthyl-5,5'-disulfonate) is an extrinsic fluorescent dye that binds to proteins by hydrophobic interactions. Upon binding the fluorescence of bis-ANS increases.¹⁷⁰ Therefore, it can be used to analyze the hydrophobicity of proteins. The assay was performed at room temperature and bis-ANS was protected from light. First, a stock solution of bis-ANS (8 mM in Milli-Q® water) was diluted in DPBS to 160 µM. Then, the samples, ADC or mAb, were diluted in a black 96-well plate to a concentration of 0.8 mg/mL (50 µL) with DPBS. 50 µL of 160 µM bis-ANS was added to the diluted sample, mixed carefully by pipetting, and incubated for 30 min at 250 rpm. Finally, the sample was excited at 385 nm and the emission spectrum from 400 to 650 nm (1 nm step) was recorded using a Synergy Neo2 reader (BioTek Instruments). For a simple comparison, the relative fluorescence intensity (RFI) measured at 511 nm was used. The final bis-ANS assay score was calculated by subtraction the RFI at 511 nm of a DPBS control, incubated without sample, from the RFI at 511 nm of the sample.

6.32. Affinity-Capture Self-Interaction Nanoparticle Spectroscopy

An additional assay with a different setup compared to CSI-BLI (section 6.30.2) was used to analyze the self-interaction tendencies of ADCs and mAbs. The procedure was done as preciously described.¹³⁷ Therefore, a capture antibody, goat anti-human IgG Fc (#109-005-098, Jackson ImmunoResearch Laboratories), and a non-capture antibody, polyclonal goat antibody (#005-000-003, Jackson ImmunoResearch Laboratories), were buffer exchanged to 20 mM acetate buffer pH 4.3 (section 6.8) using Zeba™ Spin desalting columns according to the manufacturer's instruction. After determining the protein concentration (section 6.16) it was adjusted to 0.4 mg/mL using 20 mM acetate buffer pH 4.3. Then, an antibody-mixture of 80% capture and 20% non-capture antibody was prepared. One volume of the antibody-mixture was incubated with nine volumes gold nanoparticles for 1 h on a rotator (30 rpm) at room temperature. Afterwards, the coated

nanoparticles were blocked with 0.1 μM PEG thiol for 1 h under the same conditions. The coated and blocked particles were buffer exchanged and concentrated 10-times. Therefore, the particle solution was passed through a 0.22 μM PVDF Millex-GV Syringe Filter Unit. The particles retained on the top of the membrane and were eluted with DPBS using one-tenth of the volume of the antibody/particle mixture that was passed through the filter. To measure self-interaction, 10 μL of the prepared particle solution were mixed with 100 μL 50 $\mu\text{g}/\text{mL}$ mAb/ADC (previously diluted in DPBS) or DPBS buffer control in a 96-well polypropylene plate (#5043-9311, Agilent Technologies). After incubation for 2 h at room temperature on a shaker at 250 rpm, 100 μL were transferred to a 365-well polystyrene UV plate (#12-565-506, Fisher Scientific). The plate was briefly centrifuged (\sim up to 700 rpm) to get the menisci at same level. Afterwards, a plate reader (Synergy Neo2, BioTek Instruments) was used to measure the absorbance from 450 to 650 nm at an increment of 2 nm. For data processing Microsoft Excel was used to identify the wavelength of maximum absorbance. Twenty data points around this wavelength were used to smooth the data and stored in an array. Each data point was averaged with the data point directly before and after it. A LINEST function was used to fit the data with a second-order polynomial and the coefficients were used to calculate the wavelength where the slope is equal to zero (wavelength of maximum absorbance). The calculated wavelength of maximum absorbance of the DPBS buffer control was subtracted from the calculated wavelength of maximum absorbance of the ADC or mAb to receive the final AC-SINS score.

6.33. Baculovirus Particle Enzyme-Linked Immunosorbent Assay

In this study, the original baculovirus particle (BVP) ELISA developed by Hötzel *et al.*¹²¹ was adapted for the use with ADCs. Therefore, Nunc MaxiSorp™ 96-well plates were coated overnight at 4°C with BV particles diluted in BVP coating buffer (section 6.8) to 20 $\mu\text{g}/\text{mL}$ (100 $\mu\text{L}/\text{well}$). All further incubation steps were done at room temperature for 1 h. Assay buffer for all dilutions and blocking was BVP/Heparin ELISA buffer (section 6.8), while DPBS was used for washing. Plates were washed four times between incubation steps with 300 $\mu\text{L}/\text{well}$ using a plate washer. After coating, plates were blocked (300 $\mu\text{L}/\text{well}$). Meanwhile, ADC samples were 1:3 serially diluted with an initial concentration of 20 $\mu\text{g}/\text{mL}$. The final, sixth dilution step was done 1:27. Then, the seven different sample dilutions and one buffer sample were added to the plates in quadruplicates (100 $\mu\text{L}/\text{well}$). Subsequently, horseradish peroxidase-conjugated goat anti-human IgG (#109-036-098, ImmunoResearch Laboratories) was added (160 ng/mL, 100 $\mu\text{L}/\text{well}$) and incubated. Finally, 100 $\mu\text{L}/\text{well}$ 1-Step™ Ultra TMB-ELISA Substrate Solution was added to initiate the colorimetric reaction and stopped after 11 min by the addition of 100 $\mu\text{L}/\text{well}$ 1 M sulfuric acid. The absorbance at 450 nm was recorded using a plate reader (Envision 2104, Perkin Elmer). For data analysis, the mean values of the

measured quadruplicates were calculated. Then, these results were normalized by dividing the mean values of each ADC concentration by the mean value of the buffer control without sample. Afterwards, the mean of the normalized results of the different sample concentrations (20-0.003 µg/mL) was calculated (normalized score). The final BVP score was calculated by subtracting the corresponding normalized score of the positive control (trastuzumab conjugated C-terminally at HC mTG tags to G₃-VC-PAB-MMAF, T-HC-MMAF), which was analyzed in the same experiment.

6.34. Heparin Enzyme-Linked Immunosorbent Assay

To analyze non-specific binding to heparin, heparin was diluted in DPBS to 20 µg/mL and applied (100 µL/well) to Nunc MaxiSorp™ 96-well plates. After incubation overnight at 4°C, plates were washed four times with DPBS (300 µL/well) using a plate washer. For further dilutions or blocking BVP/Heparin ELISA buffer (section 6.8) was used and all incubations were done at room temperature. The coated and washed plates were blocked with 300 µL/well for 1 h. Meanwhile, ADCs were diluted to an initial concentration of 20 µg/mL and further subjected to a serial 1:3 dilution for a total of 6 dilution steps. After blocking, plates were washed again and the seven different ADC dilutions (20.00-0.03 µg/mL) and an assay buffer control without ADC were transferred to the plates in triplicates and incubated for 2 h. Then, plates were washed and horseradish peroxidase-conjugated goat anti-human IgG (#109-036-098, Jackson ImmunoResearch Laboratories) was added at 160 ng/mL (100 µL/well) and incubated for 1 h. After a final washing step, plates were incubated with 100 µL/well 1-Step™ Ultra TMB-ELISA Substrate Solution for 8 min. The reaction was stopped with 100 µL/well 1 M sulfuric acid and the absorbance at 450 nm was read using a plate reader (Synergy Neo2, BioTek Instruments). The data were used to calculate a single heparin score for each ADC. First, the mean values of the measured triplicates were calculated. Second, these results were normalized by dividing the mean values of each ADC concentration by the mean value of the assay buffer control. Finally, the mean of the normalized results of the different sample concentrations (20.0-0.03 µg/mL) of each ADC was calculated to get the heparin score.

7. Results and Discussion

Parts of this work have been published.¹

7.1. Relationship Between HIC, huFcRn Affinity, and Thermal Stability Analysis of ADCs Conjugated at Different Conjugation Sites and Their Pharmacokinetics

To explore the parameters hydrophobicity, thermal stability, and FcRn binding as indicators for PK, an ADC series conjugated at different positions using two different conjugation techniques were used. ADCs with this design property were selected for the study, since it was shown that the conjugation site can impact the PK of ADCs.^{49,80,171} In addition, the use of these ADCs enables systematic comparison of different conjugation sites using the *in vitro* assays and PK analysis, which could allow identification of conjugation sites that lead to positive physicochemical properties of the final ADCs.

ADC hydrophobicity was analyzed by HIC (section 7.1.2), ADC thermal stability was determined by nanoDSF (section 7.1.3), and ADC binding to huFcRn was measured by BLI (section 7.1.4). Moreover, the serum stability of ADCs was analyzed (section 7.1.5) as a preliminary deconjugation in the circulation would reduce the ADC concentration in the blood in addition to the non-specific clearance route and would increase the blood concentration of unconjugated mAb. However, before the assay results will be shown and discussed in terms of the conjugation sites and associated conjugation method, the details about the design of the ADCs and their generation will be described first.

7.1.1. ADC Design and Generation

To enable a systematic comparison between different conjugation sites and associated conjugation methods, the same cleavable linker-payload moiety VC-PAB-MMAE was used for all generated ADCs. Furthermore, for the first set of eight ADCs the anti-HER2 antibody trastuzumab was used as mAb scaffold. The conjugation was either done by site-specific cysteine conjugation or mTG-conjugation, to achieve a DAR of approximately 2.

A total of five different cysteine conjugation sites were investigated, comprising two recently discovered positions described by Wozniak-Knopp *et al.*, N325 and L328,⁷⁷ as well as three well-described sites from literature: S239, D265, and S442 (see section 4.2.4). Positions S239, D265, N325, and L328 are located within the antibody C_H2 domain, whereas S442 is located at the HC C-terminus (**Figure 12**). To enable cysteine conjugation, trastuzumab was engineered by substitution of the corresponding amino acid by a

cysteine residue (T-S239C, T-D265C, T-N325C, T-L328C, T-S442C). Furthermore, the linker-payload comprised a maleimidocaproyl moiety (MC-VC-PAB-MMAE) which reacts selectively with thiol groups from cysteines. Three additional trastuzumab-ADCs were generated enzymatically by mTG. Therefore, the well-known recognition motifs LLQGA and GLLQGPP⁸⁰ were fused to the C-terminus of the HC of trastuzumab by substitution of the residue K447 (T-HC) or to position 214 of the trastuzumab LC (T-LC), respectively. Moreover, an engineered mTG enzyme variant¹⁶⁸ was used for conjugation at position Q295 within the C_H2 domain of native trastuzumab (T-Q295). For mTG-mediated conjugation the linker-payload contained a triple-glycine sequence-motif (G₃-VC-PAB-MMAE) as acyl acceptor instead of a maleimide moiety. To better understand the interplay of the antibody scaffold and the conjugation site, two conjugation sites, the engineered cysteine residue at position L328 and the C-terminal LC position for mTG mediated conjugation, were combined with two additional antibody scaffolds, the anti-IL-12/23p40 antibody briakinumab (B-L323C and B-LC) and the anti-IL-17A antibody secukinumab (S-L328C and S-LC). All mTG LC variants additionally comprised the substitution Q295A to prevent undesired conjugation to this position.

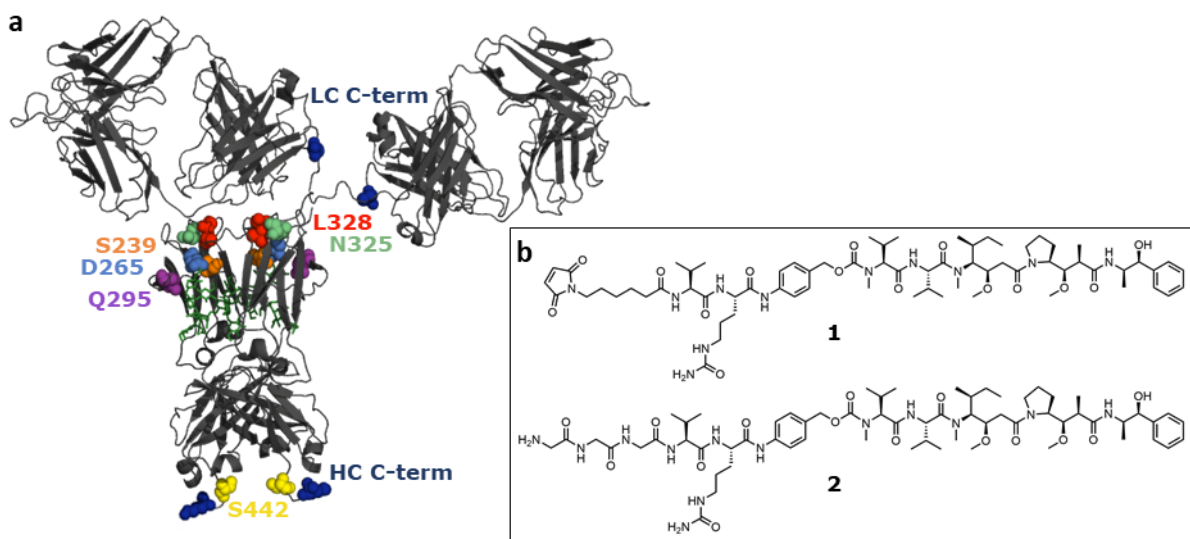


Figure 12. Conjugation sites and linker-payloads for site specific conjugation via mTG and via engineered cysteines used for systematic characterization. a) Ribbon model of an IgG1 antibody with colored spheres highlighting the engineered cysteine conjugation sites, S239, D264, N325, L328, and S442, as well as the mTG conjugation sites, engineered C-terminal LC and HC positions and Q295. Model derived from PDB entry 1HZH. b) Linker-payloads used for the cysteine conjugation, MC-VC-PAB-MMAE (1), and mTG-catalyzed conjugation, G₃-VC-PAB-MMAE (2).

The conjugation of all ADCs was successful and yielded homogeneous ADCs with DARs ranging from 1.96 to 2.37 and high purity $\geq 99.4\%$ (analyzed by SEC, **Table 4**). For ADCs with a DAR ≥ 2 (6 out of 12 ADCs), the final product contained byproduct of ADC species conjugated at additional positions. The detection of byproduct species by MS is exemplarily shown in Figure A.1 in the appendix for the trastuzumab-based ADC conjugated

at position S239C via cysteine conjugation, T-S239C-MMAE, containing the highest amount of byproduct (18.4%) of all analyzed ADCs. Presumably for cysteine conjugated ADCs, additional ADC species in the LC or HC arose from conjugation to reactive endogenous cysteines of the mAb, generated by the required reduction-oxidation step.¹⁷² For mTG-conjugated ADCs no byproduct was observed except for B-LC-MMAE (6.0%) showing that in the LC for briakinumab another glutamine residue can act as substrate for mTG (Figure A.2, appendix). Since the portion of byproduct in the ADCs was only minor, no further attempts were made to identify the exact conjugation positions. Overall, the generated ADCs were suitable to investigate the influence of the different conjugation sites and methods on the physicochemical and pharmacokinetic properties of the molecules.

In the following sections, first the results of all ADCs in each assay are discussed in terms of the ADC design (section 7.1-7.1.5), followed by the presentation and discussion of the PK results of all ADCs that were analyzed in huFcRn transgenic mice (hemizygous Tg276; section 7.1.6), and finally HIC, nanoDSF, and FcRn binding affinity (BLI) results of the ADCs were correlated with their *in vivo* clearance values to investigate whether these assays could be used as indicators for ADC PK (section 7.1.7).

Table 4. Purity and DAR of the cysteine and mTG-conjugated ADCs. Purities of the generated ADCs were measured by SEC (section 6.20) and DAR was determined by LC-MS (section 6.22).

ADC	Purity (%)	DAR
T-S239C-MMAE	100.0	2.37
T-D265C-MMAE	99.4	2.13
T-N325C-MMAE	99.7	2.11
T-L328C-MMAE	100.0	2.01
T-S442C-MMAE	100.0	2.17
T-Q295-MMAE	100.0	2.00
T-HC-MMAE	100.0	2.00
T-LC-MMAE	100.0	2.00
S-L328C-MMAE	100.0	2.08
S-LC-MMAE	99.8	1.96
B-L328C-MMAE	99.4	2.00
B-LC-MMAE	100.0	2.12

7.1.2. Hydrophobicity of the ADCs

The hydrophobicity of an ADC is an imported parameter as it can influence the PK and stability of ADCs.^{35,56} A widely used methods to assess the hydrophobicity of ADCs is hydrophobic interaction chromatography (HIC). Since most linker-payloads are hydrophobic, HIC can be used for drug distribution and DAR analyses of ADCs conjugated to the interchain-disulfides or to specifically engineered sites.¹⁷³ Beside for DAR analysis, it has been demonstrated that HIC can be used as an indicator for the solvent accessibility of hydrophobic linker-payloads.¹⁷¹ The more hydrophobic an ADC is compared to its parental mAb, the greater is the solvent accessibility of the linker-payload.¹⁷¹ Linker-payloads with a high solvent accessibility are less shielded which can have a negative impact on the stability in the circulation.^{49,171} In addition, varying accessibility of the linker-payload for proteases can translate into different ADC cleavage kinetics inside the target cell.¹⁷¹ Also the general hydrophobicity of an ADC is an import parameter as a high apparent hydrophobicity has been shown to be associated with a poor PK of ADCs in mice and rats.³⁵ Therefore, to analyze both, the solvent accessibility of the linker-payload and the general hydrophobicity of the ADCs, two different results of the HIC measurement were used in this study: The relative retention time (rRT) and the normalized retention time (nRT), respectively.

For calculation of the general hydrophobicity the normalized HIC retention times of the ADCs were used. To consider variability within the assay, the retention time of the main product of each ADC (the DAR 2 species) was normalized to the results of a defined standard which was measured in every experiment resulting in nRT (for more information on the calculation see section 6.21). Most of the ADCs exhibited similar HIC nRTs (0.18-0.34), whereas four of the ADCs showed increased hydrophobicity (**Figure 13, a**): Prolonged HIC nRTs were determined for both secukinumab-ADCs, S-L328C-MMAE (0.52) and S-LC-MMAE (0.55), and for the two trastuzumab-based ADCs conjugated at the HC C-termini, T-S442C-MMAE (0.77) and T-HC-MMAE (0.79).

To calculate the rRTs, the retention time (RT) of the ADC, DAR 2 species, was divided by the RT of its parental mAb (see section 6.21). Within the panel of trastuzumab-ADCs only ADCs conjugated at the HC C-termini (T-S442C-MMAE and T-HC-MMAE) showed higher HIC rRTs with 1.57 and 1.72 compared to other trastuzumab-ADCs (rRTs 1.14-1.28). This shows that for both ADCs the conjugation is accountable for the high apparent hydrophobicity of the ADCs, indicating that ADCs conjugated within the exposed HC C-termini of the mAb resulting in most pronounced solvent accessibility of the linker-payload (**Figure 13, b**). Consistent with these results, long HIC retention times were previously reported for an trastuzumab-VC-PAB-MMAE ADC conjugated at position L443C.¹⁷¹ Among the different antibody scaffolds the LC C-termini and L328C conjugates showed similar HIC rRTs, whereas secukinumab-ADC HIC rRTs (1.11 and 1.10) were generally lower and briakinumab-ADC HIC-rRTs (1.36. and 1.33) generally higher than trastuzumab-ADC HIC rRTs (1.28 and 1.27). Although the conjugation of the linker-payload to the briakinumab-based mAbs led to a stronger

increase in hydrophobicity compared to the corresponding trastuzumab-ADCs, the hydrophobicity of the resulting ADCs was comparable between trastuzumab- and briakinumab-based ADCs (nRTs of 0.30-0.34). In contrast, both secukinumab-ADCs showed the lowest HIC nRTs within the panel of all generated ADCs (1.11 and 1.10) but high HIC rRTs (0.52 and 0.55). In this case the antibody scaffold and not the conjugation can be mainly accounted for the elongated HIC nRTs of the secukinumab-based ADCs. To evaluate if the HIC parameters would serve as indicators for PK, HIC rRT and nRT results of the ADCs were correlated with the total antibody clearance of the ADCs in huFcRn transgenic mice, as shown in section 7.1.7.

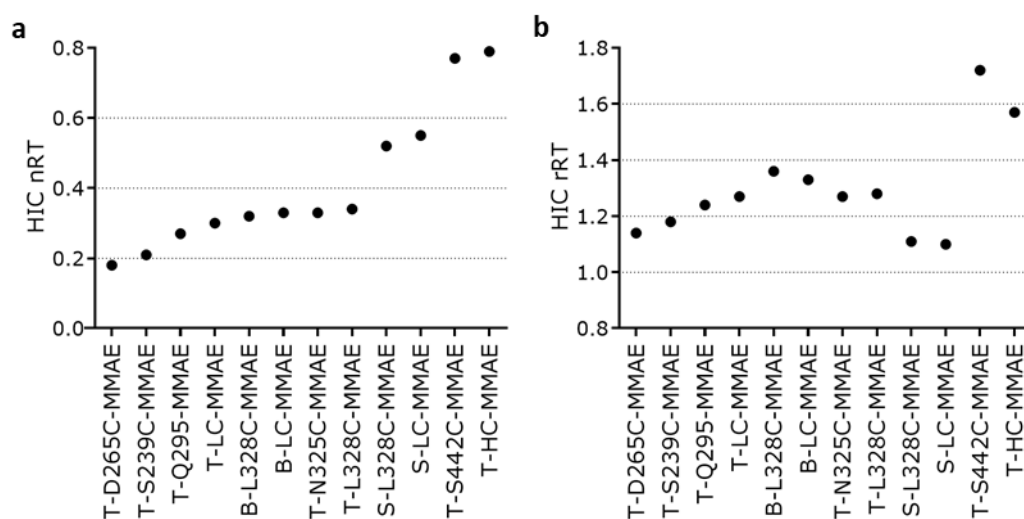


Figure 13. Hydrophobicity of the ADCs measured by HIC. **a)** HIC normalized retention times (nRTs) of the different ADCs were calculated by normalization of the retention time of the main product to a defined standard comprising ADC species with different DAR. **b)** HIC relative retention times (rRTs) were calculated by dividing the retention time of the ADC DAR 2 species by the retention time of the respective parental mAb.

7.1.3. Thermal Stability of the ADCs

Since the conjugation could destabilize the conformational stability of antibodies¹⁷⁴ which could enhance the aggregation tendency of the molecule¹⁷⁵ and may negatively impact the PK,¹⁷⁶ the thermal stability of the ADCs and corresponding native mAbs was analyzed by nano differential scanning fluorimetry (nanoDSF, section 6.28). Herein, the obtained first (T_{m1}) and second (T_{m2}) transition temperatures attribute to unfolding of the C_H2 domain and unfolding of the Fab/ C_H3 domain, respectively.¹⁷⁷ Exemplarily raw data of the unfolding curve and the first derivate indicating the transition temperatures are shown in **Figure 14, a and b**, whereas the results of all ADCs and mAbs are shown in **Figure 14, c**. For raw data of all analyzed molecules, the reader is referred to Figure A.3 in the appendix. All three native mAbs showed high thermal stabilities with T_{m1} (>70°C) and T_{m2} (>80°C) values similar to those observed for other mAbs.^{177,178} In accordance with previous reports,¹⁷⁶ conjugation to the highly stable C_H3 domain did not lead to a change in thermal stability

of the T-HC-MMAE and T-S442C-MMAE ADCs. In contrast, a decrease in T_{m1} was determined for all other ADCs which were conjugated at the C_{H2} domain or at the C-termini of the LC located close to the hinge region. Compared to the corresponding native mAb, a drop in T_{m1} ranging between 3.7°C and 7.2°C was analyzed for B-LC-MMAE, T-LC-MMAE, T-Q295-MMAE, T-S239C-MMAE, and T-D265C-MMAE. The two trastuzumab-ADCs conjugated at the positions N325C and L328C, which are located closer to the Fab domain and more exposed to the surface than the other positions in the C_{H2} domain, exhibited the most pronounced decrease in T_{m1} of the trastuzumab-ADCs (9.3°C and 10.7°C, respectively). Within the C_{H2} domain large hydrophobic surfaces are exposed to the solvent resulting in decreased stability of the C_{H2} domain than the other domains.¹⁷⁹ Therefore, an enlargement of the hydrophobic surface by attaching a hydrophobic linker-payload to or close to this domain could be most critical for the stability of the C_{H2} domain. A high drop in T_{m1} compared to the corresponding native mAbs was additionally determined for B-L328C-MMAE (11.9°C) and S-L328C-MMAE (17.2°C). Interestingly, also S-LC-MMAE exhibited a great reduction in T_{m1} of 13.9°C. As shown before (section 7.1.2), long HIC nRTs were determined for both secukinumab-ADCs which was mainly attributable to the mAb scaffold. Therefore, the more pronounced hydrophobicity of secukinumab could be an explanation for the more pronounced effect on T_{m1} for S-LC than for T-LC and B-LC. Moreover, a drop in T_{m2} compared the native mAb was determined for S-L328C-MMAE and S-LC-MMAE (4.9°C and 5.3°C, respectively). An even greater reduced Fab domain stability was determined for B-L328C-MMAE (12.8°C), while for all other ADCs similar T_{m2} values (78.6°C-80.9°C) were observed indicating high Fab domain stabilities. Therefore, in addition to the site of conjugation, the Fab domain of the antibody seemed to have a strong impact on the conformational stability of the ADCs. Similar findings have been reported with regard to FcRn binding: Even though the FcRn binding site is located at the C_{H2} - C_{H3} domain interface, it has been shown that the variable domain of the antibody can influence the binding to FcRn.¹²⁴⁻¹²⁶ As for the HIC readouts, the correlation of the thermal stability readouts and the total antibody clearance of the ADCs in Tg276 mice will be addressed in section 7.1.7.

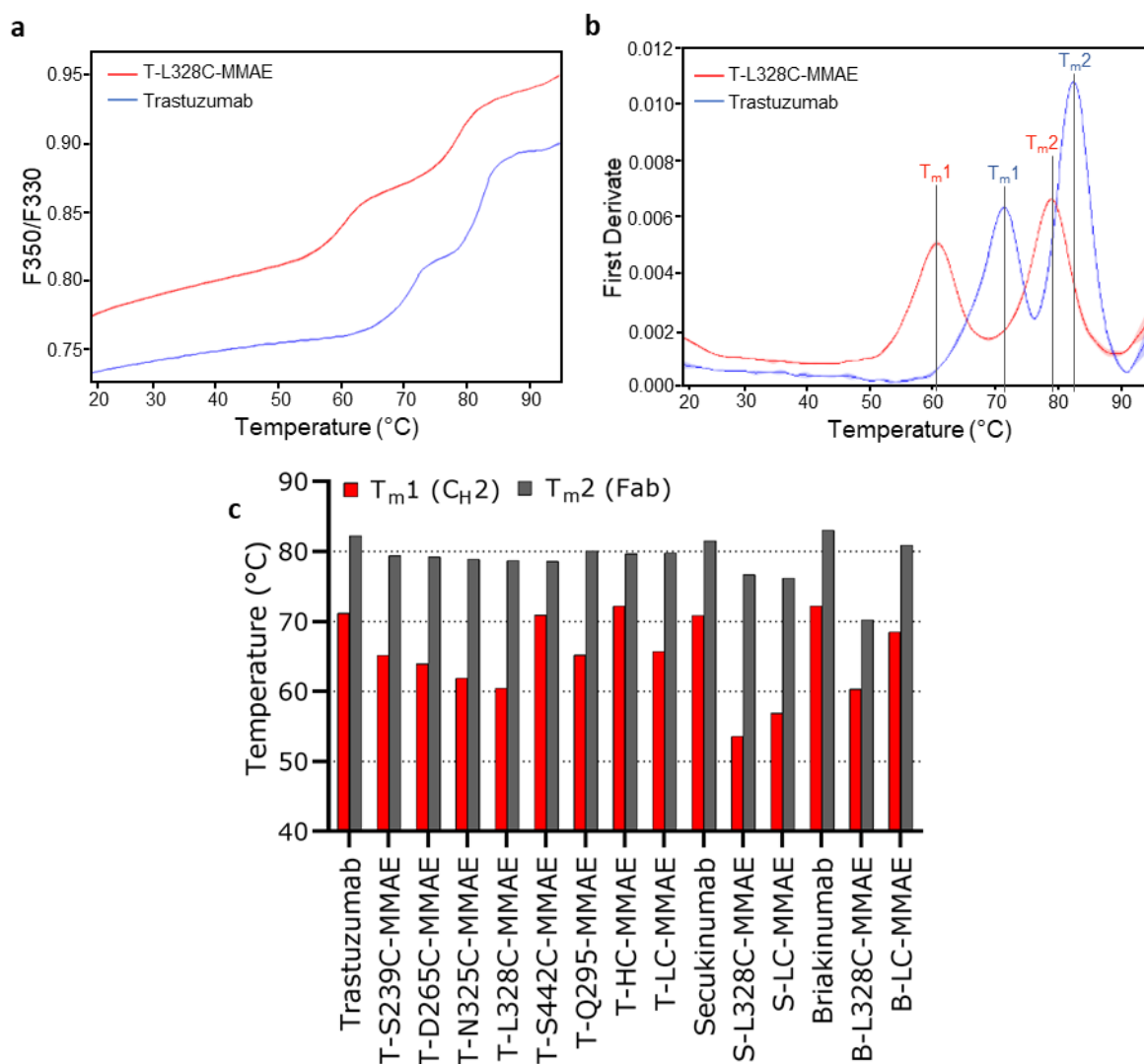


Figure 14. Thermal stability of ADCs and corresponding native antibodies measured by nanoDSF. a) Exemplary melting curve and (b) corresponding first derivative indicating transition midpoints T_{m1} (C_H2 domain) and T_{m2} (Fab domain) of trastuzumab (blue) and T-L328C-MMAE (red). c) Summary of T_{m1} (red bars) and T_{m2} (gray bars) of the different ADCs and native mAbs. Shown are the mean values of two measurements.

7.1.4. Binding Kinetics to Soluble huFcRn

The interaction with FcRn plays a key role for the long serum half-life of antibodies (see also section 4.3.1).¹¹⁴ As mentioned above, it was reported that antibody regions distinct from the FcRn binding site can influence the interaction with FcRn.^{124–126} Therefore, attaching a linker-payload to a mAb, even if not located within the FcRn binding site, could potentially impact the interaction with FcRn and therefore the PK. To analyze the interaction with FcRn, ADCs or corresponding native mAbs were immobilized on biosensors and their binding behavior to soluble recombinant huFcRn was analyzed at pH 6.0 using Bio-Layer Interferometry (BLI, section 6.30.1, representative sensorgram: **Figure 15, a**). The analyzed binding rate values of all mAbs and ADCs

(Table 5) varied only over a 2-fold range (K_D 464-1004 nM) indicating that conjugation at the different selected sites had no effect on interaction with huFcRn. Commonly, a difference of 7 to 10-fold in FcRn binding affinity (K_D) is thought to have the potential to effect PK of molecules.¹¹⁰ In addition, very fast dissociation at pH 7.4 after association at pH 6.0 (representative sensorgram: Figure 15, b, green lines) and no detectable binding to huFcRn at pH 7.4 (representative sensorgram: Figure 15, b, pink line) has been determined for all molecules (data not shown).

Table 5. FcRn binding kinetics of ADCs and native mAbs. Binding affinity (K_D), association rate (k_a) and dissociation rate constant (k_d) were measured by BLI at pH 6.0 using soluble recombinant huFcRn and immobilized ADCs or mAbs. Mean and corresponding standard deviation (SD) values of at least two independent measurements are shown.

Antibody or ADC	K_D (nM)	k_a ($\times 10^5$ M ⁻¹ s ⁻¹)	k_d (s ⁻¹)
Trastuzumab	564 (\pm 12)	3.25 (\pm 0.56)	0.17 (\pm 0.03)
T-S239C-MMAE	708 (\pm 42)	3.59 (\pm 0.51)	0.26 (\pm 0.05)
T-D265C-MMAE	481 (\pm 49)	3.98 (\pm 1.71)	0.19 (\pm 0.08)
T-N325C-MMAE	520 (\pm 56)	4.23 (\pm 0.36)	0.22 (\pm 0.01)
T-L328C-MMAE	516 (\pm 74)	5.06 (\pm 2.41)	0.25 (\pm 0.10)
T-S442C-MMAE	475 (\pm 30)	2.61 (\pm 0.80)	0.13 (\pm 0.05)
T-Q295-MMAE	501 (\pm 24)	2.98 (\pm 0.22)	0.15 (\pm 0.02)
T-HC-MMAE	1004 (\pm 128)	1.91 (\pm 0.42)	0.19 (\pm 0.02)
T-LC-MMAE	464 (\pm 78)	3.75 (\pm 0.99)	0.18 (\pm 0.08)
Secukinumab	773 (\pm 126)	2.69 (\pm 0.29)	0.21 (\pm 0.01)
S-L328C-MMAE	686 (\pm 32)	3.81 (\pm 0.69)	0.26 (\pm 0.04)
S-LC-MMAE	691 (\pm 9)	3.67 (\pm 0.04)	0.25 (\pm 0.01)
Briakinumab	508 (\pm 57)	4.33 (\pm 0.50)	0.22 (\pm 0.01)
B-L328C-MMAE	551 (\pm 5)	4.66 (\pm 0.93)	0.26 (\pm 0.05)
B-LC-MMAE	621 (\pm 64)	2.82 (\pm 0.79)	0.17 (\pm 0.03)

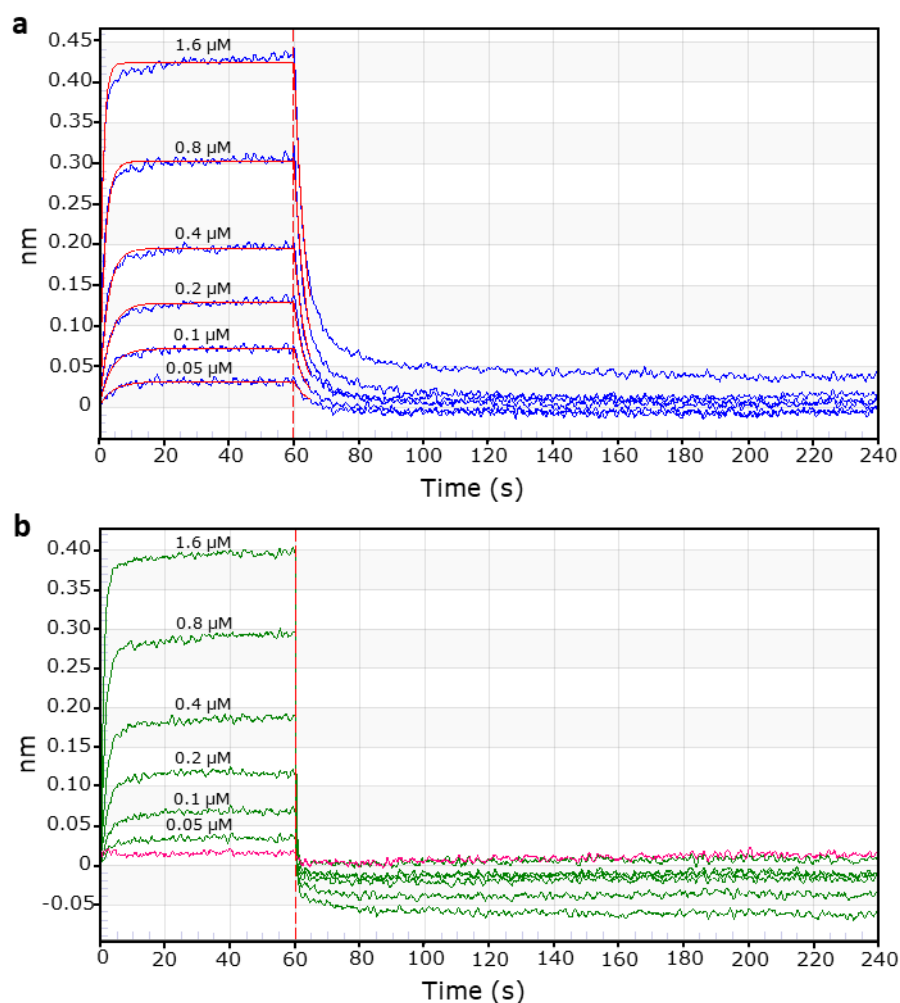


Figure 15. Representative BLI sensorgrams of the association and dissociation profiles of immobilized T-LC-MMAE and soluble recombinant huFcRn (1.6-0.05 μM). Association was measured for 60 s, followed by dissociation for 180 s. **a)** Assay was performed at pH 6.0. Binding curves (blue lines) were fitted with a 1:1 interaction model, using the complete association and the first 5 s of dissociation (red lines). **b)** Association was performed at pH 6.0 while dissociation was performed at pH 7.4 (green lines). Furthermore, both association and dissociation were performed at pH 7.4 with 1.6 μM recombinant huFcRn (pink line).

7.1.5. *In Vitro* Mouse Serum Stability of the ADCs

As deconjugation can potentially lead to undesirable non-target related toxicities, compromise efficacy and PK and impact the immunogenicity of the molecule, it is of utmost importance to generate ADCs which are stable in circulation.^{180,181} It is well documented that the site of conjugation sensitively impacts the ADC stability.^{49,56,60,80} To investigate conjugate stability in circulation, the different ADCs were incubated for 96 h in mouse serum. As maleimides can undergo retro-Michael reaction, presumably with albumin, leading to a transfer of the linker-payload to albumin,^{49,59} two orthogonal methods were used for monitoring the stability: released MMAE was detected via LC-MS/MS (section 6.23) and remaining intact ADC profiles were analyzed

using an antibody-conjugated-payload ELISA method (section 6.23). Only minor amounts of free payloads (0.3-5.2%) and a minor reduction of intact ADC portion (0-15.7%) were detected for most of the ADCs after 96 h of incubation (**Figure 16**, the results of all analyzed timepoints up to 96 h are shown in Figure A.4, appendix). Since similar stability profiles have been obtained for the ADCs based on engineered cysteine mAbs (ECM-ADCs) using both methods, pronounced retro-Michael reaction could not be detected. For different ECM-ADCs conjugated at the C_{H2} domain close to hinge region, Sussman *et al.* reported different stability in rat plasma. Of them an ADC conjugated at position S239 was stable while the position E269, K326, and A327 were less stable.⁵⁶ The results shown here could confirm the favorable stability profile of ADCs conjugated at position S239. Furthermore, even though the conjugation positions of the other ECM-ADCs conjugated at the C_{H2} domain shown in here (T-D265-MMAE, T-N325-MMAE, T-L328-MMAE, B-L328-MMAE, and S-L328C-MMAE) were located in proximity to the less stable positions described by Sussman *et al.*,⁵⁶ no stability issues in mouse serum were found for these positions.

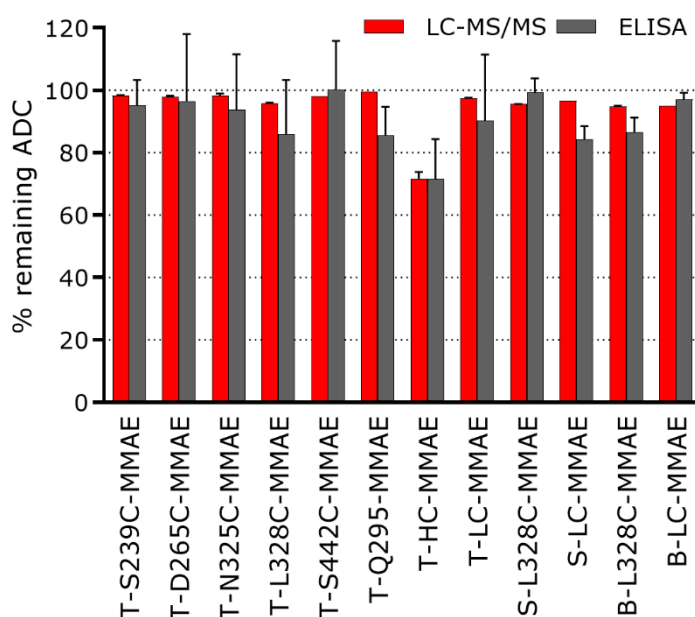


Figure 16. Mouse serum stability measurements via orthogonal conjugated-payload ELISA or free payload LC-MS/MS. ADCs were incubated for 96 h in mouse serum before the fraction of intact ADC was measured by antibody-conjugated-payload ELISA (gray bars) and conjugated-payload (in % ADC remaining) was calculated from free MMAE measured via LC-MS/MS (red bars). Measurements were performed in duplicates. Error bars represent standard error of the mean (SEM).

Of all different ADCs that were analyzed only T-HC-MMAE showed elevated MMAE release of up to 28.3% after 96 h measured with both methods. This elevated instability is in line with literature where an instability for ADCs conjugated at this position was reported.^{80,84,85} Dorywalska *et al.* demonstrated for a similar ADC that this instability was caused by an enzymatic cleavage of the VC-PAB-linker by the murine Carboxylesterase

1C (Ces1C).⁴⁵ The authors supposed that the linker-payload at the solvent exposed HC C-terminus is more accessible to Ces1C while other positions, for example, Q295 or LC C-terminus, protect the VC-PAB-linker motif by sterically hindrance of the large Ces1C.^{80,84} Nevertheless, measuring high solvent exposure by HIC, as seen for T-HC-MMAE (section 7.1.2), does not seem to be an appropriate method to predict stability issues in circulation. In contrast to T-HC-MMAE, T-S442C-MMAE was stable in mouse serum even though similar HIC rRTs were determined for both ADCs (section 7.1.2). A higher HIC retention time, but a high stability was also reported for an ECM-ADC conjugated at position L443.¹⁷¹ In this report, HIC results were shown to correlate with intracellular linker cleavage by the lysosomal protease cathepsin B rather than with cleavage in circulation by Ces1C.¹⁷¹ Because lysosomal cleavage was not investigated as critical attribute for PK, within the scope of this work this alternative finding was not assessed. An explanation for the observed differences in stability of both HC C-terminally conjugated ADCs could be the small difference in conjugation position that could lead to a different linker exposition. T-S442C-MMAE is conjugated close to the C-terminus but still four residues distant to the N-terminus, whereas T-HC-MMAE is conjugated within the mTG-tag replacing the C-terminal lysine. In fact, structural modeling of both ADCs (**Figure 17, a**) showed that the linker-payload of T-HC-MMAE (**Figure 17, c**) is presumably more solvent exposed than the linker-payload of T-S442C-MMAE (**Figure 17, b**).

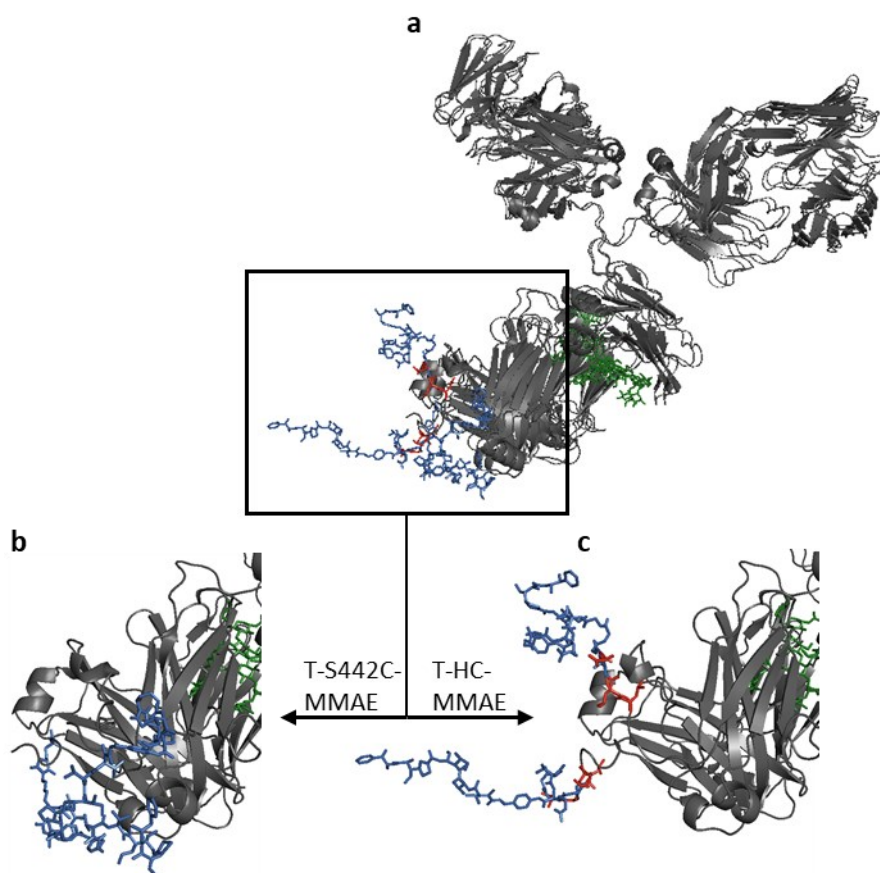


Figure 17. Comparative analysis of structural models of the T-HC-MMAE and T-S442C-MMAE. An Overlay of both ADCs (a) and separated, enlarged views of the C_{H3} domain with conjugated linker-payload (blue sticks, b and c) are shown. Conjugation of MC-VC-PAB-MMAE to the engineered cysteines at position S442 resulted in an ADC, T-S442C-MMAE (b), where the payloads is presumably more likely oriented towards the antibody. In contrast, enzymatically conjugation of G_3 -VC-PAB-MMAE to the C-terminus of the HC at a tag (red sticks) resulted in an ADC, T-HC-MMAE, where the linker-payload is presumably more solvent exposed (c). ADC structures were generated by Dr. Andreas Evers (Merck KGaA): Structural models of the mAbs were generated with the application Antibody Modeler of the platform Molecular Operation Environment (MOE; Chemical Computing Group, September 2020) and the linker-payloads were attached by the Bio MOE extension. Automatically generated rotamer libraries of the linker-payloads were screened at the respective conjugation positions and the conformation with the most favorable energy values of the selected force field (Amber) was automatically selected. Finally, the entire ADCs were subjected to global energy minimization (in the Amber force field). Visualization of the resulting molecules was performed using PyMOL 2.3 (Schrodinger, LLC).

7.1.6. Pharmacokinetics and Stability of the ADCs in huFcRn Mice

The PK behavior of ADCs conjugated at the well-known engineered cysteine conjugation sites S239 and S442 and at the mTG sites C-terminally at the LC and HC have already been reported, but the different ADC design regarding to the mAb backbone and linker-payload and the different animal species employed in these reports did not allow for a systematic comparison of the conjugation sites.^{63,65,80} Until now, only a few reports are published where the influence of different conjugation sites of ADCs on the PK was investigated.^{49,58,80,84}

In this work, beside a comprehensive comparison of different conjugation sites with different *in vitro* assays that may be suitable to indicate PK of the ADCs, the PK of all ADCs and native mAbs was analyzed in Tg276 huFcRn transgenic mice (hemizygous) that have the potential for human PK projection (further details about the mouse model can be found in section 4.3.3). Therefore, the different ADCs, secukinumab, and briakinumab were administered at 3 mg/kg to the huFcRn transgenic mice. Trastuzumab was dosed with 4.7 mg/kg. Different doses could influence the PK if the mAb target is available. Binding to the target affects the drug disposition (target mediated drug disposition, TMDD) and can cause nonlinear PK across different doses.¹⁸² However, all mAb scaffolds that were used in this study are not cross-reactive to the murine target.^{183–185} Therefore, TMDD cannot occur and potential differences in the clearance can only be caused by different behavior with respect to non-target related clearance mechanisms (section 4.3.1).

The plasma samples were analyzed for their total antibody and antibody-conjugated payload concentration profiles. Total antibody concentrations were determined using a sensitive electrochemiluminescence LBA (LLOQ = 0.34 nM, section 6.25). To avoid the possibility that differences in the total antibody profile of the ADCs is caused by undesirable DAR-sensitivity of the capture and detection-reagents,¹⁶² the DAR insensitivity of the LBA reagents was previously confirmed for all ADC variants as exemplarily shown in Figure A.5 in the appendix. To evaluate ADC stability, a hybrid affinity capture LC-MS/MS method (LLOQ = 13.9 nM, section 6.26) was used to measure the amount of payload still attached to the antibody (antibody-conjugated payload). For this method, the quantitative capture of the ADCs by protein A was confirmed (data not shown). The determined *in vivo* stability of the ADCs was in line with the previously determined *in vitro* stability in mouse serum (section 7.1.5). At DAR 2 two molecules of payload are associated with one mAb molecule. If the antibody is stable, the molar concentration of antibody-conjugated payload remains twice as high as the molar concentration of total antibody and both profiles are similar. Therefore, most ADCs showed a great stability, as indicated by similar antibody-conjugated payload (**Figure 18**, red lines) and total antibody concentration profiles (**Figure 18**, blue lines). In contrast, T-HC-MMAE showed pronounced de-conjugation of MMAE. Already 24 h after dosing, the molar concentration of MMAE was slightly lower than the molar concentration of total antibody, indicating a DAR below 1. Overall, for this ADC the conjugated MMAE was cleared 2.3-times faster than the total antibody (**Table 6**). Therefore, unconjugated mAb contributes to the total antibody CL calculation of T-HC-MMAE.

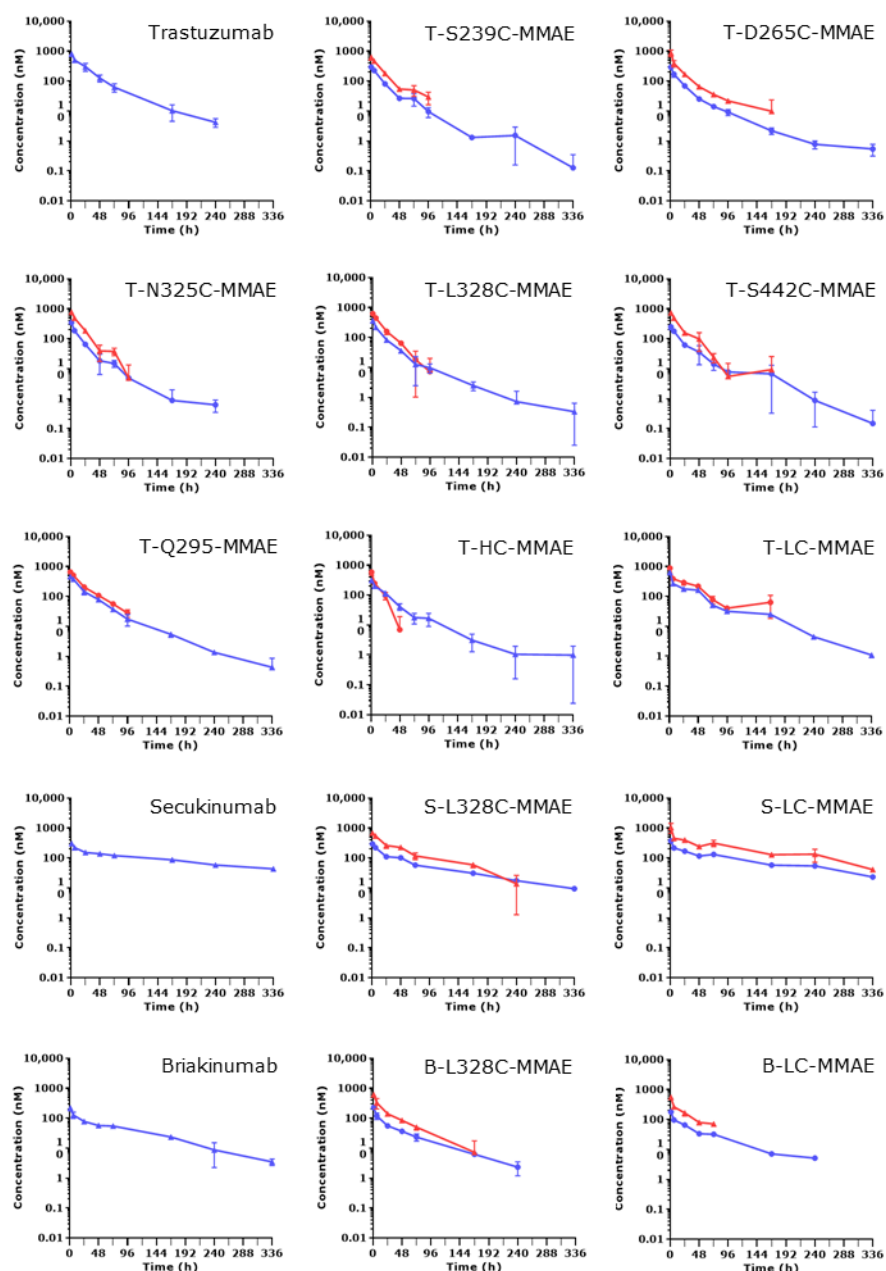


Figure 18. Pharmacokinetic profiles of the ADCs and native mAbs in huFcRn mice. Represented are the total antibody LBA profiles (LLOQ = 0.34 nM, blue lines) and antibody-conjugated MMAE LC-MS/MS profiles after forced release of the payload from the ADC (LLOQ = 13.9 nM, red lines). ADCs, secukinumab, and briakinumab were given as single intravenous dose at 3.0 mg/kg and trastuzumab at 4.7 mg/kg.

Although the other ADCs were stable and all ADCs showed a similar binding to human FcRn (section 7.1.4), pronounced differences in the total antibody CL were found (Table 6). Of the trastuzumab-ADCs only T-LC-MMAE (1.18 mL/h/kg) and T-Q295-MMAE (1.66 mL/h/kg) showed a slightly reduced or similar CL compared to trastuzumab (1.50 mL/h/kg). Beneficial PK behavior of ADCs conjugated to position Q295 of aglycosylated antibodies have been already reported.⁸¹ Therefore, even though shown for the first time, it is not surprising

that also an ADC conjugated to Q295 of a fully glycosylated mAb showed a beneficial PK behavior. In contrast, a CL of 2.55 mL/h/kg was determined for the third mTG-conjugated ADC, T-HC-MMAE, although it was less stable. In line with this finding, Strop *et al.* analyzed a 3-times faster total antibody CL in rats for a HC C-terminally conjugated mTG-ADC compared to an ADC conjugated C-terminally at the LCs.⁸⁰ However, in SCID mice they analyzed a similar total antibody PK for both ADCs.⁸⁰ Furthermore, conjugation to the ECM positions L328C and S239C led to a similar elevated CL like determined for T-HC-MMAE with values of 2.94 and 3.04 mL/h/kg, respectively. Even faster CL values of 3.41, 3.58, and 3.77 mL/h/kg were detected for trastuzumab-ADCs conjugated to the position S442C, D265C, and N325C, respectively. Despite the determined faster clearance of all engineered cysteine ADCs compared to the mTG ADCs, the position S239 is the most commonly employed ECM conjugation site which has been used for different ADCs that have been investigated in clinical trials.^{56,62,64,66,68,70,71} Furthermore, ADCs with a beneficial *in vitro* and *in vivo* behavior were generated by conjugation to the ECM sites S442 and D265 (see also section 4.2.4).^{63,74,75} Therefore, in comparison to the well-established ECM conjugation sites, the two recently identified conjugation sites, N325 and L328,⁷⁷ can be considered suitable sites for conjugation using engineered cysteines even though the two mTG-conjugated ADCs, LC C-terminal and Q295, showed a superior PK behavior.

To additionally investigate if the observed influence of the conjugation site on the PK is similar between different antibody scaffolds, the best performing positions of both conjugation methods L328C as well as the C-terminal LC mTG-position were combined with additional antibodies. For this, briakinumab and secukinumab were chosen due to the differing PK reported for both antibodies. The linear CL values published from intravenous PK studies in humans are 0.11 L/day for secukinumab, 0.23 L/day for trastuzumab, and 0.81 L/day for briakinumab.^{184,186,187} Correspondingly, in Tg276 mice the slowest CL was observed for secukinumab (0.49 mL/h/kg), followed by trastuzumab (1.50 mL/h/kg) and finally briakinumab (1.82 mL/h/kg, **Table 6**). Irrespectively of the used mAb scaffold, ADCs conjugated C-terminally at the LCs had a better PK profile than ADCs conjugated to position L328C (**Figure 19**). But the overall impact of the different conjugation sites was strongly dependent on the antibody scaffold: The total antibody CL of S-L328C-MMAE (1.18 mL/h/kg) was 2-times faster than the CL of S-LC-MMAE (0.63 mL/h/kg) and 2.4-times faster than secukinumab. But even so, S-L328C-MMAE was still cleared slower than trastuzumab. For the briakinumab-ADCs the effect of the conjugation sites was less pronounced. B-L328C-MMAE showed a total antibody CL of 3.44 mL/h/kg and B-LC-MMAE of 3.11 mL/h/kg. Conjugation C-terminally to the LC had only a minor effect on the PK of trastuzumab and secukinumab, but it resulted in an accelerated CL in the context of briakinumab. Consequently, although the conjugation position can have a major impact on the CL, the antibody scaffold can abrogate this influence and both ADC components need to be put into perspective.

Table 6. Total antibody and antibody-conjugated MMAE pharmacokinetics in huFcRn mice. The ADCs, secukinumab, and briakinumab were administration intravenously to huFcRn mice with a dose of 3.0 mg/kg, while for trastuzumab a dose of 4.7 mg/kg was used.

mAb or ADC	Total antibody			Ab-conjugated MMAE			CL _{Ab-conj.} MMAE/CL _{total} Ab (%)
	C _{max} (ng/mL)	AUC _{0-inf} (h*ng/mL)	CL (mL/h/kg)	C _{max} (ng/mL)	AUC _{0-inf} (h*ng/mL)	CL (mL/h/kg)	
Trastuzumab	118000	3130000	1.50	-	-	-	-
T-S239C-MMAE	42600	985000	3.04	452	10500	3.32	109
T-D265C-MMAE	42100	838000	3.58	627	10500	2.94	82
T-N325C-MMAE	50300	796000	3.77	557	9900	3.13	83
T-L328C-MMAE	53000	1020000	2.94	445	9380	3.20	109
T-S442C-MMAE	36400	880000	3.41	525	11100	2.89	85
T-Q295-MMAE	65800	1810000	1.66	467	14100	1.85	111
T-HC-MMAE	46000	1180000	2.55	418	5050	5.74	225
T-LC-MMAE	93500	2540000	1.18	629	17100	1.58	134
Secukinumab ^{*1}	45000	6140000	0.49	-	-	-	-
S-L328C-MMAE	43300	2550000	1.18	483	23000	1.22	103
S-LC-MMAE	55200	4760000	0.63	750	51000	0.53	84
Briakinumab	31400	1650000	1.82	-	-	-	-
B-L328C-MMAE ^{*2}	32900	873000	3.44	438	9780	3.07	89
B-LC-MMAE	25900	964000	3.11	399	10000	3.00	96

^{*1} The CL and AUC_{0-inf} of total antibody are expected to be less accurate since the percent of extrapolated AUC_{0-inf} was increased (25.3%). ^{*2} The antibody-conjugated MMAE CL and AUC_{0-inf} are expected to be less accurate since the percent of extrapolated AUC_{0-inf} was increased (21.1%).

Furthermore, it was shown for the first time that hemizygous Tg276 mice are an appropriate model for ADCs to detect differences in the PK caused by different conjugation sites. However, the different PK determined for the ADCs with different conjugation sites and methods and the influence shown with respect to the mAb scaffold, emphasizes the need to develop and identify suitable *in vitro* methods that could indicate the PK of

ADCs. The pressing question of whether the different *in vitro* assay results of the ADCs shown in the previously sections indeed indicate the different ADC PK is addressed in the next section.

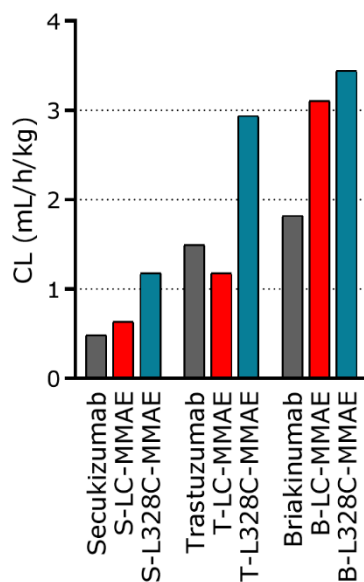


Figure 19. Comparison of the total antibody CL in huFcRn transgenic mice of ADCs conjugated at position L328C (blue) or C-terminally at the LCs (red) and corresponding native mAbs (gray). Except for trastuzumab (4.7 mg/kg), 3 mg/kg of mAb or ADC was administered intravenously to huFcRn transgenic mice.

7.1.7. Correlation of the *In Vitro* and *In Vivo* Results

Figure 20 illustrates the relationship between the different assay results and the clearance in hemizygous Tg276 mice. Already visually but also from the indicated Spearman's correlation coefficients, which were used to statistically evaluate the strength of each association, it becomes obvious that there are no correlations between the CL and HIC results, neither when using HIC rRTs nor HIC nRTs (**Figure 20, a and b**), CL and terminal stability results, Tm1 (**Figure 20, c**) and Tm2 (**Figure 20, d**), and CL and the huFcRn binding kinetics (**Figure 20, e**).

The importance of the interaction between Fc-containing molecules and FcRn for their PK is well-known.¹¹⁴ However, all study ADCs showed similar binding kinetics to huFcRn as measured by BLI (section 7.1.4). Therefore, a correlation between FcRn binding affinity and CL could not be expected suggesting that other physicochemical properties of the ADCs account for the differences in PK.

HIC and nanoDSF analysis were used to assess the hydrophobicity and thermal stability of the ADCs as it has been shown that in some cases the ADC PK correlated with HIC retention times and melting temperatures.^{35,114,171,176} For instance, for homogenous DAR 8 ADCs conjugated to different hydrophobic linker variants, a correlation between HIC retention times and PK results in mice and rats has been reported by Lyon *et al.*³⁵ However, later on, the same group demonstrated limitations for the HIC method as PK

predictor as they were not able to observe a correlation when ADCs with linkers bearing discrete PEG chains of varying length were used.¹³⁹ Furthermore, Tumej *et al.* demonstrated a weak correlation between HIC retention times and the total antibody exposure (AUC) in rats of six trastuzumab-VC-PAB-MMAE ADCs conjugated at different conjugation sites.¹⁷¹ In this study here, using CL data obtained in Tg276 mice, this observation could not be confirmed (CL = dose/AUC; the doses for the ADCs were the same).

With regard to conformational stability, results reported by Beckley *et al.* suggest that partial unfolding of the C_H2 domain, caused by conjugation involving the hinge region disulfides, is responsible for the formation of aggregates.¹⁷⁵ A strong propensity to aggregate, especially for ADCs with increased hydrophobicity mediated by high DARs, may negatively affect the PK.^{35,175} In line with that, for a set of ADCs conjugated with peptide tags in the C_H2 domain it was reported that reduced thermal stabilities caused by destabilization of the C_H2 domain indeed correlated with rapid clearance in mice.¹⁷⁶ However, as already mentioned, for the ADCs in this study an increased thermal instability of the C_H2 domain (see section 7.1.3) did not correlate with faster clearance in mice (**Figure 20, c**) or led to an increased propensity for aggregation during ADC generation. Nevertheless, it cannot be ruled out that the decrease in thermal stability might indicate a risk for further important developability factors like stress resistance, as for example, agitation or oxidative stress.¹⁷⁵

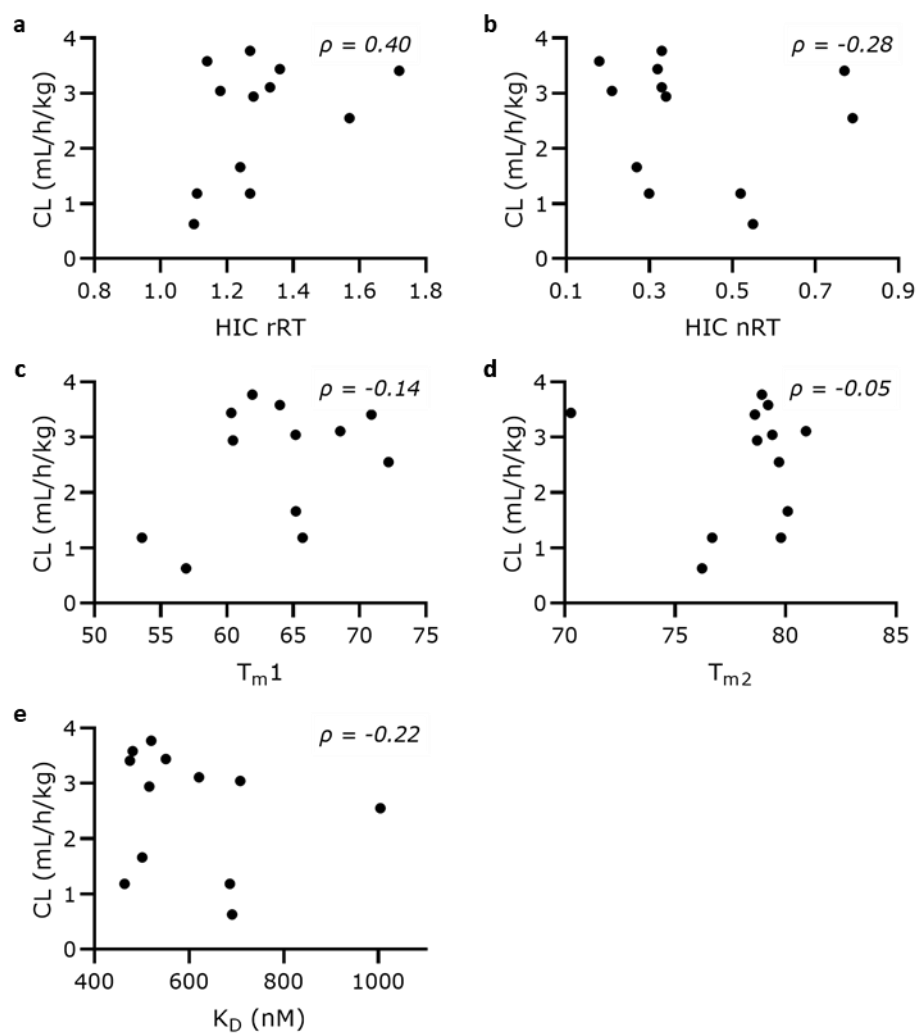


Figure 20. Relationship between the PK in huFcRn Tg276 mice and results in different *in vitro* assays. The total antibody CL value of each molecule is plotted against the results of each molecule in the following *in vitro* assays: HIC (HIC rRT, **a** and HIC nRT, **b**), nanoDSF (T_{m1} , **c** and T_{m2} , **d**), and binding affinity to huFcRn measured by BLI (K_D , **e**). No significant correlations ($p < 0.05$) could be found between the results and the CL as indicated by the Spearman correlation coefficient (ρ).

7.2. Establishment of Additional *In Vitro* Assays to Analyze ADC Physicochemical Properties for the Identification of ADCs with Risk for Poor Pharmacokinetics

7.2.1. Assay Selection and Test Molecules

In the previous section, it was shown that the hydrophobicity of the ADCs measured by HIC, the thermal stabilities measured by nanoDSF, and the huFcRn binding affinities analyzed by BLI did not correlated with the CL values obtained in Tg276 mice. Therefore, additional physicochemical property assays should be tested with a set of ADCs covering a higher variety of different ADC design features (compared to the previously used ADCs), which may allow to find a more robust correlation between the assay results and the CL. In this context, assays should allow screening of larger numbers of ADCs and fulfill some criteria. They should be sensitive, robust, and should require only limited amounts of ADCs as analyte. Furthermore, they should be suitable for the use in medium to high throughput and material costs should be rather low. Various assays were described in recent publications that fulfill these criteria and for which successful correlations of mAbs *in vitro* assay results with their PK were demonstrated. At this, assays were highlighted as suitable tools to identify mAbs with poor physicochemical properties and associated risk for poor PK (see section 4.3.2). To expand this test strategy also to ADCs, assays were selected and adapted to analyze the self-interaction and non-specific binding tendencies of ADCs. For self-interaction, the affinity-capture self-interaction nanoparticle spectrometry (AC-SINS) and a clone-self-interaction Bio-Layer Interferometry (CSI-BLI) assay were used. Non-specific binding was analyzed by a newly developed BLI-based method using polyspecificity reagent as substrate (PSR-BLI) and by two ELISA-based methods that measure non-specific binding to baculovirus particles (BVP) or heparin. Additionally, the huFcRn affinity chromatography was applied for evaluation of the ADC retention and peak profile upon elution at increasing pH and solvent exposed hydrophobicity was assessed by applying a spectroscopy method using bis-ANS (4,4'-dianilino-1,1'-binaphthyl-5,5'-disulfonate).

A set of 13 different ADCs was used for the establishment of the assays (named ADC1-ADC13) for that linear PK data in huFcRn transgenic mice (hemizygous Tg276, intravenous administrations with doses of 2 to 5 mg/kg) were available. As for all ADCs, except for ADC6 (the antibody-conjugated payload was cleared 2.3-times faster than the total antibody), pronounced stability was indicated by antibody-conjugated payload profiles (data not shown), the total antibody CL corresponds to the ADC CL. In case of ADC6, the total antibody CL could be affected by an increasing portion of unconjugated mAb over time which leads to an underestimation of the ADC CL value. Although just a small set of molecules was used, the clearance results showed a broad ranged from 1.18 to 8.38 mL/h/kg (**Figure 21**). This broad range of data is well in line with

CL ranges of previously published studies that were successfully used for mAbs for correlations of the *in vitro* physicochemical assay results with *in vivo* PK (CL).^{111,114,115,133,135}

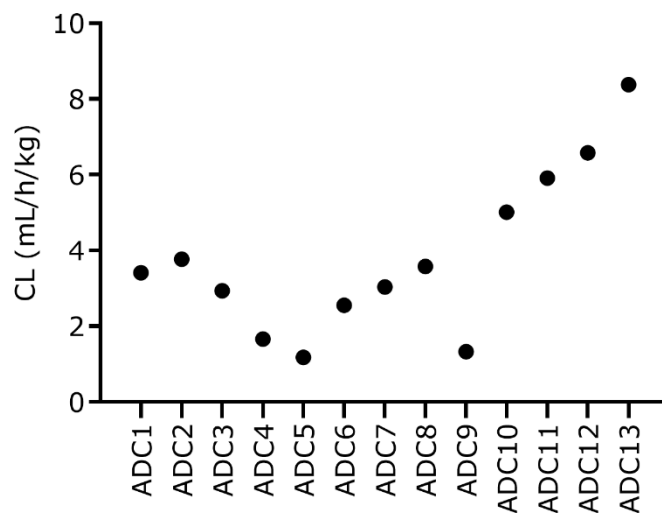


Figure 21. Total antibody clearance values of the different study ADCs (ADC1-ADC13) in huFcRn transgenic mice (hemizygous Tg276). ADCs were given as single intravenous dose at 2.0 mg/kg, 3.0 mg/kg, or 5.0 mg/kg.

The selected ADCs included in this study were based on different mAb scaffolds targeting distinct tumor associated antigens (TAA). All mAbs were conjugated with the same linker-payload (VC-PAB-MMAE) only differing in a maleimidocaproyl handle for cysteine conjugation (MC-VC-PAB-MMAE) or a triple glycine handle for mTG conjugation (G₃-VC-PAB-MMAE). As described in 7.1, different conjugation sites were targeted using mTG and engineered cysteine coupling techniques. Additionally, conjugation to interchain cysteines by partial reduction technique was used for ADC generation. The ADC design features and product characteristics are summarized in **Table 7**.

Table 7. Overview of the ADC design features and product characteristics of the 13 study ADCs.

Target	Conjugation method	Conjugation site	Linker	Payload	DAR range	% purity
EGFR	mTG	S239C	G ₃ -VC-PAB	MMAE	2-4	99.1 -100
HER2	Partial reduction	D265C	MC-VC-PAB			
MUC1	Engineered cysteine conjugation	Q295				
ROR1		N325C				
TAA		L328C				
		S442C				
		HC C-terminal				
		LC C-terminal				
		Interchain cysteines				

Furthermore, different assay control molecules were included. In all assays, except of BVP and heparin ELISA, unconjugated trastuzumab and briakinumab were used as negative and positive controls, respectively. In the following, the rationale for briakinumab as positive control is outlined in more detail: Briakinumab showed elevated CL in huFcRn transgenic mice (see section 7.1.6). Furthermore, several reports about briakinumab and its clinical competitor ustekinumab are available. In contrast to briakinumab, ustekinumab showed a good PK behavior (half-life in humans 21 days vs. 8 days)¹⁸⁸ although both antibodies bear only little differences in their constant domains related to some allotype-specific amino acids and mostly differ in their variable region.¹²⁴ To identify the reasons for the tremendous difference in half-life, several studies were performed by different groups. These studies could show that ustekinumab had good physicochemical properties whereas briakinumab showed a high self-interaction tendency (AC-SINS),^{123,189} pronounced non-specific binding (BVP-ELISA, binding to heparin, Hsp70 and Hsp90 measured by mammalian display, cross-interaction chromatography),^{123,189,190} and a slowed dissociation from huFcRn (huFcRn affinity chromatography)¹²⁴. Overall, the authors suggested that the unfavorable physicochemical properties of briakinumab can be attributed to a positive charge patch within its variable domain.^{124,190} Therefore, the reported unfavorable physicochemical properties along with fast clearance qualified briakinumab as a positive control for the assays.

Only for the heparin and BVP ELISA a trastuzumab-ADC (T-LC-MMAF, DAR 1.74) was used as negative control. At this, T-LC-MMAF was generated using the non-cleavable linker-payload G₃-MMAF and enzymatic conjugation via Sortase A (SrtA) to trastuzumab bearing a C-terminal SrtA tag ((G₄S)₃LPETGS) at the LCs

(section 6.17.5). Another trastuzumab-ADC (T-HC-VC-PAB-MMAF, DAR 1.78) was used as positive control for both ELISA-based methods. To generate this ADC, G₃-VC-PAB-MMAF was conjugated via mTG to trastuzumab bearing a C-terminal mTG tag (LLQGA) at the HCs (section 6.17.3).

In the following, the results of the 13 ADCs in every established *in vitro* assay will be described in detail (sections 7.2.2, 7.2.3, 7.2.4, and 7.2.5), followed by a comparison of the different assays (section 7.2.6) and finally, the correlations between the assay results and the CL values will be presented (section 7.2.7).

7.2.2. Evaluation of the Self-Interaction Properties of ADCs

Reduced self-interaction was described as an important factor for mAbs with good PK properties (see section 4.3.2).^{111,119,136} In various reports, the two different assays AC-SINS and CSI-BLI were described to reveal the tendency of mAbs to self-interact.^{111,123,191} Therefore, both assays were used along with the 13 study ADCs.

Affinity-Capture Self-Interaction Nanoparticle Spectroscopy

For mAbs a correlation between AC-SINS scores and *in vivo* PK data was shown.¹¹¹ In addition, so far, AC-SINS data have been the only mAb specific *in vitro* data used for a physiologically-based PK model to predict mAb PK developed by Jones *et al.*¹⁹² Because of these reports, the AC-SINS assay was selected as screening assay for ADCs although Tumey *et al.* found no correlation between the AC-SINS score and the clearance in rat for trastuzumab-VC-PAB-MMAE ADCs conjugated at different conjugation sites.¹⁷¹

For ADCs the same experimental setup as for mAbs can be used. Therefore, the AC-SINS assay was performed as reported by Liu *et al.*¹³⁷ In brief, ADCs or control mAbs were captured on gold-nanoparticles that were previously coated with an anti-human Fc antibody (section 6.32). Self-interaction between the captured molecules led to a clustering of the particles which resulted in an increase in plasmon wavelength. The recorded absorption spectra (450 - 650 nm) are exemplarily shown for three of the ADCs in comparison to assay buffer DPBS in **Figure 22, a**. Here, ADC7 showed a spectrum comparable to DPBS with a wavelength of maximum absorbance (λ_{max}) of 532.6 nm indicating low self-association and ADC9 showed a slight increase in λ_{max} (534.4 nm). In contrast, ADC13 showed elevated λ_{max} of 546.8 nm indicating pronounced self-association. The data obtained for all study ADCs were further processed in a normalization step where λ_{max} of the samples was normalized to λ_{max} of a DPBS control analyzed in the same experiment (section 6.32). Resulting AC-SINS scores of all 13 ADCs ranged from -0.1 to 15.3, whereas high scores indicate pronounced self-interaction (**Figure 22, b**). The highest scores for ADCs were measured for the ADC11-ADC13 (11.0-15.3), whereas all other ADCs showed much lower scores (-0.1-1.3). Within the panel of ADCs with low scorings (ADC1-ADC10) only minor differences were observed. Herein, ADC9 (1.3 ± 0.4) and ADC10 (1.0 ± 0.1) showed

elevated scores compared to the other ADCs (-0.1-0.7). Furthermore, ADC1, ADC2, and ADC6 showed slightly higher scores (0.35-0.7) compared to ADC3-ADC5, ADC7, and ADC8 (-0.1-0.1). The overall highest AC-SINS score (23.6 ± 1.6) was measured for the positive control mAb, briakinumab.

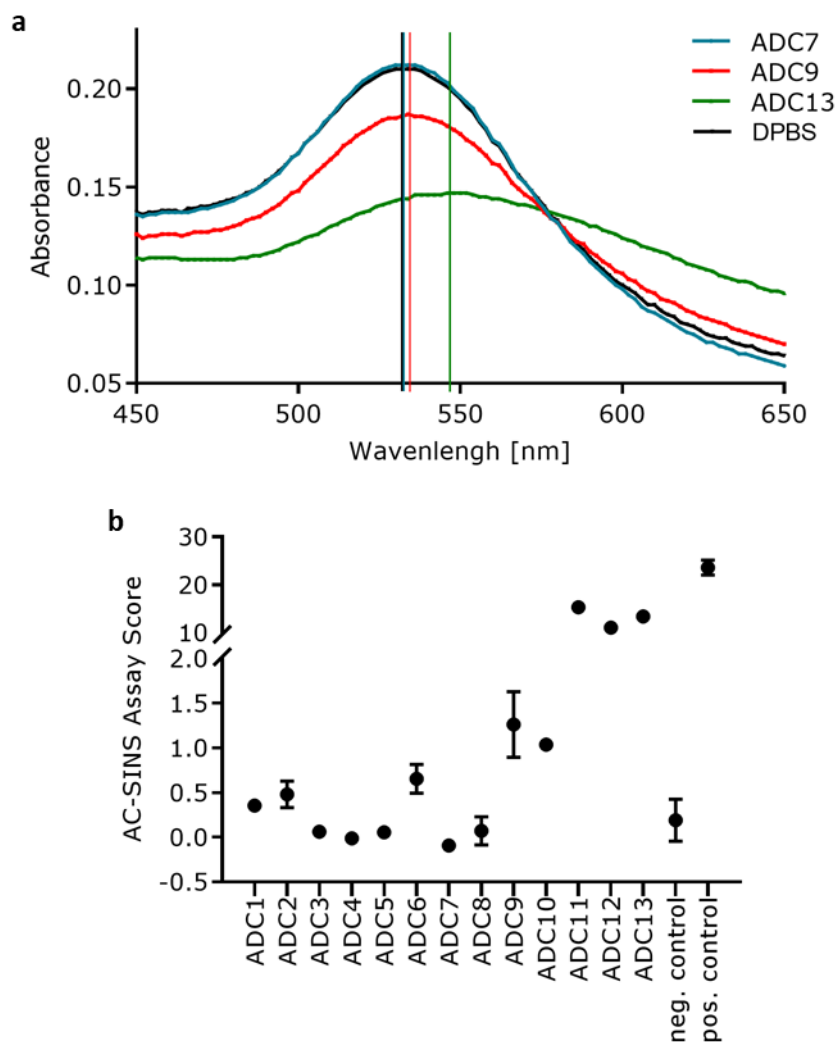


Figure 22. Analysis of the self-interaction tendencies of ADCs by AC-SINS. a) Exemplarily AC-SINS assay measurement of the DPBS control (black) compared to three ADCs (blue ADC7, red ADC9, and green ADC13) representing the whole recorded absorption spectrum (450 - 650 nm) and the wavelength of maximum absorbance (λ_{max}) marked by the respective colored line. b) Calculated final AC-SINS scores of all study ADCs and control mAbs that were analyzed at least in duplicates. Error bars represent SD.

Clone Self-Interaction Bio-Layer Interferometry

CSI-BLI was reported by Sun *et al.* as method to identify mAbs with high self-interaction.¹⁹³ In brief, in this study here, ADCs were captured on anti-human Fc capture (AHC) biosensors before they were incubated with the same analyte at high concentration that stimulates self-interaction. Triggered self-interaction was indicated by change of interference (section 6.30.2). In **Figure 23** the data processing is illustrated exemplarily: In **Figure 23, a** exemplarily raw data of a measurement is shown (ADC1 and ADC7), while in **Figure 23, b** sensorgrams are shown after normalization step, where the sensorgrams are aligned to the baseline before data analyses can be done. This was done to calculate the response at the end of the association step, which was then used to calculate the normalized response (for further information see section 6.30.2). The final CSI-BLI scores, shown in **Figure 23, c**, are normalized to the CSI-BLI score of the negative control trastuzumab to minimize potential differences in the measurement caused for example, by different biosensor charges. Similar to the AC-SINS method, the CSI-BLI measurement resulted in a broad range of scores, ranging from 0.09 to 0.60. Again, higher values indicate more pronounced self-interaction. Highest self-association scores (0.56-0.60) were determined for ADC11-ADC13, followed by ADC1, ADC2, ADC6, ADC9, and ADC10 with scores from 0.22 to 0.41 and finally ADC3–ADC5, ADC7, and ADC8 with scores lower than 0.20.

In conclusion, for each self-interaction assay a similar trend has been demonstrated for all ADC variants: ADC11-ADC13 with high scores, ADC3-ADC5, ADC7, and ADC8 with low scores and all other ADCs with intermediate scores. In contrast to AC-SINS, the CSI-BLI method seems to be more sensitive for ADCs than for mAbs since most of the ADCs showed a comparable or higher CSI-BLI score than the positive control mAb (CSI-BLI score of 0.18 ± 0.04). Furthermore, the CSI-BLI assay seems to have a better resolution, but the measurements are overall less precise compared to the AC-SINS measurements (**Figure 22, c** vs. **Figure 23, b**). Regarding to the required ADC material, a single CSI-BLI measurement (35 μ g ADC) requires 7-times the material required for one AC-SINS measurement (5 μ g). Even though 35 μ g per run are still acceptable, the assay setup allows for an increased throughput and reduced material consumption when transferring from 96- to 384-well plates. This would make both assays more comparable with respect to throughput and material consumption. The miniaturization and further optimization of CSI-BLI was not part of this work but should be feasible without complications.

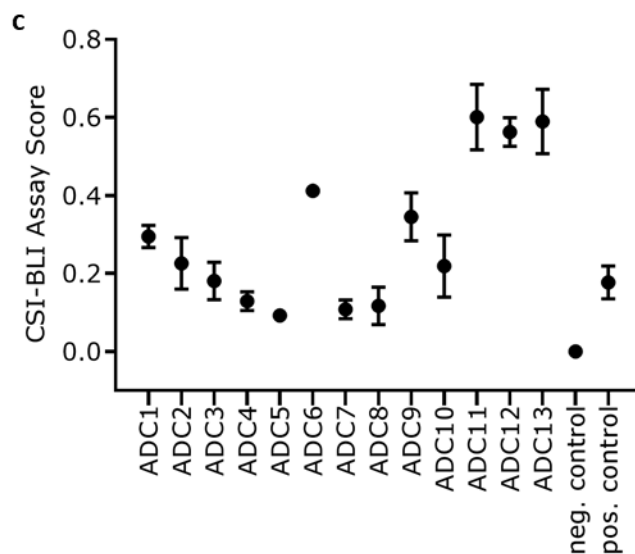
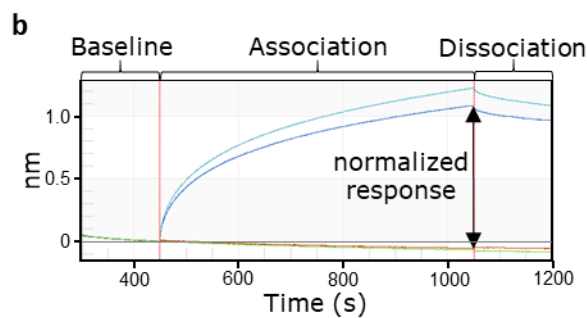
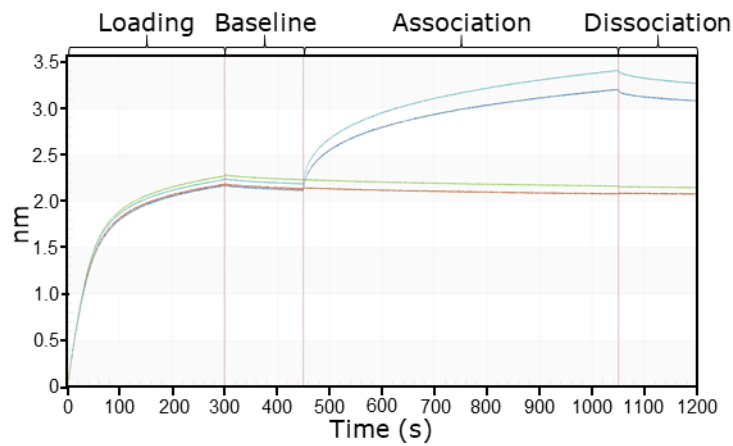


Figure 23. Results of the CSI-BLI assay. a) Exemplarily raw data of the CSI-BLI assay with all assay steps: First AHC biosensors were loaded for 300 s with 10 $\mu\text{g}/\text{mL}$ ADC, here ADC1 (green and light blue) and ADC7 (red and dark blue), then incubated for 150 s in DPBS (baseline), followed by the association step for 600 s, either in DPBS as reference measurement (green and red) or in 150 $\mu\text{g}/\text{mL}$ of the same ADC as used for the loading step (light and dark blue). The final dissociation step (150 s in DPBS) was performed to detect possible fast dissociation which could indicate that the self-interaction is not stable. b) Shown is the same data aligned to the baseline step to calculate the responses (nm shift in the interference pattern) at the end of the association step. The difference between the response of the biosensor loaded with ADC and the corresponding reference measurement (normalized response) was further normalized to the normalized response of the negative control to calculate the final CSI-BLI assay score of the ADCs (c). Samples were analyzed at least in duplicates. Error bars represent SD.

7.2.3. Investigation of Non-Specific Binding of ADCs

Non-specific binding properties of the study ADCs were first analyzed by ELISA-based methods that have been shown to be suitable to identify mAbs with risk for poor PK: ELISA-methods in that BVP or heparin were immobilized on plates.^{115,116,121} In contrast to mAbs, ADCs show an even greater non-specific binding for example, to plate surfaces, presumably due to hydrophobic linker-payloads. Therefore, the major challenge to enable the use of these assays for ADCs was to identify a blocking and assay buffer that allows for appropriate blocking of non-specific binding to the plate surface but still allows non-specific binding to the substrate. Testing of several available and known blocking solutions showed that best results were achieved when 3% (w/v) BSA was used (data not shown). For a detailed description of both methods see section 6.33 and 6.34. While heparin is a highly sulfated, negatively charged glycosaminoglycan, BVP is a complex mixture containing different substrates like glycoproteins, extracellular matrix, carbohydrates, viral capsid, and parts of the insect cell that allows for non-specific binding caused by different kind of interaction.^{121,194} A specific binding is highly unlikely in this assay setup because the assay matrices lack target structures for therapeutic ADCs.¹²¹ Because of the higher complexity of the BVP substrate the results of this ELISA were normalized to the results of the positive control measured in the same experiment to minimize variations between individual experiments and different substrate batches (section 6.33). **Figure 24** illustrates the assay results from the analyzed study ADCs that were found with both assays. Here, different non-specific binding behavior profiles were found for the study ADCs. The results of the ELISA measurement are exemplarily shown for three of the study ADCs, ADC13, ADC1, and ADC4, in **Figure 24, a** (BVP ELISA) and **b** (heparin ELISA). Of these tested ADCs, ADC13 showed the highest signals at each ADC concentration and reached the signal plateau already at low ADC concentrations indicating a high non-specific binding in both assays. ADC1 showed a reduced non-specific binding compared to ADC13 and for ADC4 only at the two highest ADC concentrations a signal was measured indicating only a minimal non-specific binding. Additionally, the final calculated BVP (**Figure 24, c**) and heparin assay scores (**Figure 24, d**) of all study ADCs are shown. Each score summarizes the different measurements of an ADC that were performed at different analyte concentrations in one value. As already mentioned, an additional normalization step was performed for the BVP results to calculate the scores (see section 6.33). Again, both assays showed a broad range of scores for the study ADCs, from -26 to 16 for the BVP ELISA and from 2 to 56 for the heparin ELISA, at which high scores indicate non-specific binding. Although the results of both ELISA methods slightly differ, for example, when comparing the ranking of the results of ADC1, ADC6, and ADC9 in both assays, the overall trend is quite similar meaning ADCs that had a high score in one assay had also a high score in the other assay and the same is true for low scoring ADCs. Since two different substrates were used, it is not surprising that the ranking of the ADCs according to their results in both tests is not the same. Overall, for both ELISA methods low scores were analyzed for ADC2-

ADC5, ADC7, and ADC8 (BVP ELISA score range: -26 to -13; heparin ELISA score range: 2 to 8) and high scores that were greater than or equal to the score of the positive control (BVP ELISA score: 0; heparin ELISA score: 15) were analyzed for ADC1, ADC6, and ADC9-ADC13 (BVP ELISA score range: 0 to 16; heparin ELISA score range: 31 to 56).

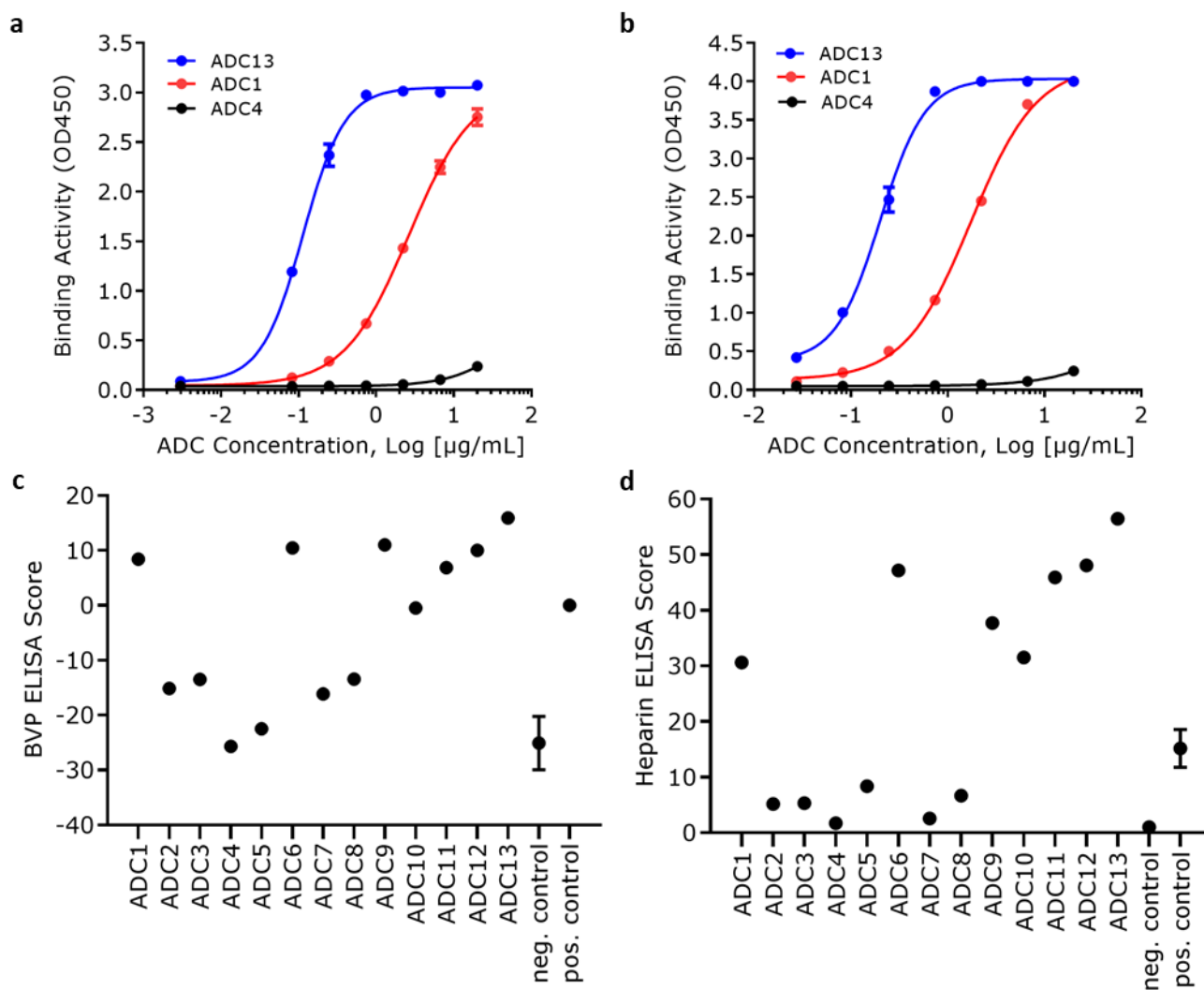


Figure 24. Results of the BVP and heparin ELISA measurement to analyze non-specific binding of the ADCs. Exemplarily results of the measurement (mean OD450) of the different ADC concentrations shown for ADC13 (blue), ADC1 (red), and ADC4 (black), of the BVP (a) and heparin ELISA (b). Each ADC concentration was analyzed in quadruplicates in the BVP and in triplicates in the heparin ELISA. (c) and (d) Final assay scores of the BVP and heparin ELISA, respectively, that were calculated for all study and control ADCs. Control ADCs were analyzed at least in duplicates. Error bars represent SD.

In addition to the ELISA-based method, an assay was developed to analyze non-specific binding based on an orthogonal readout. Xu *et al.* successfully showed that soluble membrane proteins of mammalian cells (named polyspecificity reagent, PSR) could be used during yeast surface display-guided screening of

antibodies as a counter-selection substrate for the fluorescence-activated cell sorting.¹³⁴ Based on the work performed by Xu *et al.*, PSR seemed to be also a suitable matrix to analyze non-specific binding interactions. Inspired by the CSI-BLI assay (section 7.2.2 and 6.30.2), a BLI-based assay was developed where PSR was used as soluble matrix.

BLI allows for sensitive, fast, and high-throughput measurements and real-time monitoring of all steps, which is not true for ELISA methods. Furthermore, this method requires only minor amounts of ADC (4 µg per measurement in a 96-well format), which is another advantage for BLI compared to ELISA-based methods (material consumption is 11 µg for heparin ELISA and 26 µg for BVP ELISA). As PSR displays soluble membrane proteins of CHO and HEK cells, analysis of the non-specific binding tendencies of antibodies/ADCs against targets expressed on HEK cell surface is not possible with this assay. In the following the PSR-BLI method is described briefly.

ADCs were first captured on AHC biosensors, followed by a blocking step with BSA before the interaction with PSR was measured. In every experiment and on every plate, a measurement with biosensors that were not loaded with PSR was performed in DPBS (reference biosensors). In **Figure 25** the data processing is illustrated exemplarily: In **Figure 25, a** exemplarily raw data of a PSR-BLI measurement is shown (of ADC4, ADC6, ADC9, and the reference biosensors), while in **Figure 25, b** sensorgrams are shown after normalization step, where the sensorgrams are aligned to the baseline before data analyses can be done. This was done to calculate the response at the end of the association step, which was then used to calculate the normalized response (for further information see section 6.30.3). Considering the dark blue line in **Figure 25, b** (to which the upper arrow of 'normalized response' points) a great signal can be seen for the reference biosensor. However, this response is not caused by a great non-specific binding of PSR to the biosensors but caused by the change of buffer resulting in a fast increase of the signal. While the baseline is recorded in DPBS, the buffer of the association step consists of DPBS mixed with the storage buffer of PSR (a mixture of PSR buffer A and B, section 6.8 and section 6.30.3). When performing the baseline and dissociation step in DPBS containing the PSR buffer A and B in the same concentration as in the association step no changes in the interference were detected (data not shown). Since the buffers for the PSR preparation are complex, rather expensive, and long-time storage could be problematic, the strong signal increase from baseline to association and decrease from association to dissociation was accepted. Furthermore, the PSR-buffer concentration in every experiment could vary minimally and vary with different PSR batches which could influence the signal increase. Hence, the strong signal increase was excluded by normalizing all results to the reference biosensor.

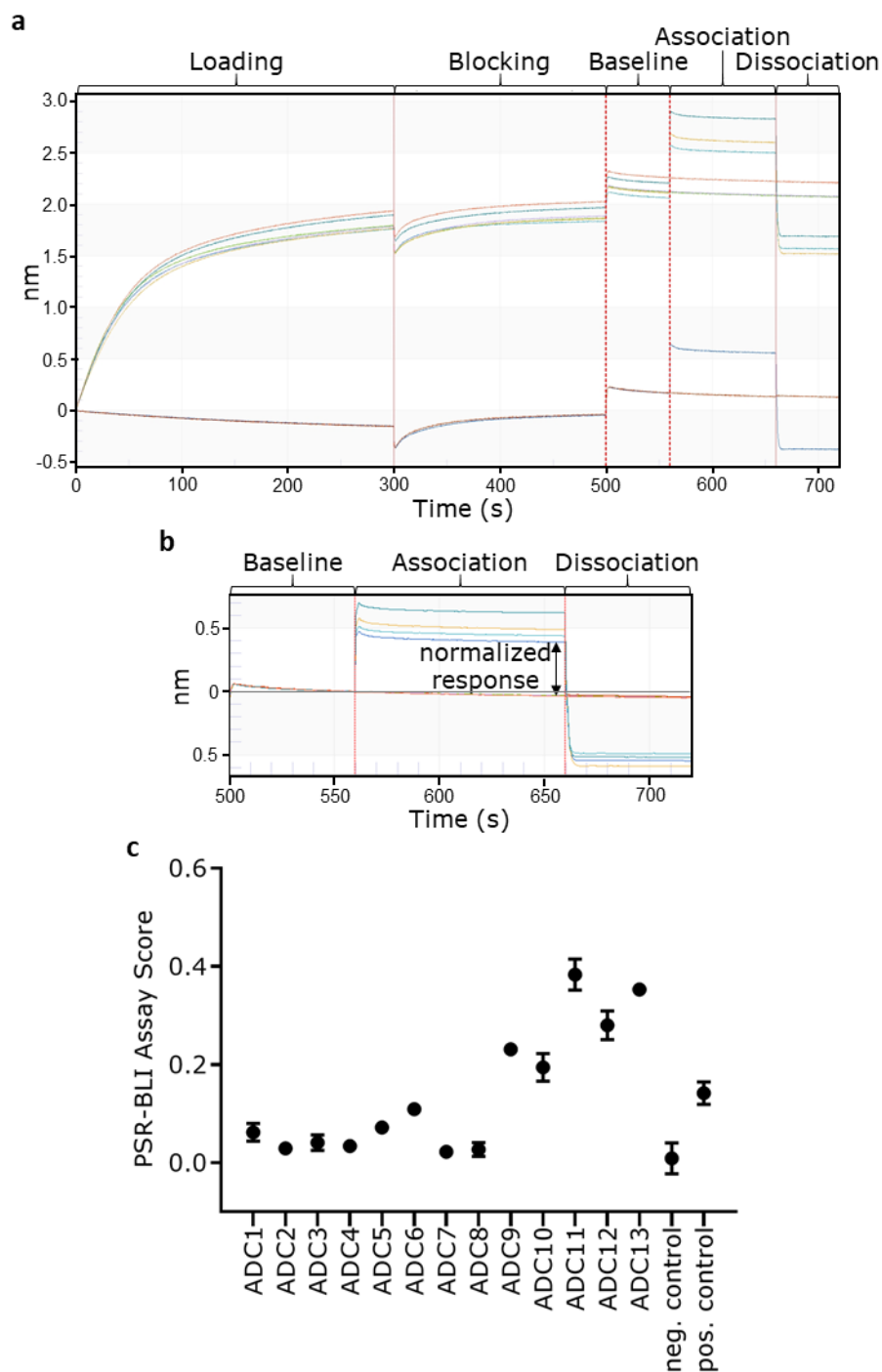


Figure 25. Results of the PSR-BLI assay. **a**) Exemplarily raw data of the PSR-BLI assay: First AHC biosensors were loaded for 300 s with 10 $\mu\text{g}/\text{mL}$ ADC, here ADC 4 (light blue and green), ADC 6 (yellow and purple), and ADC 9 (turquoise and dark orange), or incubated in DPBS (reference biosensor, dark blue and brown). Then, biosensors were incubated for 200 s in DPBS with 1% (w/v) BSA (blocking), incubated for 60 s in DPBS (baseline), and for 100 s (association) either in DPBS as reference measurement (green, purple, dark orange, brown) or in 20 $\mu\text{g}/\text{mL}$ PSR (light blue, yellow, turquoise and dark blue). Finally, a dissociation step (60 s in DPBS) was performed to detect possible obvious differences in the dissociation. **b**) Shown are the data aligned to the baseline to calculate the responses at the end of the association step. The difference between the response of the biosensor loaded with ADC and the corresponding reference measurement (normalized response) was further normalized to the normalized response of the reference biosensor (PSR-BLI assay score, **c**). Samples were analyzed at least in duplicates. Error bars represent SD.

The results obtained from the PSR-BLI assay using the control mAbs indicate a broad assay signal range with a 16-fold elevated signal for the positive control briakinumab (PSR-BLI assay score of 0.142 ± 0.023) compared to the negative control trastuzumab (0.009 ± 0.032 , **Figure 25, c**). Of the study ADCs, various ADCs (ADC1–ADC8) showed scores below the positive control (0.022 – 0.109) indicating only a low non-specific binding, while ADC9–ADC13 showed higher PSR assay scores than the positive control (0.194 – 0.383). The results of the ADCs with a high score, ADC9–ADC13, are in agreement with the high scores obtained for these ADCs by the ELISA-based methods (**Figure 24, c and d**). However, ADC1 and ADC6 that showed high scores in the ELISA-based assays, showed only relative reduced scores in the PSR-BLI assay when compared to the positive control (0.062 ± 0.018 and 0.109 ± 0.011 , respectively).

7.2.4. Hydrophobicity of ADCs Analyzed by Bis-ANS

As previously described in section 7.1.2, HIC is often used to analyze the hydrophobicity of ADCs as increased hydrophobicity of ADCs has been shown to be associated with increased clearance.^{35,36,97} However, this method has led to contrary findings in different reports with regard to the suitability of the method as screening tool to identify ADCs with risk for poor PK (see section 4.3.2 and section 7.1.7).^{35,139,171} Therefore, HIC is not considered as generic screening method for different kind of ADCs including ADCs with PEGylated linker-payloads¹³⁹ or ADCs with identical linker-payload and DAR that are conjugated at different sites of the mAb (section 7.1.7). Another method that is widely used to characterize the hydrophobicity of biotherapeutics is known under the name “bis-ANS”.^{170,195,196} The fluorescence dye bis-ANS is a dimeric analog derived from 8-anilino-naphthalene-8-sulfonate (ANS). Hydrophobic interactions with this dye leading to an increase of its fluorescence signals.¹⁷⁰ Interestingly, both methods, HIC and bis-ANS, significantly differ in the indicated hydrophobicity which was shown for a set of different trastuzumab-VC-PAB-MMAE ADCs by Benjamin *et al.*¹⁹⁶ One possible explanation that has been given is that for HIC only accessible nonpolar regions and residues on the protein are believed to interact with the stationary phase, whereas for bis-ANS sterically hidden hydrophobic residues might be accessible as well.¹⁹⁶

The bis-ANS assay is characterized by its simple procedure, low costs, medium throughput, and robustness. For this assay 40 μg of ADC are required for one measurement (96-well format, detailed method see section 6.31). However, the analyte amount is only a minor disadvantage compared to the other methods already mentioned, since reducing the amount of ADC and additionally increasing the throughput by switching to a 384-well format should be straightforward but was outside of the scope of this work.

In **Figure 26, a**, the measured fluorescence intensity spectra of the DPBS control (gray line) compared to three study ADCs (black, red, and blue line) are exemplarily shown. When bis-ANS was incubated with DPBS only a minimal background increase in the fluorescence signal was analyzed, whereas elevated fluorescence

intensities were measured during co-incubation with the ADCs. This increase in fluorescence is in line with the pronounced hydrophobicity of the VC-PAB-MMAE linker-payload utilized for conjugation.^{35,197} Although all measured ADCs were conjugated to this linker-payload and hence strong increase in signals compared to the DPBS control were obtained, great differences in the bis-ANS assay scores (599-2622) between ADCs were determined (**Figure 26, b**). The bis-ANS score represents the difference in fluorescence intensity between the ADC and the DPBS control at 511 nm. A higher score indicates a higher hydrophobicity. As expected, the negative control mAb scored 123 ± 13 , whereas the positive control mAb scored 11-fold higher (1406 ± 133). Although conjugated with the hydrophobic linker-payload, ADC1-ADC9 exhibited bis-ANS assay scores lower than the positive control mAb, ranging from 599 to 1337. Moreover, ADC5-ADC9 showed slightly increased scores (997-1337) compared to ADC1-ADC4 (599-739). Consistent with signal profiles from other assays, the highest scores were found for ADC11-ADC13 (2203–2622) followed by ADC10 (1818 ± 74). One main driver of apparent ADC hydrophobicity typically arises from the hydrophobic conjugated payload constructs but as all study ADCs carried the same linker-payload, differences between the ADCs may derive from additional factors such as DAR.^{35,36} In this study, ADC1–ADC8 had a DAR of 2, while ADC9–ADC13 had a DAR of 4. In line with expectations, the DAR 4 ADCs showed the highest scores in the bis-ANS assay. However, even all scores of DAR 4 ADCs were high, a broad range of scores were indicated for these ADCs (1337-2622). For example, the DAR 4 ADC9 showed a 2.0-fold lower score than the DAR 4 ADC13 (2622 ± 63) and a 1.4-fold lower than the DAR 4 ADC10 (1818 ± 74). This shows that even ADCs with identical DAR and linker-payload differed in hydrophobicity analyzed by bis-ANS indicating that other design features, for example, the antibody scaffold and conjugation sites, seem to have an impact on the hydrophobicity as well. One example that supports this assumption is the difference in hydrophobicity observed for ADC9 and ADC10 as these ADCs differed only in the mAb scaffold. An example for ADCs where only the conjugation sites differed but a significant difference in the bis-ANS scores was analyzed, are ADC1 (score of 599 ± 54) and ADC8 (score of 1225 ± 48).

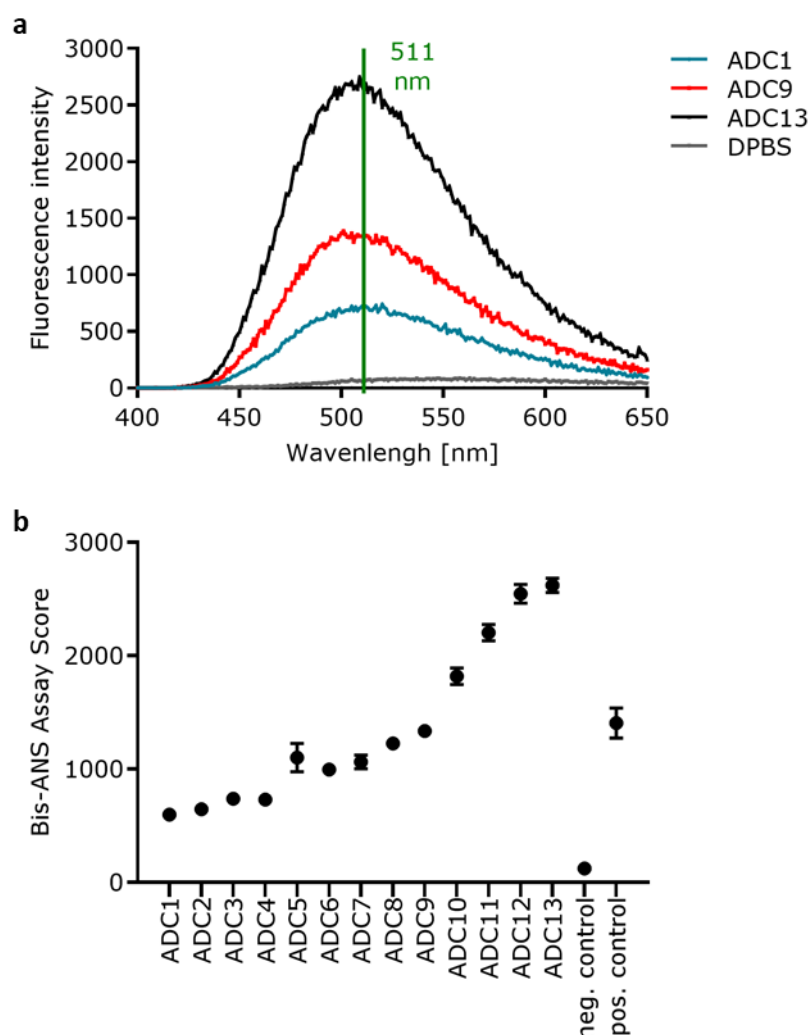


Figure 26. Hydrophobicity of ADCs analyzed by bis-ANS assay. a) Exemplary bis-ANS assay measurement of the DPBS control (gray) is shown and compared to three study ADCs (blue ADC1, red ADC9, and black ADC13) representing the broad range of recorded fluorescence spectrum (400 - 650 nm). b) Calculated final bis-ANS scores of all study ADCs and control mAbs that were analyzed at least in duplicates. Error bars represent SD.

7.2.5. huFcRn Affinity Chromatography

As already described, the pH-dependent interaction of ADCs with FcRn allows to rescue ADCs from lysosomal degradation after unspecific uptake into cells. Accordingly, it is well documented that differences in the binding kinetics with FcRn can significantly affect the PK of mAbs (see section 4.3.1).¹¹⁴ During the first attempts in this study, to evaluate FcRn binding as critical component for the PK of the 12 study ADCs, the affinity to huFcRn at pH 6.0 was measured by BLI. However, no correlations with the mouse PK data of ADCs conjugated at different conjugation sites (section 7.1.7) could be demonstrated indicating that differences in binding kinetics at pH 6.0 did not seem to play a role for the ADC series used in this study. In this regard, a novel affinity chromatography method was recently published that also relies on the FcRn interaction and

was successfully used for correlation of mAb elution profiles with PK CL values.^{111,124,132} More in detail, the huFcRn affinity chromatography was first reported by Schlothauer *et al.* as a method to characterize the interaction with huFcRn under conditions mimicking physiological conditions with respect to pH.¹³² Notably, the method requires a relatively long analysis time (104 min per sample) which limits the applicability of the method in high throughput.

In brief, mAbs or ADCs are applied to the column packed with huFcRn where they can bind to the immobilize huFcRn at acid pH before a linear gradient towards pH 8.8 is applied for elution (for detailed method see section 6.29). In this regard, not only functional pH-dependent FcRn binding but also general stickiness at increased pH values may contribute to the elution profiles. Since it was reported that the elution at pH levels above physiological pH (longer retention on the column) as well as slower-than-normal dissociation (broader elution profile) indicated poor PK, the retention time (RT, at maximum peak high) and the peak width at 50% peak high (PW) of the analytes were recorded.^{111,124} Both parameters were normalized to the negative control to reduce the effects of different column and buffer batches and were reported as relative retention time (rRT) and relative peak width (rPW). An overlay of exemplarily chromatograms from the huFcRn affinity chromatography is shown in **Figure 27, a**, whereas in **Figure 27, b** and **c**, the calculated mean rPWs and rRTs of all study ADCs and control molecules are shown. Here, the rPW ranged from 0.0 to 1.5 min (**Figure 27, b**) and the rRT from -0.9 to 4.9 min (**Figure 27, c**). The highest values were measured for the positive control mAb, with rRT of 4.9 ± 0.3 min and rPW of 1.5 ± 0.4 min. Within the panel of test ADCs, most elevated rPWs of 0.7-1.1 min were measured for ADC11-ADC13, whereas ADC1-ADC10 showed only minor rPWs of up to 0.4 min. The difference between the rRTs of ADC11-ADC13 and the other ADCs was less pronounced. However, the longest rRTs were found for ADC11-ADC13 (0.8-1.5 min). Interestingly, ADC1 showed a comparable high rRT of 1.1 ± 0.1 min even though a low value for rPW (0.1 ± 0.1 min) did not indicate strong interaction with the FcRn matrix. The ADC2-ADC4 and ADC7-ADC9 showed rRTs (-0.9-0.0 min) similar or even lower than the negative control (0 min) and ADC5, ADC6, and ADC10 showed slightly elevated rRTs (0.2-0.5 min).

High standard deviations for ADC11 and the positive control rRTs (**Figure 27, b**) were observed that could be related to the use of new column material, although normalization of the samples to the frequently measured negative control mathematically minimizes this effect. This indicated that the column performance is altered continuously with the number of runs, leading to a reduction in RT and PW of the samples, presumably due to the loss of functional huFcRn. To keep assay variability to a minimum, the column performance should be monitored by frequent measurements of controls and the column should be replaced when a rise in the variability can be observed (for example, if the rPW of positive control is only ~40% of the rPW that was determined at the beginning when the same column was new).

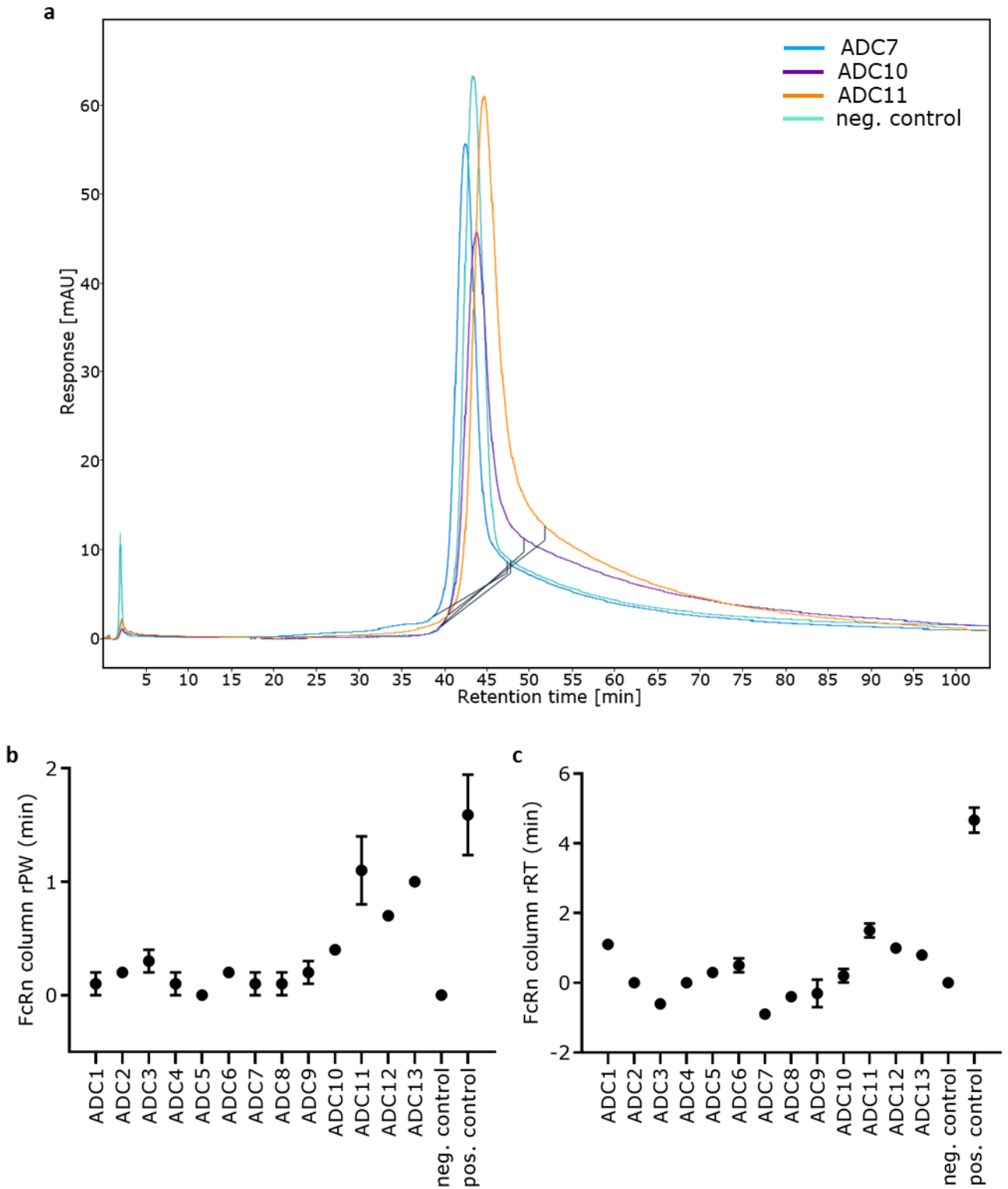


Figure 27. huFcRn affinity chromatography results of ADCs and control mAbs. a) Overlay of exemplary huFcRn column chromatograms of the negative control mAb (turquoise) and three study ADCs (blue ADC7, purple ADC10, and orange ADC11). **b** and **c**) Calculated huFcRn column relative peak width (rPW, **b**) and relative retention time (rRT, **c**) of all study ADCs and control mAbs. Mean of at least two independent measurements. Error bars represent SD.

In the next section, a systematic comparison between the different assay performances will be presented to investigate to which degree the results of the different assays match.

7.2.6. Comparison of Different *In Vitro* Assays

Although the assays have already been clustered according to the analyzed physicochemical property as it was described in the literature, these properties cannot be clearly separated as, for example, hydrophobic interactions also contribute to non-specific binding. To analyze if this clustering can be confirmed and to analyze whether some of the assays may be redundant due to the similarity of assay readouts, a systematic pairwise comparison of the results of the ADCs in the different physicochemical assays was performed using Spearman's rank correlation.

The same statistical analysis was applied to a set of different physicochemical assays that were established as screening cascade for mAbs by Avery *et al.* (see also section 4.3.2).¹¹¹ In this report, they were able to show a high correlation ($\rho > 0.90$) between the assays used for non-specific binding (DNA and Insulin ELISA) and between the different parameters of the huFcRn affinity chromatography results (rRT and PW). Between the huFcRn column parameters and the non-specific binding assays a modest to good correlation was found ($\rho = 0.64$ and 0.83). Furthermore, they employed the AC-SINS assay for detection of self-interaction and found only modest correlation with the FcRn column PW and rRT ($\rho = 0.62$ and 0.58 , respectively) and even lower correlation with the non-specific binding assays (highest $\rho = 0.49$). This led to the assumption, that distinct physicochemical properties are captured just by the AC-SINS assay but not by the other assay formats.¹¹¹

In contrast to Avery *et al.* who analyzed a total number of 42 mAbs with the different assays, only a small set of 13 ADCs were analyzed in this study for a first proof of the assay suitability.¹¹¹ Although the small ADC number limits statistical analysis of the assay comparison, the intention was still reasonable to get a first indication to which degree the results of the different assays match. The results of the Spearman's rank correlation for pairwise comparison of the *in vitro* assay data of the 13 study ADCs is shown in **Figure 28**. The scores of the CSI-BLI and AC-SINS assay highly correlated with each other ($\rho = 0.91$), which was expected since both assays are used to measure self-interaction of molecules. The three assays used to measure non-specific binding, namely PSR-BLI, BVP, and Heparin ELISA, showed a good correlation with each other (ρ range = 0.70 – 0.89). Because different substrates were used for the assays to analyze non-specific binding and thus different types of non-covalent interaction may be pronounced differently, a perfect correlation was not expected. Furthermore, the non-specific binding assays showed good correlation with both self-interaction assays (CSI-BLI and AC-SINS; ρ range = 0.80 – 0.81). This is in contrast to the finding by Avery *et al.*, where the AC-SINS assay results did not significantly correlate with the non-specific binding assays.¹¹¹ In

contrast to the work presented here, Avery *et al.* used a different set of non-specific binding assays (DNA ELISA and Insulin ELISA) and also mAbs instead of ADCs.¹¹¹ Another obvious difference compared to the analyses reported by Avery *et al.* is that the two different analyzed parameters obtained in this work from huFcRn affinity chromatography (rPW and rRT) showed no significant correlation with each other ($\rho = 0.41$).¹¹¹ This may be related to differences between selected study molecules and effects mediated by the conjugated linker-payload that may impair FcRn affinity chromatography elution profiles in this study. The bis-ANS assay that was used to analyze the hydrophobicity of the ADCs showed a modest correlation with FcRn affinity chromatography rPW ($\rho = 0.65$) but no significant correlation with FcRn affinity chromatography rRT ($\rho = 0.29$). This indicates that hydrophobic interactions may have a greater influence on the peak width than on the retention time. Furthermore, the bis-ANS assay did not show significant correlations with CSI-BLI and BVP-ELISA (ρ of 0.45 and 0.51, respectively), but modest correlation with AC-SINS ($\rho = 0.68$), PSR-BLI ($\rho = 0.71$) and Heparin ELISA ($\rho = 0.70$). Overall, a clustering of the assays according to the analyzed physicochemical properties is possible with AC-SINS and CSI-BLI in one cluster and PSR-BLI, BVP-ELISA and Heparin-ELISA in another cluster. However, also a cluster comprising all self-interaction and non-specific binding assays could be formed. In both cases, the bis-ANS assay and the huFcRn affinity chromatography can be seen as separated. These correlations suggest that single assays from assays that form strong clusters may be redundant. However, once again it should be emphasized that the correlations shown here were based on only a few data points and more robust statistical analyses requires increasing sample numbers. In addition, this kind of correlation can help when refining the screening tool selection, but first, it is even more important to assess whether an assay is suitable for the purpose of selecting ADCs with potentially good PK behavior. For this, the correlations of the different assay results with the CL values of the ADCs will be presented in the following section.

	CSI-BLI	AC-SINS	bis-ANS	PSR-BLI	Heparin ELISA	BVP ELISA	huFcRn column (rPW)	huFcRn column (rRT)
CSI-BLI		0.91	0.45	0.80	0.80	0.81	0.81	0.70
AC-SINS	0.91		0.68	0.87	0.86	0.81	0.84	0.65
bis-ANS	0.45	0.68		0.71	0.70	0.51	0.63	0.29
PSR-BLI	0.80	0.87	0.71		0.88	0.70	0.74	0.72
Heparin ELISA	0.80	0.86	0.70	0.88		0.89	0.65	0.69
BVP ELISA	0.81	0.81	0.51	0.70	0.89		0.59	0.47
huFcRn column (rPW)	0.81	0.84	0.63	0.74	0.65	0.59		0.41
huFcRn column (rRT)	0.70	0.65	0.29	0.72	0.69	0.47	0.41	

Figure 28. Correlation of *in vitro* assay results. Spearman correlations (ρ) for pairwise comparison of the *in vitro* assay data from the 13 study ADCs are shown. Significant correlations ($p < 0.05$) are marked as green gradient (ρ of 0.5 to 1.0; -0.5 to -1.0), no significant correlations are marked in gray (ρ of 0.49 to -0.49).

7.2.7. Correlation of *In Vitro* Assay Results with *In Vivo* Pharmacokinetics

Finally, *in vitro in vivo* correlations (IVIVCs) were performed for all ADCs wherein *in vitro* assay values were correlated with the total antibody clearance values determined in huFcRn transgenic Tg276 mice (**Figure 29**). So far, only for one of the shown assays the correlation between PK and assay results was investigated for ADCs.¹⁷¹ In this study, Tumey *et al.* described the use of the AC-SINS assay for trastuzumab-VC-PAB-MMAE ADCs conjugated at different sites. However a correlation between AC-SINS scores and the total antibody

clearance in rats for the respective ADCs was not found.¹⁷¹ In more detail, only minor differences in AC-SINS scores and a narrow range of CL values with maximum 2.3-fold difference between ADCs with most elevated and most reduced CL was reported.¹⁷¹ In the study presented here, for ten ADCs (ADC1-ADC10) that showed a maximum 4.3-fold difference in CL in the Tg276 mice, a correlation with self-association measured by AC-SINS could not be found as well (**Figure 29, a**). However, when including all 13 study ADCs a correlation was found. The strength of association between the assay results and CL values was analyzed statistically by Spearman's rank correlation (**Figure 29**). This statistical analysis revealed moderate significant correlations ($p < 0.05$) for the AC-SINS assay results with CL ($\rho = 0.64$). Moreover, moderate significant correlations with CL were additionally analyzed for the second self-interaction assay, CSI-BLI ($\rho = 0.58$) and for the huFcRn column chromatography rPW ($\rho = 0.72$). In contrast, no significant correlations were found for all remaining assays (**Figure 29**). However, the statistical lack of correlation is not yet a reason to consider these assays unsuitable to identify ADCs with risk for poor PK: Overall no perfect ranking of the data with the CL was found but the data of ADCs with CL values below approximately 4 mL/h/kg formed a cluster when correlated with the assay results and either showed narrow scattering as seen for the AC-SINS assay, PSR-BLI, bis-ANS, and huFcRn affinity chromatography rPW (**Figure 29, a, e, f and g**, respectively) or a rather broad widely scattering provided by a broader range of scores as seen for CSI-BLI (**Figure 29, b**) and FcRn affinity chromatography rRTs (**Figure 29, h**). The clustering prevents strong Spearman's rank correlations between the CL and assay results but is not untypically for such assays that are highly artificial compared to the *in vivo* situation.^{111,121} It was emphasized, that the published assays cannot be used as prediction tools because of the scattering in the data. However, they were described as screening tools as the assay results allowed to calculate thresholds, where molecules with threshold violation were associated to fast CL whereas molecules exhibiting acceptable assay results were linked to slow CL.^{111,121}

Because of the small data set in here, a final threshold has not yet been defined for the assays used to analyze the study ADCs. However, the three ADCs (ADC11-ADC13) with the most rapid clearance (5.91-8.30 mL/h/kg) showed the highest results in all assays and can therefore be clearly identified by all assays. Furthermore, ADC10 that had a clearance of 5.01 mL/h/kg showed higher assay readouts than the ADCs with a slower clearance (< 4 mL/h/kg) and lower assay readouts than the three fastest cleared ADCs in five of the assays, namely BVP ELISA, Heparin ELISA, PSR-BLI, bis-ANS, and the huFcRn affinity chromatography parameter rPW (**Figure 29, c, d, e, f and g**, respectively). Interestingly, with the BVP ELISA an additional separation of two ADCs with very slow clearance values and low ELISA scores can be seen (**Figure 29, c**).

However, in some of the shown IVIVCs some ADCs showed a conspicuous high assay result but had a slow clearance. For both ELISA-based measurements (Heparin and BVP) this was true for three ADCs: ADC1, ADC6, and ADC9 (**Figure 29, c and d**). In addition, the same phenomenon was also observed for the PSR-BLI assay

but just for ADC9 (**Figure 29, e**), or for the huFcRn column chromatography rRT for ADC1 (**Figure 29, h**). When applying thresholds for such kind of assays, molecules with high assay results but slow clearance (false positive results) could be erroneously rejected which could lead to the loss of suitable candidates. Also, false negative results are possible, where ADCs with fast CL exhibit assay results below the threshold and thus could not be identified as molecules with a high risk for poor PK. However, analyzing false positive or negative results for a low percentage of analyzed molecules is acceptable for such assays.^{111,121} To overcome the limitations of single assays and to minimize the risk for a false selection, the use of a set of different assays to analyze different properties of the molecule and a selection strategy is recommended.^{111,123,198} For the selection strategy a red flag system, where molecules with a value above the threshold in an assay are marked with a red flag, is often used.^{111,123,198} For example, Avery *et al.* reported a strategy where the different assays were sorted into different categories according to the analyzed biophysical properties.¹¹¹ In total they divided the assays into three different categories. If a mAb scored above the threshold in one of the assays in a specific category this category was marked red for this mAb. Best results with minimal false selection were found when only mAbs that were marked red in all three categories were guided to be rejected.¹¹¹ A similar selection strategy is conceivable for the assays shown in this study. However, the small data set in here that does not allow to define reliable thresholds also does not yet allow to define a selection strategy.

Beside the correct classification of mAbs and ADCs, the feasibility of high- and mid-throughput measurements and a reduced material consumption was described as requisite for the application of such assays during hit discovery and early development. Considering these attributes, the assays presented here all match these requirements, except for the huFcRn affinity chromatography (104 min per test item). Moreover, robust assay readouts are another critical factor. Robust readouts by performing duplicate measurements were shown to be applicable in this study for AC-SINS, CSI-BLI, PSR-BLI, bis-ANS, and huFcRn affinity chromatography and by using three to four technical replicates for heparin and BVP ELISA, respectively. Despite these duplicate and technical replicate measurements, little material amounts (305 µg for the full assay panel) are required.

Overall, for all these assays an association between the assay results and CL values was found to some extent. However, as the number of ADCs assessed in this study was limited, the expansion of the data set to include more ADC variants is required to allow more robust statistical analyses that will ultimately allow the establishment of robust thresholds and a robust selection strategy. Nevertheless, the results and various assays presented in this study may be of great utility for research in the ADC field to reduce the number of preclinical *in vivo* studies and to increase the chance to discover and develop ADCs with favorable PK.

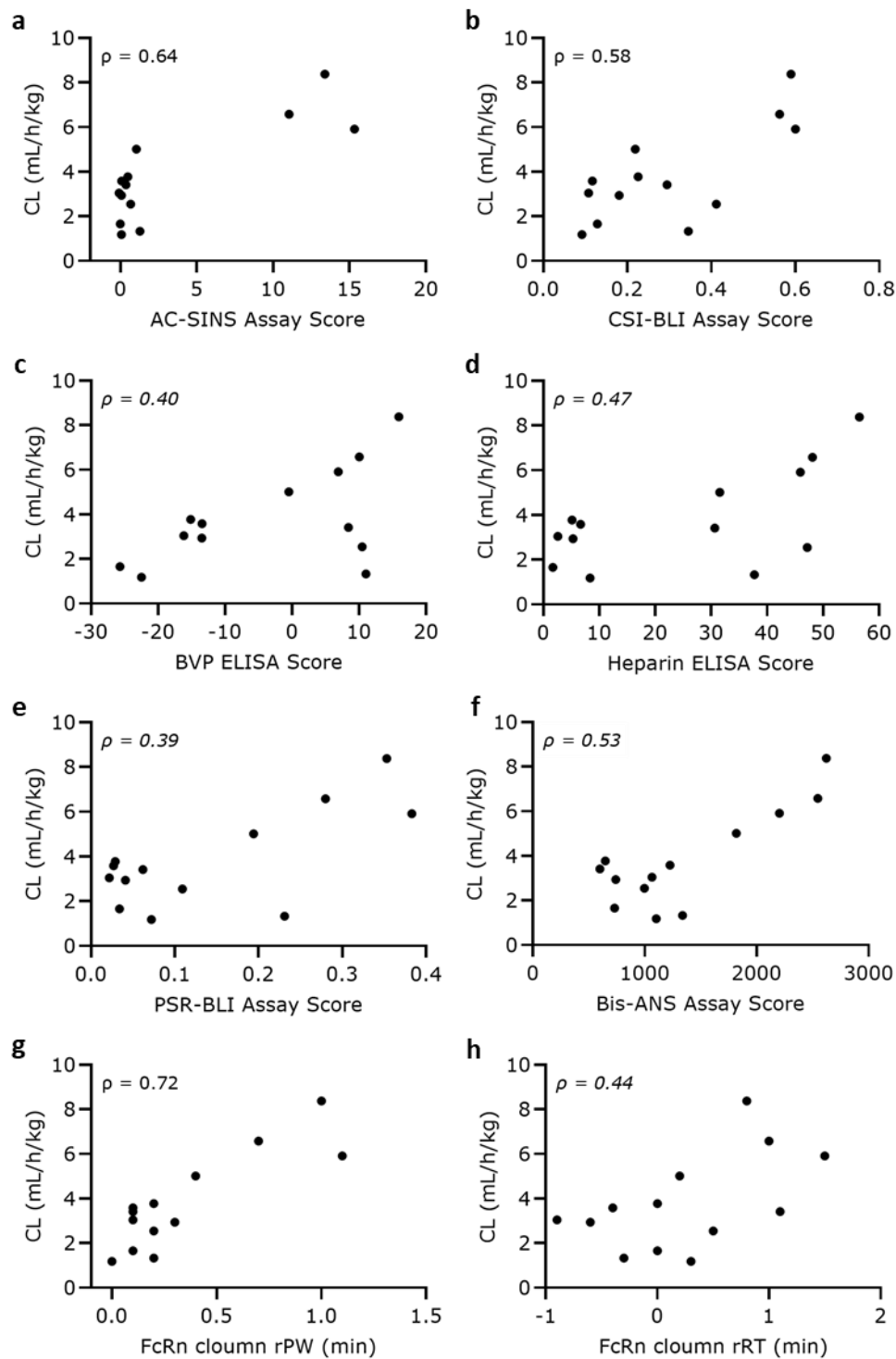


Figure 29. Relationship between the clearance in huFcRn transgenic mice (hemizygous Tg276) and the results in different *in vitro* assays of the 13 study ADCs. The total antibody CL value for each ADC is plotted against the corresponding *in vitro* assay parameters: AC-SINS assay score (**a**), CSI-BLI assay score (**b**), BVP ELISA score (**c**), heparin ELISA score (**d**), PSR-BLI assay score (**e**), bis-ANS assay score (**f**), huFcRn column chromatography rPW (**g**) and rRT (**h**). Spearman correlation (ρ) for total mAb CL in mice with each *in vitro* assay is shown either straight if there is a significant correlation ($p < 0.05$) or in italic if the correlation is not significant.

8. Outlook

The aim of this study was to evaluate physicochemical property assays as indicators for poor PK of ADCs. To test the feasibility of this approach, data from physicochemical property assays, obtained from a series of study ADCs, were correlated with CL values from huFcRn transgenic mouse PK studies. Here we could show for the first time that physicochemical property assays were successfully adapted and applied to ADCs and that a positive association between assay readouts and CL values was observed for several assays.

One shortcoming of this study is the limited number of ADCs used for correlation which does not allow robust statistical analyses. Therefore, as already mentioned, further data points are required for the IVIVCs to establish robust thresholds which may allow refinement of the selected assays. Even more important is that the establishment of thresholds in combination with a selection strategy, for example, as described in section 7.2.7, can be used to minimize the risk for false selections caused by possible false positive or negative results in single assays. In addition, if the data set with ADCs of different designs would be large enough, this would maybe allow a better understanding of the relative influence of the individual ADC components and design properties (mAb, linker, payload, DAR, conjugation site and method) on the physicochemical properties and PK. Regarding the physicochemical properties, this could also be possible if enough ADCs of different designs for which no PK data are available would be analyzed with the assays, even though this data would not contribute to the IVIVCs. Furthermore, the detailed analyses of different ADC subclasses could allow to identify the components and design properties with most impact.

In addition, it is possible that further data points would not confirm the suitability of the assays as screening tools to identify ADCs with risk for poor PK but would impair the correlation, so that reasonable thresholds with a low number of false results could not be established. If this would be the case for too many assays, so that a robust selection could no longer be guaranteed, or if it would even be the case for all the assays, the high relevance of identifying assays that are suitable would suggest that further assays should be developed, established, and tested for their suitability.

Moreover, in this study we could show that hemizygous Tg276 mice can be used to identify differences in PK of ADCs caused by minimal differences in their design. Another important huFcRn mouse model is the homozygous Tg32 mouse. Beside that the used mice strain in this study is hemizygous and this Tg32 strain is homozygous for the huFcRn gene, both express huFcRn under control of a different promoter (see section 4.3.3). These differences in both mice strains result in differences in the clearance of molecules in both strains. In this context, mAbs were shown to be cleared faster in hemizygous Tg276 mice than in homozygous Tg32 mice.^{140,152} Furthermore, recently, the homozygous Tg32 mice strain has been suggested to be currently

the best suitable mouse strain to predict human PK of mAbs.^{142,146,150,154,155} It cannot be expected that the ranking of clearance values obtained for the ADCs in the hemizygous Tg267 mice would completely be different in homozygous Tg32 mice, that molecules that showed really poor PK in Tg267 mice would suddenly show better PK in the Tg32 mice than the molecules with good PK in Tg276 mice, and vice versa. However, it cannot be completely ruled out that the ADCs shown in this study might have a slightly different clearance ranking in this Tg32 mouse strain, which could affect the correlation. Although it has been shown that homozygous Tg32 mice are suitable to predict human PK of mAbs, the same cannot yet be precluded for hemizygous Tg276 mice, since only very few mAbs with available human PK data were analyzed for their PK in hemizygous Tg276 mice.^{126,142,146,150,154,155} Furthermore, there is no indication yet whether the human PK prediction also applies to ADCs. Therefore, a head-to-head comparison of both strains by analyzing the PK of different molecules with available human PK data, including also especially ADCs, in both strains would be desirable. This would allow to identify which of the two strains is the better with respect to human PK prediction and would therefore be better suitable for correlations with the assay results. If this suggested comparison of the two strains would confirm the better suitability of the homozygous Tg32 mice strain, then also the suitability of the assays to indicate PK shown in this study should be reconfirmed using ADCs with PK data from these mice.

9. References

1. Kaempffe, A. *et al.* Effect of conjugation site and technique on the stability and pharmacokinetics of antibody-drug conjugates. *J. Pharm. Sci.* **110**, 3776–3785 (2021).
2. Bray, F., Laversanne, M., Weiderpass, E. & Soerjomataram, I. The ever-increasing importance of cancer as a leading cause of premature death worldwide. *Cancer* **127**, 3029–3030 (2021).
3. Tong, J. T. W., Harris, P. W. R., Brimble, M. A. & Kaviani, I. An Insight into FDA Approved Antibody-Drug Conjugates for Cancer Therapy. *Molecules* **26**, 5847 (2021).
4. Hafeez, U., Parakh, S., Gan, H. K. & Scott, A. M. Antibody-Drug Conjugates for Cancer Therapy. *Molecules* **25**, 4764 (2020).
5. Kovtun, Y. V. & Goldmacher, V. S. Cell killing by antibody-drug conjugates. *Cancer Lett.* **255**, 232–240 (2007).
6. Panowski, S., Bhakta, S., Raab, H., Polakis, P. & Junutula, J. R. Site-specific antibody drug conjugates for cancer therapy. *MAbs* **6**, 34–45 (2014).
7. Tarcsa, E., Guffroy, M. R., Falahatpisheh, H., Phipps, C. & Kalvass, J. C. Antibody-drug conjugates as targeted therapies: Are we there yet? A critical review of the current clinical landscape. *Drug Discov. Today Technol.* **37**, 13–22 (2020).
8. Chalouni, C. & Doll, S. Fate of Antibody-Drug Conjugates in Cancer Cells. *J. Exp. Clin. Cancer Res.* **37**, 20 (2018).
9. Kitson, S. *et al.* Antibody-Drug Conjugates (ADCs) - Biotherapeutic bullets. *Chim. Oggi* **31**, 29–35 (2013).
10. Vidarsson, G., Dekkers, G. & Rispen, T. IgG Subclasses and Allotypes: From Structure to Effector Functions. *Front. Immunol.* **5**, 520 (2014).
11. Kellner, C., Derer, S., Valerius, T. & Peipp, M. Boosting ADCC and CDC activity by Fc engineering and evaluation of antibody effector functions. *Methods* **65**, 105–113 (2014).
12. Yu, J., Song, Y. & Tian, W. How to select IgG subclasses in developing anti-tumor therapeutic antibodies. *J. Hematol. Oncol.* **13**, 45 (2020).
13. Baah, S., Laws, M. & Rahman, K. M. Antibody-Drug Conjugates—A Tutorial Review. *Molecules* **26**, 2943 (2021).
14. Zammarchi, F. *et al.* ADCT-402, a PBD dimer-containing antibody drug conjugate targeting CD19-expressing malignancies. *Blood* **131**, 1094–1105 (2018).
15. Perez, H. L. *et al.* Antibody-drug conjugates: current status and future directions. *Drug Discov. Today* **19**, 869–881 (2014).

-
16. Kamath, A. V. & Iyer, S. Preclinical pharmacokinetic considerations for the development of antibody drug conjugates. *Pharm. Res.* **32**, 3470–3479 (2015).
 17. Köhler, G. & Milstein, C. Continuous cultures of fused cells secreting antibody of predefined specificity. *Nature* **256**, 495–497 (1975).
 18. Liu, J. K. H. The history of monoclonal antibody development – Progress, remaining challenges and future innovations. *Ann. Med. Surg.* **3**, 113–116 (2014).
 19. Khazaeli, M. B., Conry, R. M. & LoBuglio, A. F. Human immune response to monoclonal antibodies. *J. Immunother.* **15**, 42–52 (1994).
 20. Safdari, Y., Farajnia, S., Asgharzadeh, M. & Khalili, M. Antibody humanization methods – a review and update. *Biotechnol. Genet. Eng. Rev.* **29**, 175–186 (2013).
 21. Brüggemann, M. *et al.* Human Antibody Production in Transgenic Animals. *Arch. Immunol. Ther. Exp. (Warsz)*. **63**, 101–108 (2015).
 22. Metzker, M. L. Sequencing technologies — the next generation. *Nat. Rev. Genet.* **11**, 31–46 (2010).
 23. Verma, R., Boleti, E. & George, A. J. T. Antibody engineering: Comparison of bacterial, yeast, insect and mammalian expression systems. *J. Immunol. Methods* **216**, 165–181 (1998).
 24. Klemm, J., Pekar, L., Krah, S. & Zielonka, S. Antibody Display Systems. in *Introduction to Antibody Engineering* (eds. Rüker, F. & Wozniak-Knopp, G.) 65–96 (Springer, Cham, 2021). doi:10.1007/978-3-030-54630-4_4.
 25. Buss, N. A. P. S., Henderson, S. J., McFarlane, M., Shenton, J. M. & de Haan, L. Monoclonal antibody therapeutics: history and future. *Curr. Opin. Pharmacol.* **12**, 615–622 (2012).
 26. Ma, J. *et al.* Bispecific Antibodies: From Research to Clinical Application. *Frontiers in Immunology* vol. 12 626616 (2021).
 27. Shim, H. Bispecific Antibodies and Antibody-Drug Conjugates for Cancer Therapy: Technological Considerations. *Biomolecules* **10**, 360 (2020).
 28. Tang, J., Gong, Y. & Ma, X. Bispecific Antibodies Progression in Malignant Melanoma. *Front. Pharmacol.* **13**, 837889 (2022).
 29. Hanson Wade: ADC Beacon Targeted Therapies database. <https://beacon-intelligence.com/solutions/adc> (May 2022).
 30. Hoffmann, R. M. *et al.* Antibody structure and engineering considerations for the design and function of Antibody Drug Conjugates (ADCs). *Oncoimmunology* **7**, e1395127 (2018).
 31. Tiller, K. E. & Tessier, P. M. Advances in Antibody Design. *Annu. Rev. Biomed. Eng.* **17**, 191–216 (2015).
 32. Deonarain, M. P., Yahioğlu, G., Stamati, I. & Marklew, J. Emerging formats for next-generation antibody drug conjugates. *Expert Opin. Drug Discov.* **10**, 463–481 (2015).

-
33. Beck, A., Goetsch, L., Dumontet, C. & Corvaia, N. Strategies and challenges for the next generation of antibody–drug conjugates. *Nat. Rev. Drug Discov.* **16**, 315–337 (2017).
 34. Kostova, V., Désos, P., Starck, J.-B. & Kotschy, A. The Chemistry Behind ADCs. *Pharmaceuticals* **14**, 442 (2021).
 35. Lyon, R. P. *et al.* Reducing hydrophobicity of homogeneous antibody–drug conjugates improves pharmacokinetics and therapeutic index. *Nat. Biotechnol.* **33**, 733–735 (2015).
 36. Hamblett, K. J. *et al.* Effects of drug loading on the antitumor activity of a monoclonal antibody drug conjugate. *Clin. Cancer Res.* **10**, 7063–7070 (2004).
 37. Tumey, L. N. Next Generation Payloads for ADCs. in *Innovations for Next-Generation Antibody-Drug Conjugates. Cancer Drug Discovery and Development* (ed. Damelin, M.) 187–214 (Humana Press, Cham, 2018). doi:10.1007/978-3-319-78154-9_8.
 38. Kim, E. G. & Kim, K. M. Strategies and advancement in antibody–drug conjugate optimization for targeted cancer therapeutics. *Biomol. Ther.* **23**, 493–509 (2015).
 39. Lu, J., Jiang, F., Lu, A. & Zhang, G. Linkers Having a Crucial Role in Antibody–Drug Conjugates. *Int. J. Mol. Sci.* **17**, 561 (2016).
 40. Su, Z. *et al.* Antibody–drug conjugates: Recent advances in linker chemistry. *Acta Pharm. Sin. B* **11**, 3889–3907 (2021).
 41. Mohamed, M. M. & Sloane, B. F. Cysteine cathepsins: multifunctional enzymes in cancer. *Nat. Rev. Cancer* **6**, 764–775 (2006).
 42. Dubowchik, G. M. *et al.* Cathepsin B-Labile Dipeptide Linkers for Lysosomal Release of Doxorubicin from Internalizing Immunoconjugates: Model Studies of Enzymatic Drug Release and Antigen-Specific In Vitro Anticancer Activity. *Bioconjug. Chem.* **13**, 855–869 (2002).
 43. Bargh, J. D., Isidro-Llobet, A., Parker, J. S. & Spring, D. R. Cleavable linkers in antibody–drug conjugates. *Chem. Soc. Rev.* **48**, 4361–4374 (2019).
 44. Caculitan, N. G. *et al.* Cathepsin B is dispensable for cellular processing of cathepsin B-cleavable antibody–drug conjugates. *Cancer Res.* **77**, 7027–7037 (2017).
 45. Dorywalska, M. *et al.* Molecular basis of valine-citrulline-PABC linker instability in site-specific ADCs and its mitigation by linker design. *Mol. Cancer Ther.* **15**, 958–970 (2016).
 46. Ubink, R. *et al.* Unraveling the Interaction between Carboxylesterase 1c and the Antibody–Drug Conjugate SYD985: Improved Translational PK/PD by Using Ces1c Knockout Mice. *Mol. Cancer Ther.* **17**, 2389–2398 (2018).
 47. Tedeschini, T. *et al.* Polyethylene glycol-based linkers as hydrophilicity reservoir for antibody–drug conjugates. *J. Control. Release* **337**, 431–447 (2021).

-
48. Tsuchikama, K. & An, Z. Antibody-drug conjugates: recent advances in conjugation and linker chemistries. *Protein Cell* **9**, 33–46 (2018).
 49. Shen, B.-Q. *et al.* Conjugation site modulates the in vivo stability and therapeutic activity of antibody-drug conjugates. *Nat. Biotechnol.* **30**, 184–189 (2012).
 50. Junutula, J. R. R. *et al.* Site-specific conjugation of a cytotoxic drug to an antibody improves the therapeutic index. *Nat. Biotechnol.* **26**, 925–932 (2008).
 51. Zhou, Q. Site-Specific Antibody Conjugation for ADC and Beyond. *Biomedicines* **5**, 64 (2017).
 52. Kaur, S., Xu, K., Saad, O. M., Dere, R. C. & Carrasco-Triguero, M. Bioanalytical assay strategies for the development of antibody–drug conjugate biotherapeutics. *Bioanalysis* **5**, 201–226 (2013).
 53. Junutula, J. R. *et al.* Rapid identification of reactive cysteine residues for site-specific labeling of antibody-Fabs. *J. Immunol. Methods* **332**, 41–52 (2008).
 54. Lyons, A. *et al.* Site-specific attachment to recombinant antibodies via introduced surface cysteine residues. *Protein Eng. Des. Sel.* **3**, 703–708 (1990).
 55. Ohri, R. *et al.* High-Throughput Cysteine Scanning To Identify Stable Antibody Conjugation Sites for Maleimide- and Disulfide-Based Linkers. *Bioconjug. Chem.* **29**, 473–485 (2018).
 56. Sussman, D. *et al.* Engineered cysteine antibodies: an improved antibody-drug conjugate platform with a novel mechanism of drug-linker stability. *Protein Eng. Des. Sel.* **31**, 47–54 (2018).
 57. Su, D. *et al.* Modulating antibody-drug conjugate payload metabolism by conjugation site and linker modification. *Bioconjug. Chem.* **29**, 1155–1167 (2018).
 58. Tumey, L. N. *et al.* Optimization of Tubulysin Antibody-Drug Conjugates: A Case Study in Addressing ADC Metabolism. *ACS Med. Chem. Lett.* **7**, 977–982 (2016).
 59. Alley, S. C. *et al.* Contribution of linker stability to the activities of anticancer immunoconjugates. *Bioconjug. Chem.* **19**, 759–765 (2008).
 60. Tumey, L. N. *et al.* Mild method for succinimide hydrolysis on ADCs: impact on ADC potency, stability, exposure, and efficacy. *Bioconjug. Chem.* **25**, 1871–1880 (2014).
 61. Akkapeddi, P. *et al.* Construction of Homogeneous Antibody-drug Conjugates using Site-selective Protein Chemistry. *Chem. Sci.* **7**, 2954–2963 (2016).
 62. Faria, M. *et al.* Multiplex LC-MS/MS assays for clinical bioanalysis of MEDI4276, an antibody-drug conjugate of tubulysin analogue attached via cleavable linker to a biparatopic humanized antibody against HER-2. *Antibodies* **8**, 1–31 (2019).
 63. Bai, C. *et al.* Site-specific conjugation of the indolinobenzodiazepine DGN549 to antibodies affords antibody–drug conjugates with an improved therapeutic index as compared with lysine conjugation. *Bioconjug. Chem.* **31**, 93–103 (2020).

-
64. Dimasi, N. *et al.* Efficient preparation of site-specific antibody–drug conjugates using cysteine insertion. *Mol. Pharm.* **14**, 1501–1516 (2017).
 65. Jeffrey, S. C. *et al.* A potent anti-CD70 antibody–drug conjugate combining a dimeric pyrrolobenzodiazepine drug with site-specific conjugation technology. *Bioconjug. Chem.* **24**, 1256–1263 (2013).
 66. Li, F. *et al.* Characterization of SGN-CD123A, a potent CD123-directed antibody–drug conjugate for acute myeloid leukemia. *Mol. Cancer Ther.* **17**, 554–564 (2018).
 67. Lewis, T. *et al.* SGN-CD352A: A novel humanized anti-CD352 antibody-drug conjugate for the treatment of multiple myeloma. *Cancer Res.* **76**, Abstract nr 1195 (2016).
 68. Kung Sutherland, M. S. *et al.* SGN-CD33A: a novel CD33-targeting antibody–drug conjugate using a pyrrolobenzodiazepine dimer is active in models of drug-resistant AML. *Blood* **122**, 1455–1463 (2013).
 69. Ryan, M. C. *et al.* Therapeutic potential of SGN-CD19B, a PBD-based anti-CD19 drug conjugate, for treatment of B-cell malignancies. *Blood* **130**, 2018–2026 (2017).
 70. Hartley, J. A. Antibody-drug conjugates (ADCs) delivering pyrrolobenzodiazepine (PBD) dimers for cancer therapy. *Expert Opin. Biol. Ther.* **21**, 931–943 (2020).
 71. Phillips, T. *et al.* A phase 1 trial of SGN-CD70A in patients with CD70-positive diffuse large B cell lymphoma and mantle cell lymphoma. *Invest. New Drugs* **37**, 297–306 (2019).
 72. Pal, S. K. *et al.* A phase 1 trial of SGN-CD70A in patients with CD70-positive, metastatic renal cell carcinoma. *Cancer* **125**, 1124–1132 (2019).
 73. Rinnerthaler, G., Gampenrieder, S. P. & Greil, R. HER2 directed antibody-drug-conjugates beyond T-DM1 in breast cancer. *Int. J. Mol. Sci.* **20**, 1–17 (2019).
 74. Li, J. Y. *et al.* A biparatopic HER2-targeting antibody-drug conjugate induces tumor regression in primary models refractory to or ineligible for HER2-targeted therapy. *Cancer Cell* **29**, 117–129 (2016).
 75. Lutz, C. *et al.* Amanitin Conjugates. *WO2017149077* (2017).
 76. Anderl, J., Hechler, T., Müller, C. & Pahl, A. Amatoin-Antibody Conjugates. *US 2018/0043033 A1* (2018).
 77. Wozniak-Knopp, G. *et al.* Cysteine Engineered Antigen-Binding Molecules. *US 2020/0277399 A1* (2020).
 78. Yokoyama, K., Nio, N. & Kikuchi, Y. Properties and applications of microbial transglutaminase. *Appl. Microbiol. Biotechnol.* **64**, 447–454 (2004).
 79. Jeger, S. *et al.* Site-specific and stoichiometric modification of antibodies by bacterial transglutaminase. *Angew. Chemie Int. Ed.* **49**, 9995–9997 (2010).
 80. Strop, P. *et al.* Location matters: site of conjugation modulates stability and pharmacokinetics of

-
- antibody drug conjugates. *Chem. Biol.* **20**, 161–167 (2013).
81. Dickgiesser, S. *et al.* Site-specific conjugation of native antibodies using engineered microbial transglutaminases. *Bioconjug. Chem.* **31**, 1070–1076 (2020).
 82. Strop, P. Versatility of microbial transglutaminase. *Bioconjug. Chem.* **25**, 855–862 (2014).
 83. Strop, P. *et al.* Site-specific conjugation improves therapeutic index of antibody drug conjugates with high drug loading. *Nat. Biotechnol.* **33**, 694–696 (2015).
 84. Dorywalska, M. *et al.* Effect of attachment site on stability of cleavable antibody drug conjugates. *Bioconjug. Chem.* **26**, 650–659 (2015).
 85. Dorywalska, M. *et al.* Site-dependent degradation of a non-cleavable auristatin-based linker-payload in rodent plasma and its effect on ADC efficacy. *PLoS One* **10**, e0132282 (2015).
 86. Wong, O. K. *et al.* RN765C, a low affinity EGFR antibody drug conjugate with potent anti-tumor activity in preclinical solid tumor models. *Oncotarget* **9**, 33446–33458 (2018).
 87. Strop, P. *et al.* RN927C, a site-specific Trop-2 antibody-drug conjugate (ADC) with enhanced stability, is highly efficacious in preclinical solid tumor models. *Mol. Cancer Ther.* **15**, 2698–2708 (2016).
 88. Ratnayake, A. S. *et al.* Natural product bis-intercalator depsipeptides as a new class of payloads for antibody–drug conjugates. *Bioconjug. Chem.* **30**, 200–209 (2019).
 89. King, G. T. *et al.* A phase 1, dose-escalation study of PF-06664178, an anti-Trop-2/Aur0101 antibody-drug conjugate in patients with advanced or metastatic solid tumors. *Invest. New Drugs* **36**, 836–847 (2018).
 90. Thurber, G. M., Schmidt, M. M. & Wittrup, K. D. Antibody tumor penetration: Transport opposed by systemic and antigen-mediated clearance. *Adv. Drug Deliv. Rev.* **60**, 1421–1434 (2008).
 91. Li, C. *et al.* Clinical pharmacology of vc-MMAE antibody–drug conjugates in cancer patients: learning from eight first-in-human Phase 1 studies. *MAbs* **12**, 1699768 (2020).
 92. Ponte, J. F. *et al.* Antibody Co-Administration Can Improve Systemic and Local Distribution of Antibody–Drug Conjugates to Increase In Vivo Efficacy. *Mol. Cancer Ther.* **20**, 203–212 (2021).
 93. Dixit, R. Minimizing off-target toxicity and improve targeting to tumor associated antigens. in *8th annual World ADC San Diego* (2017).
 94. Saber, H. Antibody-Drug Conjugates: what are the data telling us? A retrospective review with emphasis on human starting dose. <http://docplayer.net/44580026-Antibody-drug-conjugates.html> (2021).
 95. Ovacik, M. & Lin, K. Tutorial on Monoclonal Antibody Pharmacokinetics and Its Considerations in Early Development. *Clin. Transl. Sci.* **11**, 540–552 (2018).
 96. Burke, P. J. *et al.* Optimization of a PEGylated glucuronide-monomethylauristatin E linker for antibody-

-
- drug conjugates. *Mol. Cancer Ther.* **16**, 116–123 (2017).
97. Simmons, J. K., Burke, P. J., Cochran, J. H., Pittman, P. G. & Lyon, R. P. Reducing the antigen-independent toxicity of antibody-drug conjugates by minimizing their non-specific clearance through PEGylation. *Toxicol. Appl. Pharmacol.* **392**, 114932 (2020).
98. Lin, K. & Tibbitts, J. Pharmacokinetic considerations for antibody drug conjugates. *Pharm. Res.* **29**, 2354–2366 (2012).
99. Lucas, A. T. *et al.* Factors Affecting the Pharmacology of Antibody–Drug Conjugates. *Antibodies* **7**, 1–28 (2018).
100. Tabrizi, M. A., Tseng, C.-M. L. & Roskos, L. K. Elimination mechanisms of therapeutic monoclonal antibodies. *Drug Discov. Today* **11**, 81–88 (2006).
101. Subedi, G. P. & Barb, A. W. The Structural Role of Antibody N-Glycosylation in Receptor Interactions. *Structure* **23**, 1573–1583 (2015).
102. Ryman, J. T. & Meibohm, B. Pharmacokinetics of Monoclonal Antibodies. *CPT pharmacometrics Syst. Pharmacol.* **6**, 576–588 (2017).
103. Andersen, J. T. & Sandlie, I. The Versatile MHC Class I-related FcRn Protects IgG and Albumin from Degradation: Implications for Development of New Diagnostics and Therapeutics. *Drug Metab. Pharmacokinet.* **24**, 318–332 (2009).
104. Garg, A. & Balthasar, J. P. Physiologically-based pharmacokinetic (PBPK) model to predict IgG tissue kinetics in wild-type and FcRn-knockout mice. *J. Pharmacokinet. Pharmacodyn.* **34**, 687–709 (2007).
105. Pyzik, M. *et al.* The Neonatal Fc Receptor (FcRn): A Misnomer? *Front. Immunol.* **10**, 1540 (2019).
106. Latvala, S., Jacobsen, B., Otteneder, M. B., Herrmann, A. & Kronenberg, S. Distribution of FcRn Across Species and Tissues. *J. Histochem. Cytochem.* **65**, 321–333 (2017).
107. Roopenian, D. C. *et al.* The MHC Class I-Like IgG Receptor Controls Perinatal IgG Transport, IgG Homeostasis, and Fate of IgG-Fc-Coupled Drugs. *J. Immunol.* **170**, 3528–3533 (2003).
108. Chaudhury, C. *et al.* The major histocompatibility complex-related Fc receptor for IgG (FcRn) binds albumin and prolongs its lifespan. *J. Exp. Med.* **197**, 315–322 (2003).
109. Chaudhury, C., Brooks, C. L., Carter, D. C., Robinson, J. M. & Anderson, C. L. Albumin Binding to FcRn: Distinct from the FcRn–IgG Interaction. *Biochemistry* **45**, 4983–4990 (2006).
110. Dostalek, M., Prueksaritanont, T. & Kelley, R. F. Pharmacokinetic de-risking tools for selection of monoclonal antibody lead candidates. *MAbs* **9**, 756–766 (2017).
111. Avery, L. B. *et al.* Establishing in vitro in vivo correlations to screen monoclonal antibodies for physicochemical properties related to favorable human pharmacokinetics. *MAbs* **10**, 244–255 (2018).
112. Bumbaca, D. *et al.* Highly specific off-target binding identified and eliminated during the humanization

-
- of an antibody against FGF receptor 4. *MAbs* **3**, 376–386 (2011).
113. Roopenian, D. C. & Akilesh, S. FcRn: the neonatal Fc receptor comes of age. *Nat. Rev. Immunol.* **7**, 715–725 (2007).
114. Datta-Mannan, A. Mechanisms Influencing the Pharmacokinetics and Disposition of Monoclonal Antibodies and Peptides. *Drug Metab. Dispos.* **47**, 1100–1110 (2019).
115. Datta-Mannan, A. *et al.* Balancing charge in the complementarity-determining regions of humanized mAbs without affecting pI reduces non-specific binding and improves the pharmacokinetics. *MAbs* **7**, 483–493 (2015).
116. Datta-Mannan, A. *et al.* The interplay of non-specific binding, target-mediated clearance and FcRn interactions on the pharmacokinetics of humanized antibodies. *MAbs* **7**, 1084–1093 (2015).
117. Li, B. *et al.* Framework selection can influence pharmacokinetics of a humanized therapeutic antibody through differences in molecule charge. *MAbs* **6**, 1255–1264 (2014).
118. Igawa, T. *et al.* Reduced elimination of IgG antibodies by engineering the variable region. *Protein Eng. Des. Sel.* **23**, 385–392 (2010).
119. Dobson, C. L. *et al.* Engineering the surface properties of a human monoclonal antibody prevents self-association and rapid clearance in vivo. *Sci. Rep.* **6**, 38644 (2016).
120. Boune, S., Hu, P., Epstein, A. L. & Khawli, L. A. Principles of N-Linked Glycosylation Variations of IgG-Based Therapeutics: Pharmacokinetic and Functional Considerations. *Antibodies* **9**, 22 (2020).
121. Hötzel, I. *et al.* A strategy for risk mitigation of antibodies with fast clearance. *MAbs* **4**, 753–760 (2012).
122. Sand, K. M. K. *et al.* Unraveling the Interaction between FcRn and Albumin: Opportunities for Design of Albumin-Based Therapeutics. *Front. Immunol.* **5**, 682 (2015).
123. Jain, T. *et al.* Biophysical properties of the clinical-stage antibody landscape. *Proc. Natl. Acad. Sci. U. S. A.* **114**, 944–949 (2017).
124. Schoch, A. *et al.* Charge-mediated influence of the antibody variable domain on FcRn-dependent pharmacokinetics. *Proc. Natl. Acad. Sci.* **112**, 5997–6002 (2015).
125. Piche-Nicholas, N. M. *et al.* Changes in complementarity-determining regions significantly alter IgG binding to the neonatal Fc receptor (FcRn) and pharmacokinetics. *MAbs* **10**, 81–94 (2018).
126. Wang, W. *et al.* Monoclonal antibodies with identical Fc sequences can bind to FcRn differentially with pharmacokinetic consequences. *Drug Metab. Dispos.* **39**, 1469–1477 (2011).
127. Prabhat, P. *et al.* Elucidation of intracellular recycling pathways leading to exocytosis of the Fc receptor, FcRn, by using multifocal plane microscopy. *Proc. Natl. Acad. Sci.* **104**, 5889–5894 (2007).
128. Datta-Mannan, A. *et al.* Humanized IgG₁ Variants with Differential Binding Properties to the Neonatal Fc Receptor: Relationship to Pharmacokinetics in Mice and Primates. *Drug Metab. Dispos.* **35**, 86–94

-
- (2007).
129. Datta-Mannan, A. & Wroblewski, V. J. Application of FcRn Binding Assays to Guide mAb Development. *Drug Metab. Dispos.* **42**, 1867–1872 (2014).
 130. Qi, T. & Cao, Y. In Translation: FcRn across the Therapeutic Spectrum. *Int. J. Mol. Sci.* **22**, 3048 (2021).
 131. Gurbaxani, B., Dela Cruz, L. L., Chintalacharuvu, K. & Morrison, S. L. Analysis of a family of antibodies with different half-lives in mice fails to find a correlation between affinity for FcRn and serum half-life. *Mol. Immunol.* **43**, 1462–1473 (2006).
 132. Schlothauer, T. *et al.* Analytical FcRn affinity chromatography for functional characterization of monoclonal antibodies. *MAbs* **5**, 576–586 (2013).
 133. Kelly, R. L. *et al.* Chaperone proteins as single component reagents to assess antibody nonspecificity. *MAbs* **9**, 1036–1040 (2017).
 134. Xu, Y. *et al.* Addressing polyspecificity of antibodies selected from an in vitro yeast presentation system: A FACS-based, high-throughput selection and analytical tool. *Protein Eng. Des. Sel.* **26**, 663–670 (2013).
 135. Kelly, R. L. *et al.* High throughput cross-interaction measures for human IgG1 antibodies correlate with clearance rates in mice. *MAbs* **7**, 770–777 (2015).
 136. Saluja, A. & Kalonia, D. S. Nature and consequences of protein–protein interactions in high protein concentration solutions. *Int. J. Pharm.* **358**, 1–15 (2008).
 137. Liu, Y. *et al.* High-throughput screening for developability during early-stage antibody discovery using self-interaction nanoparticle spectroscopy. *MAbs* **6**, 483–492 (2014).
 138. Foti, R. S. *et al.* Use of Cryopreserved Hepatocytes as Part of an Integrated Strategy to Characterize In Vivo Clearance for Peptide-Antibody Conjugate Inhibitors of Nav1.7 in Preclinical Species. *Drug Metab. Dispos.* **47**, 1111–1121 (2019).
 139. Meyer, D. W. *et al.* An in vitro assay using cultured kupffer cells can predict the impact of drug conjugation on in vivo antibody pharmacokinetics. *Mol. Pharm.* **17**, 802–809 (2020).
 140. Proetzel, G. & Roopenian, D. C. Humanized FcRn mouse models for evaluating pharmacokinetics of human IgG antibodies. *Methods* **65**, 148–153 (2014).
 141. Ober, R. J., Radu, C. G., Ghetie, V. & Ward, E. S. Differences in promiscuity for antibody-FcRn interactions across species: implications for therapeutic antibodies. *Int. Immunol.* **13**, 1551–1559 (2001).
 142. Avery, L. B. *et al.* Utility of a human FcRn transgenic mouse model in drug discovery for early assessment and prediction of human pharmacokinetics of monoclonal antibodies. *MAbs* **8**, 1064–1078 (2016).

-
143. Proetzel, G., Wiles, M. V & Roopenian, D. C. Genetically engineered humanized mouse models for preclinical antibody studies. *BioDrugs* **28**, 171–180 (2014).
 144. Li, T. & Balthasar, J. P. FcRn Expression in Wildtype Mice, Transgenic Mice, and in Human Tissues. *Biomolecules* **8**, 115 (2018).
 145. Stein, C. *et al.* Clinical chemistry of human FcRn transgenic mice. *Mamm. Genome* **23**, 259–269 (2012).
 146. Tam, S. H., McCarthy, S. G., Brosnan, K., Goldberg, K. M. & Scallon, B. J. Correlations between pharmacokinetics of IgG antibodies in primates vs. FcRn-transgenic mice reveal a rodent model with predictive capabilities. *MAbs* **5**, 397–405 (2013).
 147. Petkova, S. B. *et al.* Enhanced half-life of genetically engineered human IgG1 antibodies in a humanized FcRn mouse model: potential application in humorally mediated autoimmune disease. *Int. Immunol.* **18**, 1759–1769 (2006).
 148. Low, B. E., Christianson, G. J., Lowell, E., Qin, W. & Wiles, M. V. Functional humanization of immunoglobulin heavy constant gamma 1 Fc domain human FcγRT transgenic mice. *MAbs* **12**, e1829334 (2020).
 149. Zalevsky, J. *et al.* Enhanced antibody half-life improves in vivo activity. *Nat. Biotechnol.* **28**, 157–159 (2010).
 150. Valente, D. *et al.* Pharmacokinetics of novel Fc-engineered monoclonal and multispecific antibodies in cynomolgus monkeys and humanized FcRn transgenic mouse models. *MAbs* **12**, e1829337 (2020).
 151. Haraya, K., Tachibana, T., Nanami, M. & Ishigai, M. Application of human FcRn transgenic mice as a pharmacokinetic screening tool of monoclonal antibody. *Xenobiotica* **44**, 1127–1134 (2014).
 152. Roopenian, D. C., Christianson, G. J. & Sproule, T. J. Human FcRn Transgenic Mice for Pharmacokinetic Evaluation of Therapeutic Antibodies. in *Mouse Models for Drug Discovery. Methods in Molecular Biology (Methods and Protocols)*, vol 602 (eds. Proetzel, G. & Wiles, M. V) 93–104 (Humana Press, 2010). doi:10.1007/978-1-60761-058-8_6.
 153. Wang, W. *et al.* Impact of methionine oxidation in human IgG1 Fc on serum half-life of monoclonal antibodies. *Mol. Immunol.* **48**, 860–866 (2011).
 154. Christianson, G. J., Lowell, E. & Lutz, C. Utility of human FcRn transgenic mice for preclinical screening of immunotherapeutics. *Cancer Res.* **78**, Abstract no 4905 (2018).
 155. Betts, A. *et al.* Linear pharmacokinetic parameters for monoclonal antibodies are similar within a species and across different pharmacological targets: A comparison between human, cynomolgus monkey and hFcRn Tg32 transgenic mouse using a population-modeling approach. *MAbs* **10**, 751–764 (2018).
 156. Kaur, S., Xu, K., Saad, O. M., Dere, R. C. & Carrasco-Triguero, M. Bioanalytical assay strategies for the

-
- development of antibody-drug conjugate biotherapeutics. *Bioanalysis* **5**, 201–226 (2013).
157. Xu, K. *et al.* Characterization of intact antibody-drug conjugates from plasma/serum in vivo by affinity capture capillary liquid chromatography-mass spectrometry. *Anal. Biochem.* **412**, 56–66 (2011).
158. Excoffier, M. *et al.* A new anti-human Fc method to capture and analyze ADCs for characterization of drug distribution and the drug-to-antibody ratio in serum from pre-clinical species. *J. Chromatogr. B* **1032**, 149–154 (2016).
159. Su, D. *et al.* Custom-Designed Affinity Capture LC-MS F(ab')₂ Assay for Biotransformation Assessment of Site-Specific Antibody Drug Conjugates. *Anal. Chem.* **88**, 11340–11346 (2016).
160. Debaene, F. *et al.* Innovative native MS methodologies for antibody drug conjugate characterization: High resolution native MS and IM-MS for average DAR and DAR distribution assessment. *Anal. Chem.* **86**, 10674–10683 (2014).
161. Hengel, S. M. *et al.* Measurement of in vivo drug load distribution of cysteine-linked antibody-drug conjugates using microscale liquid chromatography mass spectrometry. *Anal. Chem.* **86**, 3420–3425 (2014).
162. Kumar, S., King, L. E., Clark, T. H. & Gorovits, B. Antibody–drug conjugates nonclinical support: from early to late nonclinical bioanalysis using ligand-binding assays. *Bioanalysis* **7**, 1605–1617 (2015).
163. Stephan, J. P., Kozak, K. R. & Wong, W. L. T. Challenges in developing bioanalytical assays for characterization of antibody-drug conjugates. *Bioanalysis* **3**, 677–700 (2011).
164. Wang, J. *et al.* Antibody-drug conjugate bioanalysis using LB-LC-MS/MS hybrid assays: strategies, methodology and correlation to ligand-binding assays. *Bioanalysis* **8**, 1383–1401 (2016).
165. Brody, T. *Clinical Trials: Study Design, Endpoints and Biomarkers, Drug Safety, and FDA and ICH Guidelines.* (Elsevier Inc., 2016).
166. Briakinumab amino acid sequence on KEGG database (entry D09588). <https://www.genome.jp/entry/D09588> (2022).
167. Secukinumab amino acid sequence on KEGG database (entry D09967). <https://www.genome.jp/entry/D09967> (2022).
168. Dickgiesser, S., Kellner, R., Kolmar, H. & Rasche, N. Site-Specific Conjugation of Thiol-Reactive Cytotoxic Agents to Nonnative Cysteines of Engineered Monoclonal Antibodies. in *Bioconjugation. (Methods in Molecular Biology)*, vol 2033 (eds. Massa, S. & Devoogdt, N.) 1–14 (Humana, New York, NY, 2019). doi:10.1007/978-1-4939-9654-4_1.
169. Tobias, R. & Ma, W. *Application Note 19: Analysis of FcRn-Antibody Interactions on the Octet platform (Pall ForteBio LLC).* <https://www.sartorius.com/download/552136/analysis-of-fcrn-antibody-interactions-on-the-octet-platform-application-note-en-sartorius-data.pdf> (2017).

-
170. Hawe, A., Sutter, M. & Jiskoot, W. Extrinsic fluorescent dyes as tools for protein characterization. *Pharm. Res.* **25**, 1487–1499 (2008).
 171. Tumey, L. N. *et al.* Site selection: a case study in the identification of optimal cysteine engineered antibody drug conjugates. *AAPS J.* **19**, 1123–1135 (2017).
 172. Chumsae, C., Gaza-Bulseco, G. & Liu, H. Identification and localization of unpaired cysteine residues in monoclonal antibodies by fluorescence labeling and mass spectrometry. *Anal. Chem.* **81**, 6449–6457 (2009).
 173. Wakankar, A., Chen, Y., Gokarn, Y. & Jacobson, F. S. Analytical methods for physicochemical characterization of antibody drug conjugates. *MAbs* **3**, 161–172 (2011).
 174. Guo, J., Kumar, S., Prashad, A., Starkey, J. & Singh, S. K. Assessment of Physical Stability of an Antibody Drug Conjugate by Higher Order Structure Analysis: Impact of Thiol- Maleimide Chemistry. *Pharm. Res.* **31**, 1710–1723 (2014).
 175. Beckley, N. S., Lazzareschi, K. P., Chih, H.-W., Sharma, V. K. & Flores, H. L. Investigation into Temperature-Induced Aggregation of an Antibody Drug Conjugate. *Bioconjug. Chem.* **24**, 1674–1683 (2013).
 176. Grünewald, J. *et al.* Efficient preparation of site-specific antibody–drug conjugates using phosphopantetheinyl transferases. *Bioconjug. Chem.* **26**, 2554–2562 (2015).
 177. Wen, J., Lord, H., Knutson, N. & Wikström, M. Nano differential scanning fluorimetry for comparability studies of therapeutic proteins. *Anal. Biochem.* **593**, 113581 (2020).
 178. Joshi, S., Maharana, C. & Rathore, A. S. An application of nano differential scanning fluorimetry for higher order structure assessment between mAb originator and biosimilars: trastuzumab and rituximab as case studies. *J. Pharm. Biomed. Anal.* **186**, 113270 (2020).
 179. Thies, M. J. W. Struktur , Stabilität und Faltung von Antikörperdomänen (PhD Thesis). (TU München, 2002).
 180. Hinrichs, M. J. M. & Dixit, R. Antibody Drug Conjugates : Nonclinical Safety Considerations. **17**, 1055–1064 (2015).
 181. Ross, P. L. & Wolfe, J. L. Physical and Chemical Stability of Antibody Drug Conjugates: Current Status. *J. Pharm. Sci.* **105**, 391–397 (2016).
 182. An, G. Concept of Pharmacologic Target-Mediated Drug Disposition in Large-Molecule and Small-Molecule Compounds. *J. Clin. Pharmacol.* **60**, 149–163 (2020).
 183. Lima, X. T., Abuabara, K., Kimball, A. B. & Lima, H. C. Briakinumab. *Expert Opin. Biol. Ther.* **9**, 1107–1113 (2009).
 184. Therapeutic Goods Administration (Australian Government). Australian Public Assessment Report for

- Secukinumab. <https://www.tga.gov.au/sites/default/files/auspar-secukinumab-150916.pdf>. (2015).
185. European Medicines Agency. *Herceptin: EPAR - Scientific Discussion*. https://www.ema.europa.eu/en/documents/scientific-discussion/herceptin-epar-scientific-discussion_en.pdf (2005).
186. Joaquin, I. *et al.* Methods For Treating Psoriasis Using Antibodies That Bind To The P40 Subunit Of IL-12 And/Or IL-23. *US 8,557.239 B2* vol. 2 (2013).
187. Bruno, R. *et al.* Population pharmacokinetics of trastuzumab in patients With HER2+ metastatic breast cancer. *Cancer Chemother. Pharmacol.* **56**, 361–369 (2005).
188. Gandhi, M., Alwawi, E. & Gordon, K. B. Anti-p40 antibodies ustekinumab and briakinumab: blockade of interleukin-12 and interleukin-23 in the treatment of psoriasis. *Semin. Cutan. Med. Surg.* **29**, 48–52 (2010).
189. Kelly, R. L. *et al.* Target-independent variable region mediated effects on antibody clearance can be FcRn independent. *MAbs* **8**, 1269–1275 (2016).
190. Dyson, M. R. *et al.* Beyond affinity: selection of antibody variants with optimal biophysical properties and reduced immunogenicity from mammalian display libraries. *MAbs* **12**, e1829335 (2020).
191. Bailly, M. *et al.* Predicting Antibody Developability Profiles Through Early Stage Discovery Screening. *MAbs* **12**, e1743053 (2020).
192. Jones, H. M. *et al.* A Physiologically-Based Pharmacokinetic Model for the Prediction of Monoclonal Antibody Pharmacokinetics From In Vitro Data. *CPT Pharmacometrics Syst. Pharmacol.* **8**, 738–747 (2019).
193. Sun, T. *et al.* High throughput detection of antibody self-interaction by bio-layer interferometry. *MAbs* **5**, 838–841 (2013).
194. Sahoo, H. & Schwille, P. Influence of glycosaminoglycans on lipid dynamics in supported phospholipid bilayers. *Soft Matter* **9**, 3859–3865 (2013).
195. Zhao, H. *et al.* Modulation of macropinocytosis-mediated internalization decreases ocular toxicity of antibody-drug conjugates. *Cancer Res.* **78**, 2115–2126 (2018).
196. Benjamin, S. R. *et al.* Thiolation of Q295 : Site-Specific Conjugation of Hydrophobic Payloads without the Need for Genetic Engineering. *Mol. Pharm.* **16**, 2795–2807 (2019).
197. Ekholm, F. S. *et al.* Hydrophilic Monomethyl Auristatin E Derivatives as Novel Candidates for the Design of Antibody-Drug Conjugates. *Separations* **6**, 1 (2019).
198. Lipinski, C. A., Lombardo, F., Dominy, B. W. & Feeney, P. J. Experimental and computational approaches to estimate solubility and permeability in drug discovery and development settings. *Adv. Drug Deliv. Rev.* **23**, 3–25 (1997).

10. Appendix

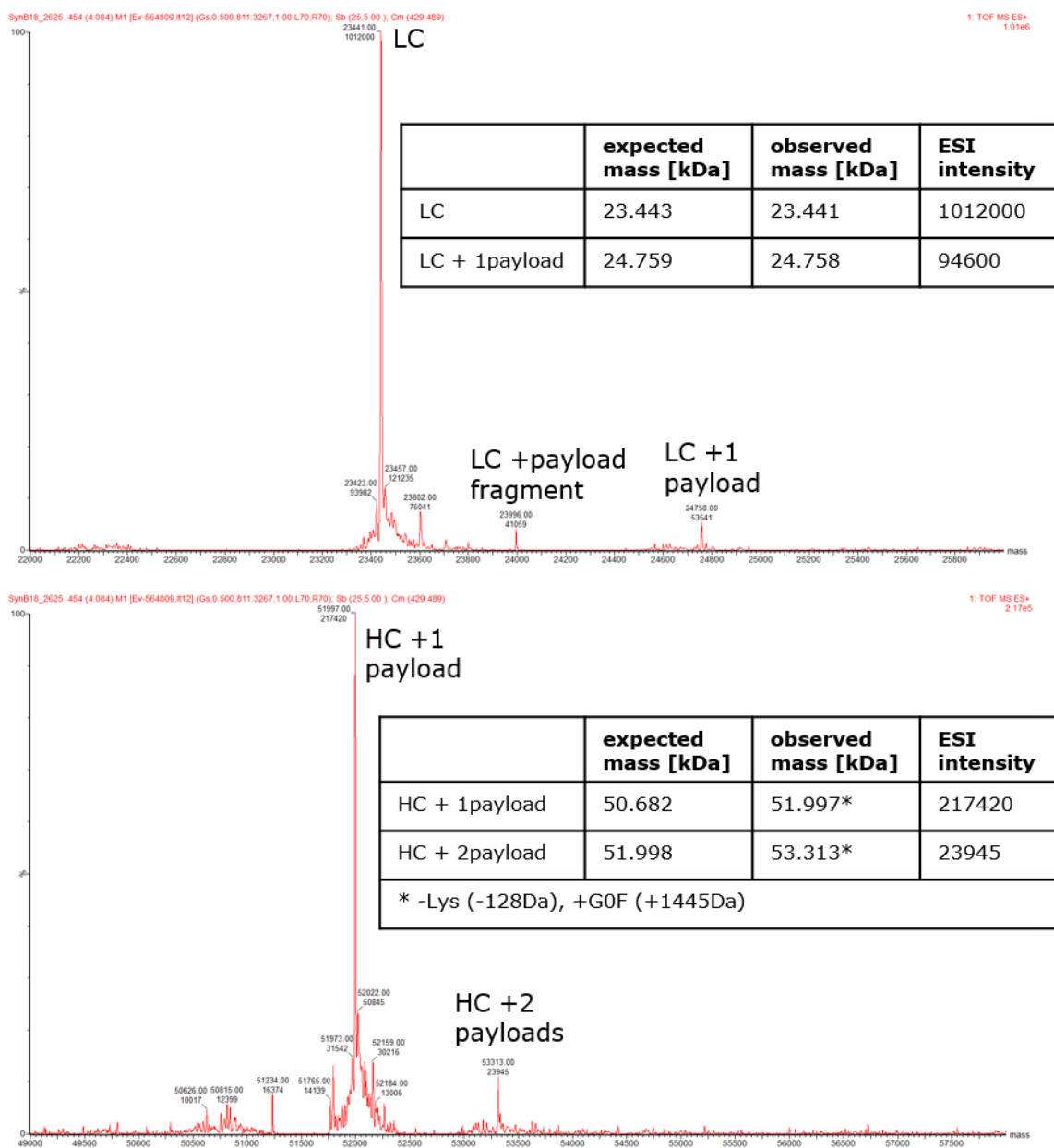


Figure A.1 Example mass analysis results measured by ESI-MS to determine the DAR of T-S293-MMAE. Mass analysis showed that in addition to the expected conjugation of one MC-VC-PAB-MMAE at each HC (position S239) a species with two conjugations of linker-payloads in the HC (9.9%) and a species with one conjugation in the LC (8.5%) was produced, resulting in a total DAR of 2.37.

Briakinumab LC	1	QSVLTQ-PPSVSGAPGQ	RVTISCSGSRSNIGSNT-VK	WYQQLPGTAPKLL	48
Trastuzumab LC	1	DIQMTQSPSSLSASVGDR	VTITCRASQD---VNTAVAWY	QQKPGKAPKLL	47
Briakinumab LC	49	IYYNDQ	RPSGVPDRFSGSKSGTSASLAITGLQAEDEADY	YCQSYDRYTHP	98
Trastuzumab LC	48	IYSASFLYSGVPSR	FSGSRSGTDFTLTIS	LQPEDFATYYCQQH--YTFP	95
Briakinumab LC	99	ALLFGTGTKVTVL	GQPKAAPSVTLFPPSSEELQ	ANKATLVCLISDFYPGA	148
Trastuzumab LC	96	P-TFGQGTKVEI-KR	TVAAPSVFI	FPPSDEQLKSGTASVVCLLN	FYPRE 143
Briakinumab LC	149	VTVAWKADSSPVKAG--	VETTTPSKQ	SNNKYAASSYLSLTPEQ	WKSHKSY 196
Trastuzumab LC	144	AKVQWKVDNA-LQSGNSQESVTEQDS	KDSTYLSSTLTLSKADY	EKKHVV	192
Briakinumab LC	197	SCQVTHEG--	STVEKTVAPTECS		217
Trastuzumab LC	193	ACEVTHQGLSSPVTKS	FNRGEC-		214

Figure A.2 Comparison of the LC amino acid sequence of briakinumab and trastuzumab. Comparison indicated eight glutamine residues in the briakinumab sequence not found in the trastuzumab sequence (red boxes). One or more of these glutamine residues could potentially be accessible for mTG, allowing for conjugation in the LC. Sequence comparison was done by using the EMBOSS Needle tool from EMBL-EBI.

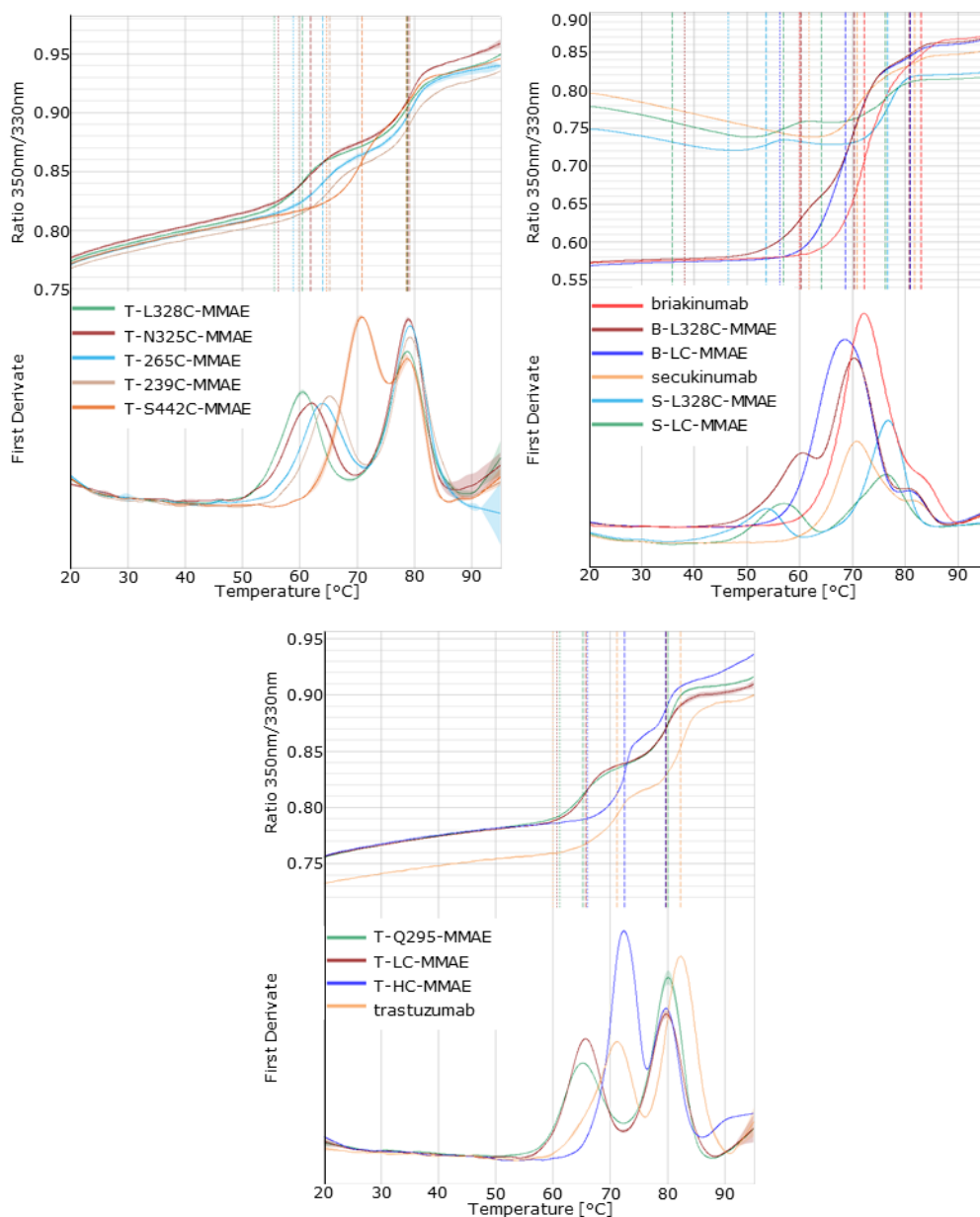


Figure A.3 Thermal stability raw data measured by nanoDSF of trastuzumab-, briakinumab-, and secukinumab-ADCs, and of the corresponding native mAbs. Unfolding curves (upper area in each picture) and corresponding first derivate (lower area in each picture) indicating the denaturation midpoints T_{m1} (C_H2 domain, first peak at lower temperature) and T_{m2} (Fab/ C_H3 domain, second peak at higher temperature).

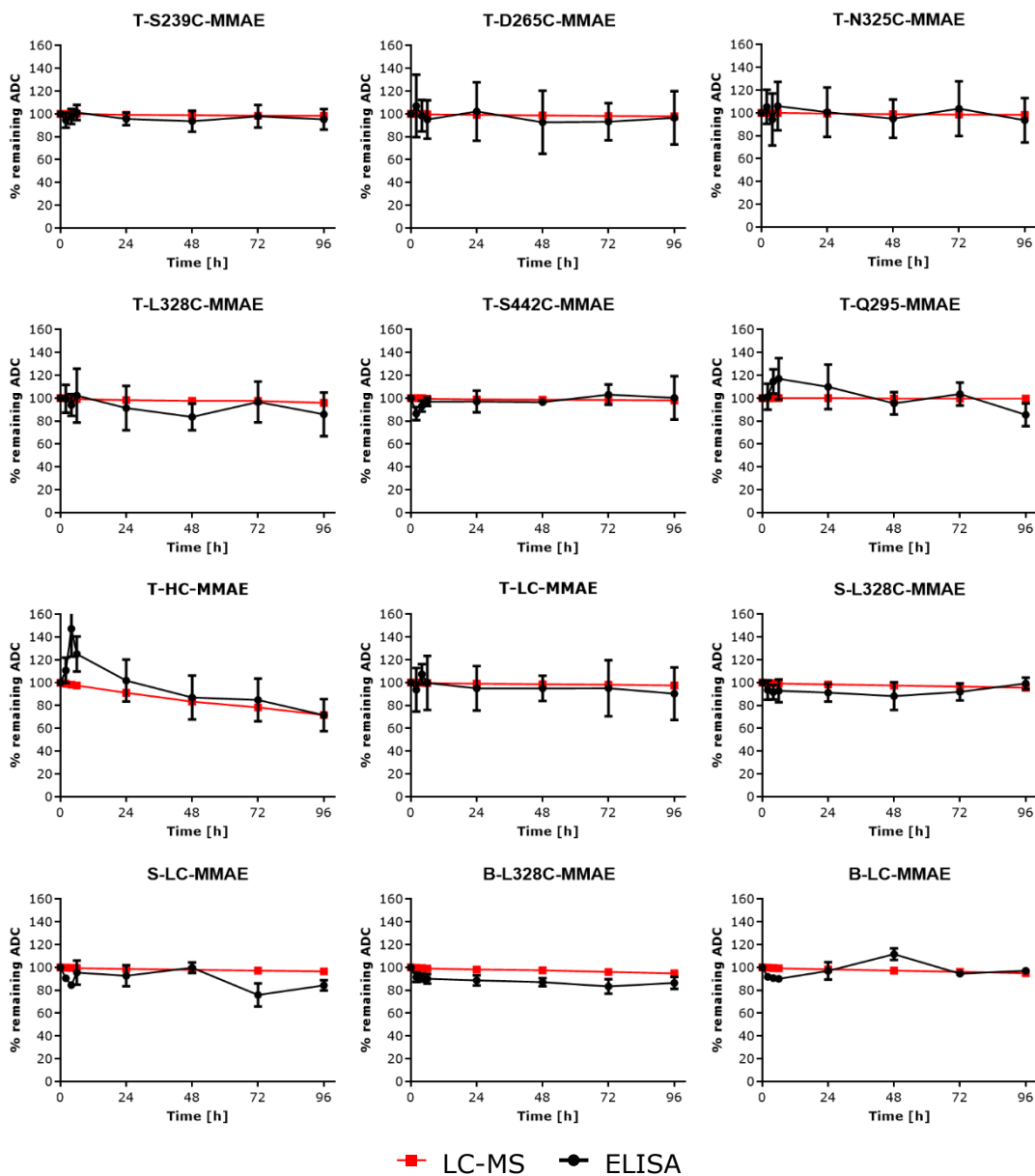


Figure A.4 Mouse serum stability measurement results. ADCs were incubated up to 96 h in mouse serum. Samples were taken in duplicates after 0, 2, 4, 6, 24, 48, 72, and 96 h of incubation and fraction of intact ADC was measured by antibody-conjugated payload ELISA (black bars) and free MMAE by LC-MS, of which the concentration of conjugated-payload (in % ADC remaining) was calculated (red bars). Error bars represent SD.

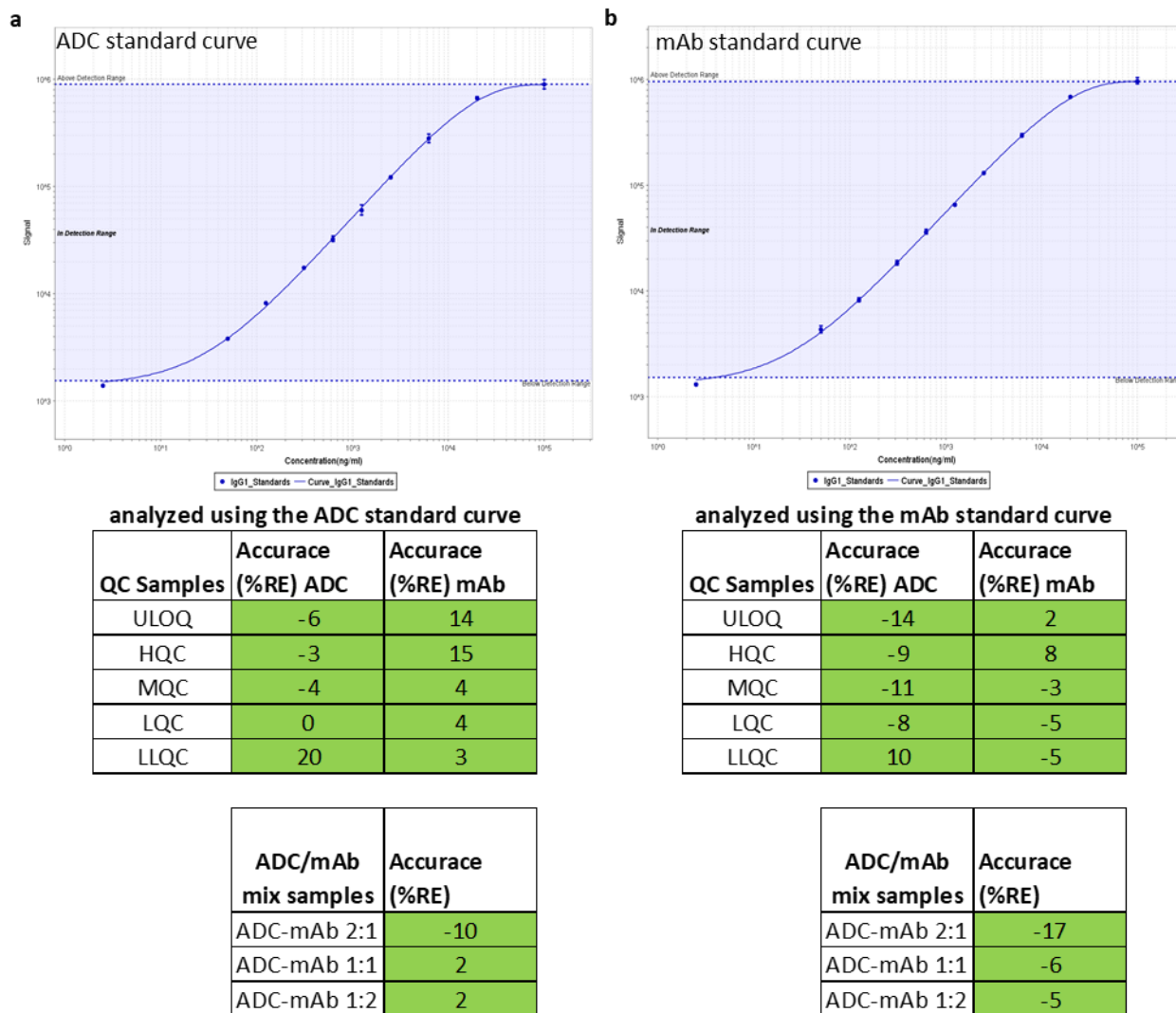


Figure A.5 DAR-sensitive test of the reagents for the electroluminescence LBA. Test exemplarily shown for T-D265C-MMAE using the capture reagent biotin-SP-conjugated AffiniPure goat anti-human IgG (Fcγ fragment specific, JIR #109-065-098) and the detection reagent mouse anti-human IgG (F(ab')₂ fragment specific, JIR, # 209-005-097) labeled with SULFO-TAG. A calibration standard, each of the ADC and corresponding unconjugated mAb (0–100000 ng/mL), different quality controls (QC) of mAb and ADC (ULOQ 20000 ng/mL, HQC 5000 ng/mL, MQC 1000 ng/mL, LQC 150 ng/mL, and LLOQ 50 ng/ml), and three different mixtures of mAb and ADC (total 1000 ng/mL) spiked into mouse plasma were prepared and analyzed. Shown are the accuracies of the analyzed QCs and ADC/mAb mixture concentrations using the standard curves prepared with the ADC (a) or with the mAb (b). As the % of accuracy is within ±20% for all the samples, especially for ADC QCs that were analyzed with the mAb standard curve and vice versa, it indicates absence of a DAR-sensitivity of the used detection reagent combination.

10.1. Abbreviations

ACN	Acetonitrile
AC-SINS	Affinity-capture self-interaction nanoparticle spectroscopy
ADC	Antibody-drug conjugates
AHC	Anti-human IgG Fc capture biosensor
ALCL	Anaplastic large-cell lymphoma
ALL	Acute lymphoblastic leukemia
AML	Acute myeloid leukemia
ANS	Anilinonaphthalene sulfonate
AUC	Area-under-the-curve
A _x	Absorbance at x nm
B2M	β2-macroglobulin
BCA	Bicinchoninic acid
BCMA	B-cell maturation antigen
bis-ANS	4,4'-Dianilino-1,1'-binaphthyl-5,5'-disulfonic acid dipotassium salt
B-L328C-MMAE	Briakinumab ADC with VC-PAB-MMAE conjugated <i>via</i> site-specific cysteine conjugation to the engineered cysteine position L328C
B-LC-MMAE	Briakinumab ADC with VC-PAB-MMAE conjugated <i>via</i> mTG to a recognition motif engineered C-terminally at mAb LCs
BLI	Bio-Layer Interferometry
BQL	Below quantification limit
BSA	Bovine serum albumin
BsAbs	Bispecific antibodies
BVP	baculovirus particles
C	Cleavable linker
C1q	Complement Component C1q
CAG	Chicken beta-actin/rabbit beta-globin hybrid promoter
CatB	Cathepsin B
CD	Cluster of differentiation
CDR	Complementary-determining regions
Ces1C	Carboxylesterase 1C
C _H 1, 2, 3	Constant domain 1, 2, 3 of the heavy chain

CHO	Chinese hamster ovary
C _L	Constant domain of the light chain
CL	Clearance
CL2A	Cleavable PEG8- and triazole-containing PABC–peptide–MC linker
C _{max}	maximum observed plasma concentration
CMV	Cytomegalovirus immediate early promoter
CSI-BLI	Clone self-interaction Bio-Layer interferometry
CV	Column volume
Cys	Interchain cysteine conjugation
DAR	Drug-to-antibody ratio
DDM	N-Dodecyl-β-maltoside
DLBCL	Diffuse large B cell lymphoma
DM1	Derivate of maytansine
DMSO	Dimethyl sulfoxide
DNA	Deoxyribonucleic acid
DPBS	Dulbecco's Phosphate Buffered Saline
DXd	Exatecan derivate
ECM	Engineered cysteine mAb
EDTA	Ethylenediaminetetraacetic acid
EGFR	Epidermal growth factor receptor
ELISA	Enzyme-linked immunosorbent assay
ErbB2	Erythroblastic leukemia viral oncogene homolog 2
ESI-MS	Electrospray ionization mass spectroscopy
Fab	Fragment of antibody binding
FAB2G biosensor	Fab-CH1 2 nd Generation biosensor
Fc	Fragment crystalline
FcRn	Neonatal Fc receptor
FcγR	Fc-gamma-receptor
FDA	Food and Drug Administration (United States of America)
G ₃	glycine- glycine- glycine
GFS	Gel filtration standard
GGPG	glycine-glycine-phenylalanine-glycine
HC	Heavy chain

HEK	Human embryonic kidney
HEPES	4-(2-hydroxyethyl)-1-piperazineethanesulfonic acid
HER2	human epidermal growth factor receptor 2
HIC	Hydrophobic interaction chromatography
HL	Hodgkin lymphoma
HNSTD	Highest non-severely toxic dose
HPLC	High-performance liquid chromatography
HQC	High quality control
HSA	Human serum albumin
Hsp70, 90	Heat shock protein 70, 90
huFcRn	Human neonatal Fc receptor
Ig	Immunoglobulin
IL	Interleukin
IVIVC	<i>In vitro in vivo</i> correlations
k_a	Association rate
K_D	Equilibrium dissociation constant
k_d	Dissociation rate
kDa	Kilo Dalton
LB medium	Luria-Bertani medium
LBA	Ligand binding assays
LC	Light chain
LC-MS	Liquid chromatography-mass spectrometry
LC-MS/MS	Liquid chromatography with tandem mass spectrometry
L-DHA	L-Dehydroascorbic acid
LLOQ	Lower limit of quantification
LQC	Low quality control
Lys	Random lysine conjugation
mAb	Monoclonal antibody
MC	Maleimidocaproyl
MCC	4-maleimidomethyl cyclohexane-1-carboxylate
MDR1	Multidrug resistance protein 1
MED	Minimum effective dose
MES	2-Morpholinoethanesulfonic acid monohydrate

MHC	Major histocompatibility complex
MMAE	Monomethyl auristatin E
MMAF	Monomethyl auristatin F
MoA	Mechanism of action
MOE	Molecular Operation Environment
MQC	Middle quality control
MS	Mass spectrometry
MSA	Murine serum albumin
MSD	Meso Scale Diagnostics
MTD	Maximum tolerated dose
mTG	Microbial transglutaminase
MUC1	Mucin-1
MW	Molecular weight
MWCO	Molecular weight cut-off
nanoDSF	Nano Differential Scanning Fluorimetry
Na _v 1.7	Voltage-gated sodium channel NaV1.7
NC	Non-cleavable linker
NEM	N-ethyl maleimide
NHP	Nonhuman primate
nRT	Normalized retention time
OD450	Optical density at 450 nm
PAB	Para-aminobenzyl alcohol
PBD	Pyrrolobenzodiazepine
PBS	Phosphate buffered saline
PCR	Polymerase chain reaction
PDB	Protein Data Bank
PEG	Polyethyleneglycol
PK	Pharmacokinetics
PSR	Polyspecificity reagent
PSR-BLI	Polyspecificity reagent Bio-Layer Interferometry
PVDF	Polyvinylidene fluoride
PW	Peak width at half peak height
QC	Quality control

RFI	Relative fluorescence intensity
RNA	Ribonucleic acid
ROR1	Tyrosine-protein kinase transmembrane receptor
rpm	Revolutions per minute
rPW	Relative peak width
rRT	Relative retention time
RT	Retention time
<i>S. aureus</i>	<i>Staphylococcus aureus</i>
<i>S. mobaraensis</i>	<i>Streptomyces mobaraensis</i>
S.O.C medium	Super optimal broth medium
SD	Standard deviation
SEC	Size exclusion chromatography
SE-HPLC	Analytical size exclusion-high-performance liquid chromatography
SEM	Standard error of the mean
S-L328C-MMAE	Secukinumab ADC with VC-PAB-MMAE conjugated <i>via</i> site-specific cysteine conjugation to the engineered cysteine position L328
S-LC-MMAE	Secukinumab ADC with VC-PAB-MMAE conjugated <i>via</i> mTG to a recognition motif engineered C-terminally at mAb LCs
SMCC	Succinimidyl 4-(<i>N</i> -maleimidomethyl)cyclohexane-1-carboxylate
SN38	Active metabolite of the topoisomerase I inhibitor irinotecan
SPR	Surface plasmon resonance
SrtA	Sortase A
$t_{1/2}$	Half-life
TAA	Tumor-associated antigen
TCEP	Tris(2-carboxyethyl)phosphine
T-D265C-MMAE	Trastuzumab ADC with VC-PAB-MMAE conjugated <i>via</i> site-specific cysteine conjugation to the engineered cysteine position D265
T-DM1	Ado-trastuzumab emtansine
TF	Tissue factor
Tg	Transgenic
T-HC-MMAE	Trastuzumab ADC with VC-PAB-MMAE conjugated <i>via</i> mTG to a recognition motif engineered C-terminally at mAb HCs

T-L328C-MMAE	Trastuzumab ADC with VC-PAB-MMAE conjugated <i>via</i> site-specific cysteine conjugation to the engineered cysteine position L328
T-LC-MMAE	Trastuzumab ADC with VC-PAB-MMAE conjugated <i>via</i> mTG to a recognition motif engineered C-terminally at mAb LCs
T _m 1, 2	Transition midpoints 1, 2
TMB	3,3',5,5' tetramethylbenzidine
TMDD	Target mediated drug disposition
T-N325C-MMAE	Trastuzumab ADC with VC-PAB-MMAE conjugated <i>via</i> site-specific cysteine conjugation to the engineered cysteine position N325
TNBC	Triple negative breast cancer
T-Q295-MMAE	Trastuzumab ADC with VC-PAB-MMAE conjugated <i>via</i> mTG to position Q295 of the native mAb
TROP-2	Tumor-associated calcium signal transducer 2
T-S239C-MMAE	Trastuzumab ADC with VC-PAB-MMAE conjugated <i>via</i> site-specific cysteine conjugation to the engineered cysteine position S239
T-S442C-MMAE	Trastuzumab ADC with VC-PAB-MMAE conjugated <i>via</i> site-specific cysteine conjugation to the engineered cysteine position S442
TY medium	Medium consisting of tryptone and yeast extract
ULOQ	Upper limit of quantitation
UPLC	Ultra-performance liquid chromatography
UV/VIS	Ultraviolet and visible spectroscopy
V	Volume of distribution
v/v	Volume per volume
VA	Valine-alanine
VC	Valine-citrulline
V _H	Variable domain of the heavy chain
V _L	Variable domain of the light chain
V _{ss}	Volume of distribution at steady state
w/v	Weight per volume
κ	Kappa
λ	Lambda
λ _{max}	Wavelength of maximum absorbance
ρ	Spearman correlation coefficient

10.2. List of Figures

Figure 1. Comparison of the therapeutic windows of a conventional chemotherapy and ADC therapy.	6
Figure 2. ADC mode of action.	7
Figure 3. Schematic representation of an ADC. The ADC consists of an antibody equipped with cytotoxic payload that is attached via a linker.	8
Figure 4. Chemical structure of the cleavable dipeptide linker VC-PAB-MMAE.	13
Figure 5. Heterogeneity in the ADC conjugation sites and drug-to-antibody ratio (DAR) of ADCs generated with different conjugation techniques.	14
Figure 6. Cysteine conjugated ADCs with maleimide-based linkers.	15
Figure 7. ADCs generation via microbial transglutaminase (mTG).	16
Figure 8. Illustration of the dependency between the PK and safety of ADCs.	18
Figure 9. Schematic illustration of the FcRn mediated recycling of Fc-fragment containing molecules.	20
Figure 10. Exemplary pharmacokinetic profiles of ADC analytes.	26
Figure 11. Usage of a standard, containing ADCs with different DARs, to calculate normalized retention times (nRTs) of sample ADCs.	48
Figure 12. Conjugation sites and linker-payloads for site specific conjugation via mTG and via engineered cysteines used for systematic characterization.	60
Figure 13. Hydrophobicity of the ADCs measured by HIC.	63
Figure 14. Thermal stability of ADCs and corresponding native antibodies measured by nanoDSF.	65
Figure 15. Representative BLI sensorgrams of the association and dissociation profiles of immobilized T-LC-MMAE and soluble recombinant huFcRn (1.6-0.05 μ M).	67
Figure 16. Mouse serum stability measurements via orthogonal conjugated-payload ELISA or free payload LC-MS/MS.	68
Figure 17. Comparative analysis of structural models of the T-HC-MMAE and T-S442C-MMAE.	70
Figure 18. Pharmacokinetic profiles of the ADCs and native mAbs in huFcRn mice.	72
Figure 19. Comparison of the total antibody CL in huFcRn transgenic mice of ADCs conjugated at position L328C (blue) or C-terminally at the LCs (red) and corresponding native mAbs (gray).	75
Figure 20. Relationship between the PK in huFcRn Tg276 mice and results in different <i>in vitro</i> assays.	77
Figure 21. Total antibody clearance values of the different study ADCs (ADC1-ADC13) in huFcRn transgenic mice (hemizygous Tg276).	79
Figure 22. Analysis of the self-interaction tendencies of ADCs by AC-SINS.	82
Figure 23. Results of the CSI-BLI assay.	84



Figure 24. Results of the BVP and heparin ELISA measurement to analyze non-specific binding of the ADCs.86

Figure 25. Results of the PSR-BLI assay.88

Figure 26. Hydrophobicity of ADCs analyzed by bis-ANS assay.91

Figure 27. huFcRn affinity chromatography results of ADCs and control mAbs.93

Figure 28. Correlation of *in vitro* assay results.96

Figure 29. Relationship between the clearance in huFcRn transgenic mice (hemizygous Tg276) and the results in different *in vitro* assays of the 13 study ADCs.99

Figure A.1 Example mass analysis results measured by ESI-MS to determine the DAR of T-S293-MMAE....115

Figure A.2 Comparison of the LC amino acid sequence of briakinumab and trastuzumab.116

Figure A.3 Thermal stability raw data measured by nanoDSF of trastuzumab-, briakinumab-, and secukinumab-ADCs, and of the corresponding native mAbs.117

Figure A.4 Mouse serum stability measurement results.118

Figure A.5 DAR-sensitive test of the reagents for the electroluminescence LBA.119

10.3. List of Tables

Table 1. FDA approved ADCs.	10
Table 2. Linear pH gradient used for the huFcRn affinity chromatography.	53
Table 3. pH gradient used to wash and re-equilibrate the huFcRn column after every fifth mAb/ADC sample analysis.	53
Table 4. Purity and DAR of the cysteine and mTG-conjugated ADCs.	61
Table 5. FcRn binding kinetics of ADCs and native mAbs.	66
Table 6. Total antibody and antibody-conjugated MMAE pharmacokinetics in huFcRn mice.	74
Table 7. Overview of the ADC design features and product characteristics of the 13 study ADCs.	80

10.4. Acknowledgements

Mein erster Dank gilt Prof. Dr. Harald Kolmar für die akademische Betreuung meiner Dissertation an der TU Darmstadt, dem Interesse an meiner Forschungstätigkeit und der Unterstützung durch konstruktive Ratschläge und Taten. Darüber hinaus möchte ich ihm für die Möglichkeit des interessanten wissenschaftlichen Austauschs sowohl mit der Arbeitsgruppe in Form von Seminaren und Ausflügen in das Kleinwalsertal als auch durch die Teilnahme an der PEGS Lissabon danken.

Prof. Dr. Dr. Siegfried Neumann möchte ich für die Übernahme des Koreferats danken. Weiterhin möchte ich Dr. Tobias Meckel und Prof. Dr. Dominik Niopek dafür danken, dass sie sich als Fachprüfer meiner Disputation zur Verfügung stellen, und Herrn Prof. Dr. Schmidt für die Übernahme des Vorsitzes.

Ein besonderer Dank gilt Dr. Christian Schröter für die Unterstützung, wissenschaftliche Betreuung, wertvollen Diskussionen, fachlichen und persönlichen Ratschläge sowie auch für seine optimistische Einstellung, die für mich eine zusätzliche Motivationsquelle darstellte. Auch dem gesamten Team Schröter, Anja Lamack, Dr. Doreen Könning, Gernot Musch und Vanessa Lautenbach gilt mein besonderer Dank für die großartige Zusammenarbeit und Unterstützung und für die vielen gemeinsamen Mittagessen. Bei Anja und Vanessa möchte ich besonders für die tolle Atmosphäre im Labor bedanken. Es hat sehr viel Spaß gemacht und ich vermisse es schon jetzt.

Ebenso möchte ich mich herzlich bei Dr. Stefan Hecht und Dr. Jan Anderl bedanken, die mir die Möglichkeit gegeben haben, in diesem spannenden Themenfeld zu promovieren und zahlreiche sowohl persönliche als auch wissenschaftliche Erkenntnisse und Erfahrungen zu sammeln. Im speziellen möchte ich mich für die Möglichkeit der Teilnahme an dem intensiven PK Seminar in Arosa bedanken. Auch für die Möglichkeit einen Teil der Analysen der PK Studien selbst durchzuführen und dazu gemeinsam mit den DMPK Kollegen in Ivrea zu arbeiten, möchte ich mich bedanken. Besonders auch dafür, dass diese Studien überhaupt möglich waren. Diesbezüglich gilt mein besonderer Dank auch Dr. Simona Riva, Dr. Kyra Cowan und allen weiteren Personen, die dies ermöglicht haben, hier aber namentlich nicht genannt sind. Dr. Hecht möchte ich zusätzlich für die Unterstützung durch zahlreiche konstruktive Anmerkungen und Anregungen danken.

Desweiteren möchte ich mich bei Dr. Nicolas Rasche und seinem gesamten Team für die Konjugationen, SEC und HIC Analysen der ADCs bedanken. Mein besonderer Dank gilt hierbei Ingrid Schmidt, Jens Hannewald, Laura Basset, Markus Fleischer und Vanessa Grünewald. Jens Hannewald möchte ich zudem für die Hilfestellungen, im Besonderen bezüglich der HPLC Anwendung, danken. Zudem danke ich Dr. Stephan

Dickgiesser für seine fachliche Unterstützung und Zusammenarbeit bei der Untersuchung der unterschiedlichen Konjugationspositionen, im Besonderen für die Auswahl der Konjugationspositionen sowie für die Möglichkeit diese mittels verschiedener Versuche vergleichen zu können.

Überdies danke ich Roland Kellner und seinem gesamten Team für die Bereitstellung der DAR Daten, der nanoDSF Daten und der Hilfestellung bei fachlichen Fragen. Hier gilt mein besonderer Dank Amanda Friedrich und Jennifer Schanz für die Durchführung der Analysen.

Auch Dirk Müller-Pompalla und seinem Team gilt mein Dank für die Bereitstellung von Materialien, wie des rekombinanten huFcRn Materials, die Mitbenutzung von Laborgeräten, wie Ultrazentrifugen, und diverse Hilfestellungen. Im speziellen möchte ich hier Sigrid Auth für einige Antikörper-Aufreinigungen und Stephan Keller für die Herstellung der huFcRn Säulen danken.

Thomas Rysiok und seinem Team, im besonderen Oliver Edler, möchte ich meinen Dank für die fachliche Hilfe in Bezug auf die Antikörperexpression, für die zur Verfügungstellung von Zellen, sowie für die Durchführung einiger der Expression aussprechen.

Next, I must apologize, but unfortunately my Italian has not progressed very much, so I must stick to English. At the Ivrea site, I would like to thank all my colleagues who made my stay in Ivrea a great experience, the incredibly warm welcome (whether with or without a language barrier), the great collaboration, and also the activities in the free time and the participation in the EHS team event. In particular, I would like to thank Dr. Elisa Bertotti for letting me perform the LBA experiment in her lab (and also for the insect repellent provided ;-)). Furthermore, I would like to thank Dr. Federico Riccardi Sirtori and the LC-MS team for working together in the LC-MS lab. Here I would like to thank in particular Dr. Francesco Molinaro, Dr. Ilse Maria Luce De Salve, and Dr. Luca Maria Barbero. I would also like to thank Dr. Francesco Molinaro for the great day and the personal city tour in Torino. Special thanks also go to Dr. Andrea Paoletti for providing the final PK parameter and organizing the PK study. In addition, I would like to thank the whole DMPK team, inside and outside Italy, for providing the results of the further PK studies and for the continued good cooperation and discussions.

Darüber hinaus gilt mein Dank sehr vielen weiteren Menschen bei Merck für die Bereitstellung von Materialien und Geräten, für die Unterstützung und Hilfestellungen auf unterschiedliche Arten und im Besonderen auch für die vielen freundlichen Gespräche, die mir unter anderem sehr dabei geholfen haben neue Ideen zu entwickeln oder auch einfach nur den Arbeitsalltag auflockerten: Dr. Simon Krah, Dr. Stefan Zielonka, Dr. Lars Toleikis, Ralf Günther, Dr. Stefan Becker, Florian Gross, Alexander Müller, Marion Sauer, Dominik Reitz, Svenja Wolber, Steffen Rindfuß, Iris Mannberger, Dr. Andreas Evers, Dr. João Pereira, Dr. Laura Sponton, Dr. Stanley Sweeney-Lasch, Dr. Birgit Piater, Kirsten Leidiger, Tessa-Madeleine Heuer, Ana Cristina

Silva Castro, Selma Bozkurt, Dr. Jan Baumann, Dr. Uwe Wittenberg, Michael Brandt, Uwe Schilke, Dr. Vanessa Siegmund, Elvira Meissen, Konstanze Waurisch, Nils Bahl, Sonja Dreher, Marion Wetter, Dr. Jason Tonillo, Angelika-N. Helfrich, Pia Stroh, Claudia Kubis, Dr. Sakshi Garg, Ramona Gaa, Laura Unmuth, Dr. Carl Deutsch, Dr. Min Shan, Dr. Achim Doerner, Dr. Laura Rhiel, Deniz Demir, Kerstin Hallstein, Dr. Carolin Sellmann, Dr. Alec Gross, Iris Willenbuecher, Elke Ciesielski, Christina Bauer, Daniela Noack, Dr. Jean Wakim, Helene Crassier, Mirela Kunkel, Antje Schoeneberg, Katrin Schreiber, Dr. Bernhard Valldorf, Beatrix Boeckler und Teresa Gorgol.

Und natürlich gilt mein Dank auch den ehemaligen und aktuellen Doktoranden-„Mitstreitern“ bei Merck für die netten Mittagessen, Gespräche und auch den wissenschaftlichen Austausch: Vielen Dank M.Sc. Quillmann, Dr. Tim Hofmann, Dr. Marcel Rieker, Dr. Lukas Pekar, M.Sc. Tanja Lehmann, Dr. Janis Roszkopf, M.Sc. (so gut wie Dr.) Sandra Müller, Dr. Martina Zimmermann, Dr. Markus Lubda, und M.Sc. Janina Klemm. Ein besonderer Dank gilt meinem Sinntaler-Doktoranden-Kollegen, Dr. Sebastian Jäger, für die aufmunternde und sehr hilfreiche Unterstützung während der finalen Phase.

Barbara Diestelmann gilt mein Dank für die organisatorischen Hilfen bezüglich Uni-Angelegenheiten (inklusive den ‚postalischen Übermittlungen‘ während der Corona-Zeit) und dem immer freundlichen und netten Kontakt.

Meinen Eltern möchte ich für die seelische Unterstützung danken sowie für das Verständnis für einen eingeschränkten Kontakt während stressiger Phasen.

Zu guter Letzt möchte ich mich bei Patrick bedanken. Danke, dass du mich auch in den letzten, besonderen Jahren ausgehalten hast und Geduld mit mir hattest. Danke auch für deinen Rückhalt und Zuspruch, ohne den ich diese Arbeit vermutlich nicht angefertigt hätte.

11. Affirmations

Erklärungen laut Promotionsordnung

§8 Abs. 1 lit. c PromO

Ich versichere hiermit, dass die elektronische Version meiner Dissertation mit der schriftlichen Version übereinstimmt und für die Durchführung des Promotionsverfahrens vorliegt.

§8 Abs. 1 lit. d PromO

Ich versichere hiermit, dass zu einem vorherigen Zeitpunkt noch keine Promotion versucht wurde und zu keinem früheren Zeitpunkt an einer in- oder ausländischen Hochschule eingereicht wurde. In diesem Fall sind nähere Angaben über Zeitpunkt, Hochschule, Dissertationsthema und Ergebnis dieses Versuchs mitzuteilen.

§9 Abs. 1 PromO

Ich versichere hiermit, dass die vorliegende Dissertation selbstständig und nur unter Verwendung der angegebenen Quellen verfasst wurde.

§9 Abs. 2 PromO

Die Arbeit hat bisher noch nicht zu Prüfungszwecken gedient.

Ort, Datum: Darmstadt, 01.06.2022

Unterschrift:



Anna Kaempffe